UNIVERSITY of CALIFORNIA

SANTA CRUZ

WHITE DWARFS IN OPEN CLUSTERS: THE INITIAL-FINAL MASS RELATION, THE SUPERNOVA MASS LIMIT, AND THE WHITE DWARF DEFICIT

A dissertation submitted in partial satisfaction of the
requirements for the degree of

DOCTOR OF PHILOSOPHY

in

ASTRONOMY AND ASTROPHYSICS

by

Kurtis A. Williams

December 2002

The Dissertation of Kurtis A. Williams
is approved:

Professor Michael Bolte, Chair

Professor Graeme Smith

Professor William Mathews

Frank Talamantes
Vice Provost and Dean of Graduate Studies

Table of Contents

List of Figures

List of Tables

Abstract

White Dwarfs in Open Clusters: The initial-final mass relation, the supernova mass limit, and the white dwarf deficit

by

Kurtis A. Williams

White dwarfs are useful tools for studying numerous interesting astrophysical phenomena. The upper limit for white dwarf progenitor masses provides a lower limits on the mass of supernova progenitors. The initial-final mass relation gives the integrated mass loss over the lifetime of a star. This dissertation presents the results from a photometric and spectroscopic study of WDs in nearby open clusters. First, a sample of nearby open clusters is constructed. Second, photometry from a subset of the sample clusters, NGC 2168, IC 4665, NGC 6633, and NGC 7063, is presented and white dwarf candidates selected. Spectroscopic follow-up of the white dwarf candidates uncovered four cluster member white dwarfs, a number far below what would be expected based on integration of the initial-mass function in the clusters. Two of the white dwarfs agree with the existing Hyades and Praesepe empirical initial-final mass relationship; a third cluster white dwarf is a suspected helium-core white dwarf. The high-mass end of the initial-final mass relation, previously determined from white dwarfs in NGC 2516 and the Pleiades, is found to be highly sensitive to the adopted ages of these clusters. The lower limit on the upper mass of main sequence parameters is reduced to $5.7 M_{\odot}$ when the age uncertainties are taken into account. Finally, a Monte Carlo simulation is used to show that the apparent lack of white dwarfs in most open cluster can be mostly explained by WDs in binary systems, the first time that this effect has been quantified.

For M & M

Acknowledgements

I owe many thanks to many people for the duration of this project. I would like to acknowledge the tireless efforts of my committee, especially those of Mike Bolte. Many thanks are also due to Matt Wood and Prof. Dr. Detlev Koester, who freely provided the WD and atmospheric models used in this analysis. Thanks also to Phyllis Wattis and the Northern California ARCS Foundation, who provided financial support during a portion of this research. Thanks to Sarah Martell for providing observing support when I insisted on going observing a week after being released from the hospital, to George Blumenthal for helping me understand χ^2 fitting. A load of thanks to a variety of people for their help along the way: L. Binkley, W. Brinkmann, S. Dehoff, K. Flint, A. Gonzalez, A. Goto, J. Harris, A. Metevier, J. C. McGrath, T. Nielsen, G. Penn & K. Müller-Osten, C. Rudokas & G. Guinee, D. Schneider, A. Zabludoff, my family, and all the other grads, faculty, and staff in the Department.

And last, but far, far from least, thanks to my wife, the world's most gracious telescope widow.

Chapter 1

Introduction

Spectrum analysis enabled the astronomer to tell when a star was advancing head on, and when it was going the other way. This was regarded as very precious. Why the astronomer wanted to know, is not stated, nor what he could sell out for, when he did know. An astronomer's notions about preciousness are loose. They are not much regarded by practical men, and seldom excite a broker.

— Mark Twain, "The Secret History of Eddypus"

To first order, white dwarfs are straightforward systems to model: a degenerate core surrounded by a non-degenerate atmosphere cooling passively by radiation of thermal energy. The first WD cooling models based on this picture were developed by Mestel (1952). Developments in stellar evolutionary theory led to the realization that WDs were the remnant cores of evolved stars (Schwarzschild, 1958). Theoretical studies of nucleosynthesis in evolved stars led to the conclusion that WDs must consist of ^{12}C and ^{16}O (see Salpeter 1971 and references therein). These advances led to the development of new evolutionary models for $1M_{\odot}$, pure ^{12}C WDs (Lamb & van Horn, 1975).

Numerous obstacles in WD theory remained to be overcome in order to produce useful cooling models. WDs span a range of masses, from $\sim 0.4M_{\odot}$ up to the Chandrasekhar mass ($\sim 1.4M_{\odot}$), with the majority of WD masses around $0.6M_{\odot}$. In addition, the chemical composition of WDs is a C/O mixture, and the C/O ratio likely varies with radius. Asteroseismological observations of pulsating DA WDs have provided convincing evidence that the DA atmospheres are "thick", i.e. the surface H layers are on the order of $10^{-4}M_{*}$, the maximum atmospheric mass before H-burning would ignite in the atmosphere (Fontaine et al., 1992).

In light of these considerations, Wood (1995, hereafter W95) developed evolutionary models for C/O WDs for a variety of masses. These models include a radially-varying C/O ratio and maximal H and He envelopes of zero metallicity. The C/O profile was chosen to be typical of that obtained from post-AGB evolutionary calculations, but is dependent upon the highly uncertain ^{12}C(α,γ)^{16}O reaction rate (Wood, 1990). Subsequent work on WD evolution has focused on effects such as chemical separation and crystallization (Salaris et al., 1997), atmospheric convection (Fontaine et al., 2001), and cool atmospheric physics (Hansen, 1999), effects which become important for $T_{\rm eff} \lesssim 10^4$K.

1.1 Supernovae and the interstellar medium

Supernovae are among the most energetic events in the present-day universe. It is generally accepted that two types of supernovae occur: those originating from the collapse of a core in a highly-evolved massive star (core-collapse supernovae), and those resulting from the detonation of Chandrasekhar-mass WDs (Type Ia). Supernovae result in the release of significant amounts of processed stellar material and metals into the interstellar medium (ISM), as well as the release of significant quantities of kinetic energy.

Stellar evolutionary and supernova explosion models suggest that core-collapse supernovae occur in stars which carbon burning ignites in the core (Mayle & Wilson, 1988 and references therein). We will refer to the minimum main-sequence mas for which a core-collapse supernova occurs as $M_{\rm crit}$. Although the canonical value for $M_{\rm crit}$ from stellar evolutionary models is $8M_\odot$, it depends on the star's metallicity and the exact detail on input physics (Dominguez et al., 1999). Recent evolutionary models including a modest amount of convective overshoot ignite carbon for main-sequence masses of $6M_\odot$ (Girardi et al., 2000), and $M_{\rm crit}$ could be as low as $5M_\odot$ (Castellani et al., 1985).[1]

Because of their large kinetic energies ($\sim 10^{51}$ ergs), supernovae have an enormous impact on gas in galaxies, and supernova feedback is considered fundamental to understanding star formation rates in galaxies (e.g. Somerville and Primack, 1999), the evolution of starbursts and star formation regions (e.g. Leitherer et al., 1999), and the evolution of gas and the ISM in dwarf galaxies (Dekel & Silk, 1986; Ferrara & Tolstoy, 2000)).

[1] A note on nomenclature: Many papers on intermediate-mass stellar evolution use the term M_{up}. In general, this refers to the maximum progenitor mass for which a non-degenerate carbon-oxygen core develops and ignites during the latter stages of stellar evolution. Some authors use M_{up} to refer to the upper progenitor mass for which a white dwarf remnant is formed, but these two numbers are not necessarily the same.

The value of $M_{\rm crit}$ is a vital but often-overlooked component to supernova feedback studies. For a Salpeter initial-mass function (IMF) (Salpeter, 1955) in an instantaneous burst of star formation, decreasing $M_{\rm crit}$ from $8M_{\odot}$ to $5M_{\odot}$ increases the number of core-collapse supernovae by $\sim 90\%$, and the length of time over which supernovae occur increases from $\sim$ 40Myr to $\sim$ 125Myr. The result of a decrease in $M_{\rm crit}$ is therefore an increase in the amount of kinetic energy injected in to the ISM over longer periods of time. In low-mass systems, this extra energy would increase the strength and duration of any galactic winds, resulting in a higher loss of gas mass from a dwarf galaxy of a given mass (Dekel & Silk, 1986). This extra kinetic energy would also increase the amount of energy deposited in the intergalactic medium (IGM). In fact, some observations of the IGM suggest that it is more energetic than would be expected from energy due to supernovae with $M_{\rm crit} = 8M_{\odot}$ (Binney, 2001). This could be alleviated with a decrease in $M_{\rm crit}$, although AGN likely contribute some energy to the IGM (Begelman, 2001).

Since supernovae are easily observed, one obvious method for determining $M_{\rm crit}$ is to compare observed supernova rates to those expected from various values of $M_{\rm crit}$. This is a difficult exercise, as observed supernova rates in the Milky Way and other galaxies are sensitive to corrections for extinction and other selection effects, and expected supernova rates are sensitive to input star formation rates and IMFs, among other factors. Historically-observed supernovae have occurred at a higher rate than would be expected for observed mass functions in the solar neighborhood and $M_{\rm crit} = 8M_{\odot}$ (van den Bergh & Tammann, 1991). A lower value of $M_{\rm crit}$ could explain this discrepancy, but other possibilities, such as a less-steep IMF or the solar system being located near a spiral arm, could also resolve the discrepancy (Dragicevich et al., 1999).

An alternative method for determining $M_{\rm crit}$ is to determine the most massive progenitor masses for white dwarfs. This mass provides a firm lower limit to $M_{\rm crit}$, though it may be metallicity dependent (e.g. Bono, 2000 and references therein). In general, it is not possible to determine the initial mass of WDs in the field, unless they are part of a non-interacting binary system, in which case the cooling age of the WD and the companion star mass can be used to place lower limits on the progenitor star mass. If, however, the WD is located in a system of co-eval stars for which an age of the system can be determined, i.e. an open (galactic) or globular star cluster, it becomes possible to derive an initial mass as described below.

1.2 The initial-final mass relation

The initial-final mass relation for white dwarfs relates the zero-age main sequence mass for the WD progenitor with the final mass of the WD. The initial-final mass rela-

tion gives the *integrated* mass loss over the entire evolution of the progenitor star. This mass may have been lost through any of several stages of stellar evolution, including stellar winds during the main-sequence, red giant, and asymptotic giant branch phases of evolution, as well as during the final planetary-nebula ejection.

The amount of mass lost is critical to understanding the evolution of the interstellar medium, especially that in elliptical galaxies, where the majority of the hot ISM is presumed to come from stellar mass loss (Brighenti & Mathews, 1998; Mathews, 1989). The initial-final mass relation is not currently well-constrained (Weidemann, 2000). For stars currently evolving off the main sequence in the oldest stellar populations ($M_* \lesssim 1 M_\odot$), the uncertainty in the integrated mass lost is $\gtrsim 20\%$. For higher progenitor masses, the absolute scatter in final masses is $\sim 0.1 M_\odot$ for both modeled and observed initial-final mass relationships (Weidemann, 2000).

There are a variety of methods for deriving theoretical initial-final mass relationships. These methods are discussed in Weidemann (2000). Differences among models result from different methods of evolving stars through the thermally-pulsing asymptotic giant branch (AGB). Differences in the strength and modeling methods of convective overshoot also affect the core masses, with the general trend that stronger overshoot results in more massive carbon-oxygen cores for a given progenitor mass.

Observationally, the initial-final mass relation is derived semi-empirically. If a WD is in a system with coeval stars of known ages and masses (such as a star cluster), it is possible to derive the progenitor mass. The WD effective temperature and surface gravity are measured from analysis of the WD spectrum. Given evolutionary models for WDs, the cooling age of the WD can then be derived. Comparison of the WD cooling age to the age of the star cluster gives the pre-WD lifetime of the progenitor star, which includes post-main sequence evolution. Given stellar evolutionary models, one then determines which mass of progenitor star has an evolutionary lifetime equal to the pre-WD lifetime of the WD – the initial mass. Both the theoretical and observational initial-final mass relations are highly model-dependent, and slight changes the input models can lead to significant changes in the derived relation (c.f. Jeffries, 1997 and Claver et al., 2001).

Another outstanding question is whether or not the initial-final mass relation is single-valued. While not often discussed in detail, it is conceivable that parameters such as rotation may affect the final WD mass. Currently it is difficult to determine to what degree these effects increase the scatter in the initial-final mass relation.

1.3 Critical review of open cluster white dwarf studies

The concept of using white dwarfs in open clusters as probes of the maximum mass of WD progenitors, hereafter referred to as M_w, was first championed by Tinsley

(1974) and van den Hueval (1975) in studies of the Hyades. Their work suggested $M_w \lesssim 4M_\odot$, though this limit was very uncertain due to the advanced age of the Hyades and intrinsic faintness of WDs. [2].

Romanishin and Angel (1980, hereafter RA80) determined $M_{\rm crit} \geq 5M_\odot$ based on photographic plate observations of four open clusters. They compared the numbers of faint blue objects in cluster images to the numbers in adjacent comparison fields. The excess number of objects is then compared to the number of WDs expected given an assumed IMF and the number of observed main-sequence stars. The major limitations of this study were the faint limit of the photometry ($M_{V,faint} \sim 10.5$), as the most massive WDs ($M_{WD} \approx 1M_\odot$) fade below this limit within 25 Myr, and the lack of quantitative photometry for many of the blue objects, thereby precluding at least a perfunctory rejection of background / foreground contamination.

The analysis in RA80 raises many important concerns that must be considered in any photometric WD search. First, they recognized that WDs in binary systems are very difficult to detect by color selection, unless the companion is very low mass. Another concern is the dynamical evolution of the star cluster; WDs may preferentially evaporate in comparison to the remaining high-mass main sequence cluster members. These concerns will be discussed in more detail later.

A series of papers by Koester & Reimers (Koester & Reimers, 1981; Reimers & Koester, 1982; Koester & Reimers, 1985; Reimers & Koester, 1988; Reimers & Koester, 1989; Koester & Reimers, 1993; Reimers & Koester, 1994; Koester & Reimers, 1996) took spectra of many of the RA80 WD candidates. While often suffering from low signal-to-noise, these papers led to confirmation of many candidates as WDs, and they provided the first estimates of physical parameters for these WDs: the effective temperature, $T_{\rm eff}$, and surface gravity, $\log g$. Their work on the cluster NGC 2516 (Koester & Reimers, 1996) placed a lower limit on M_w, with $M_w \gtrsim 7.0M_\odot$. This lower limit is sensitive to the adopted stellar evolutionary models.

The WDs in several other open clusters have since been studied by various authors, including M34 and Praesepe (Anthony-Twarog, 1982), the Hyades (Weidemann et al., 1992), M67 (Richer et al., 1998; Williams et al., 2001), and NGC 2099 (Kalirai et al., 2001b), among others. Most recently, a careful study of WDs in Praesepe was undertaken by Claver et al. (2001). This study used $UBVI$ photometry to identify candidate WDs, with high signal-to-noise follow-up spectroscopy of the WD candidates. The spectra of confirmed WDs were then analyzed by the Balmer-line fitting methods of Bergeron, Saffer, and Liebert (1992), from which $T_{\rm eff}$ and $\log g$ were determined and

[2] Another note on nomenclature: The symbol M_w or m_w is used in many papers, including Romanishin & Angel (1980); Weidemann (2000) uses M_{up}; Anthony-Twarog (1982) uses $\mathcal{M}_{wd}$. In this dissertation, M_w refers to the maximum mass of a progenitor star which forms a white dwarf. Unless there is an unexpected stage of stellar evolution, $M_w = M_{\rm crit}$. To be conservative, these two symbols will not be used interchangeably.

the WD mass derived. Through the use of stellar evolutionary models, an empirical initial-final mass relation was derived.

1.4 The program

Because the value of M_w and the initial-final mass relationship are of fundamental importance to several areas of astrophysics, ranging from details of stellar evolution through the evolution of dwarf galaxies and the IGM, it is necessary to devise a careful, methodical study of these parameters. White dwarfs in open star clusters provide several advantages to such a study. First, their membership in a single-metallicity, coeval population of stars provides numerous constraints on the adopted models, and thereby results in the tightest possible constraints on the derived parameters. Second, numerous open clusters spanning a variety of ages and metallicities are located relatively nearby, permitting even the faintest member white dwarfs to be studied with high signal-to-noise spectroscopy, a distinct advantage over globular clusters, the other obvious coeval populations of stars in the galaxy.

Until recently, the study of open cluster WDs has been limited due to the small field of view of modern CCD imagers. The most well-studied white dwarf populations were chosen from photographic plate studies, which limited the observer to either the nearest star clusters – the Hyades, Pleiades, and Praesepe – or to the brightest WDs in more distant clusters. The main limitations of these surveys have been small-number statistics. The Pleiades contains a single, massive white dwarf, but the distance to the cluster is uncertain enough, with nearly a 0.5 mag discrepancy between Hipparcos parallaxes and main-sequence fitting distances (Stello & Nissen, 2001), that the WD age and progenitor mass are not well-constrained. The Hyades sample appears to contain too few faint WDs, a result explained in the literature as likely incompleteness and possible dynamical effects (Claver et al., 2001), though this will be discussed later. The Praesepe sample does not extend faint enough to reach the faintest expected WDs (Claver et al., 2001). New wide-field CCD cameras permit more distant clusters to be surveyed for WDs to magnitudes well-below the faintest expected white dwarfs in relatively short times, permitting complete samples of WDs to be created for a larger numbers of clusters.

The goals of this program are as follows:

- To develop a sample of nearby open clusters spanning a wide range of ages yet near enough to permit high signal-to-noise spectroscopy of the faintest expected WD candidates,
- To obtain deep photometric observations of open clusters in the above sample, and thereby derive a complete sample of WD candidates in each cluster,

- To obtain high signal-to-noise spectroscopy of each white dwarf candidate, thereby confirming its white dwarf nature and cluster membership and determining the effective temperature and surface gravity, and

- To combine these data with the best-available theoretical stellar and white-dwarf evolutionary models in order to determine the initial and final mass of each white dwarf, and thereby obtain an empirical initial-final mass relation and limits on the value of M_w.

The metallicity dependence of M_w and the initial-final mass relation is also an ultimate goal of this program; however, this remains outside the scope of this dissertation. The details of the method used to achieve these goals are presented in the following chapter.

Chapter 2

The Cluster Sample

The careful construction of a sample of open clusters for the study of white dwarfs and their progenitors is crucial to the success of this project. There are several points of consideration which led to the final open cluster sample:

- *Declination.* — As the Keck Observatory was to be used to obtain spectra of candidate WDs, the cluster sample includes only those clusters with declinations within 45° of the latitude of the observatory, specifically, $-25^\circ \leq \delta \leq +65^\circ$.

- *Angular extent.* — Nearby open clusters subtend fairly large areas of sky, with diameters up to $\gtrsim 6^\circ$ (α Per). The wide-field imager used in this project, the Lick Observatory Prime Focus Camera (PFCam), has a field-of-view of $10' \times 10'$, much too small to image significant areas of the largest open clusters with reasonable amounts of observing time. The cluster sample was therefore limited to open clusters with angular diameters $\leq 80'$. While clusters with angular diameters $\gtrsim 30'$ are too large to image with a reasonable number of pointings of PFCam, larger clusters were included in case further imaging work were to make use of larger mosaic cameras, such as the NOAO CCD mosaic ($36' \times 36'$ FOV) and the CFH12K mosaic camera.

- *Age.* – Cluster white dwarfs will not be found in open clusters in which stars with mass $M_* = M_w$ have not yet completed their evolution. Although the exact value of M_w is not well known, it is generally assumed to be less than $9M_\odot$. Therefore, the sample did not include clusters with turnoff masses higher than $9M_\odot$. From the isochrones of Girardi et al. (Girardi et al., 2002), this corresponds to an age limit of $\log(\mathrm{age}) \gtrsim 7.5$.

- *Magnitude Limit.* — The magnitude limit for this sample was constrained most tightly by the U-band photometry. If the assumption is made that the observa-

tions will be sky-noise dominated, then the signal-to-noise ratio $\frac{\mathrm{S}}{\mathrm{N}}$ for an object is

$$\frac{\mathrm{S}}{\mathrm{N}} \approx \frac{R_* t}{(R_* t + R_{\mathrm{sky}} t\, n_{\mathrm{pix}})^{1/2}}, \tag{2.1}$$

where R_* is the count rate of the object in e^-/sec, R_{sky} is the count rate of the sky in e^-/sec/pixel, n_{pix} is the number of pixels covered by the object, and t is the exposure time. If the count rate is R_0 for a reference object with magnitude m_{ref}, then the count rate for an object of magnitude m is:

$$R_* = R_0 10^{-0.4(m-m_{\mathrm{ref}})}\ . \tag{2.2}$$

Placing this in Eq. 2.1 and solving for $m_{\mathrm{lim}} = m$,

$$m_{\mathrm{lim}} = m_{\mathrm{ref}} - 2.5 \log \left[\frac{(\frac{\mathrm{S}}{\mathrm{N}})}{2R_0 t} + \frac{1}{2R_0} \sqrt{\frac{(\frac{\mathrm{S}}{\mathrm{N}})^4}{t^2} + \frac{4(\frac{\mathrm{S}}{\mathrm{N}})^2 R_{\mathrm{sky}} n_{\mathrm{pix}}}{t}} \right]\ . \tag{2.3}$$

For PFCam in the U-band, $R_{\mathrm{sky}} = 1.4$ (dark) and $R_0 = 36$ for $U_{\mathrm{ref}} = 20$ (Bolte, personal communication). For the desired photometric accuracy of 0.1 mags, $\frac{\mathrm{S}}{\mathrm{N}} \approx 10.9$. If the total exposure time is limited to 1800s and the typical seeing $\mathrm{FWHM} = 1\farcs5$, the limiting magnitude is $U_{\mathrm{lim}} \approx 22.7$. For the coolest expected WDs, $U-V \approx -0.3$ (see §3.1). This puts a magnitude limit of $V \approx 23$ on the photometry.

The V magnitude of the faintest WD in a cluster depends on four quantities: the distance of the cluster, the line-of-sight extinction to the cluster, the WD mass, and the WD cooling age. Whereas the first two quantities are available from published cluster data, the WD mass and cooling age must be estimated from WD cooling models. In order to ensure a complete sample of WDs in a given cluster, the V-band magnitude of the faintest expected WD must be estimated independently for each cluster. Due to the mass-radius relation for WDs, more massive WDs have a smaller radius, and therefore are less luminous for a given effective temperature. Therefore, the most-massive available WD models ($1.0 M_\odot$) were used. As the cooling age of a cluster WD must be less than the cluster age, and since WDs fade as they cool, the V-band magnitude was estimated from models assuming a cooling age equal to the cluster age.

It is desirable to extend the photometry at least 1 mag fainter than the faintest expected WD in order to ensure that the WD cooling sequence terminates where expected. Based on our photometric limits, this requires that $V_{\mathrm{WD,faint}} \lesssim 22$. Therefore, the cluster catalog was selected to include only those WDs for which the faintest expected WD has $V \lesssim 22$.

The open cluster sample was selected using these criteria from the web-based open cluster database, WEBDA (Mermilliod, 1995). The final catalog contains 34 open clusters and is presented in Table 2.1. It should be noted that the listed parameters (distance, age, metallicity, etc.) may be quite uncertain.

Table 2.1: Open clusters in the sample fulfilling the criteria in the text.

Cluster Name	RA (J2000)	Dec (J2000)	ℓ (°)	b (°)	d (pc)	$E(B-V)$	age	diam (′)	$m_{V,\mathrm{faint}}$	Richness Class[a]
NGC 225	00:43:26	+61:47	122.0	-01.1	657	0.274	8.114	14	21.4	2
Collinder 463	01:48:23	+71:57	127.4	+09.6	702	0.259	8.373	29	21.8	2
NGC 752	01:57:47	+37:41	137.2	-23.4	457	0.034	9.050	75	21.1	2
Stock 2	02:14:59	+59:16	133.4	-01.9	303	0.380	8.230	45	21.3	4
Trumpler 2	02:37:18	+55:59	137.4	-03.9	651	0.324	8.169	17	21.5	3
NGC 1039 (M34)	02:42:03	+42:47	143.6	-15.6	499	0.070	8.249	25	20.3	2
NGC 1027	02:42:41	+61:33	135.8	+01.5	772	0.325	8.203	14	21.9	2
IC 348	03:44:33	+32:17	160.4	-17.7	385	0.929	7.641	7	21.6	1
NGC 1647	04:46:02	+19:04	180.4	-16.8	540	0.370	8.158	39	21.2	3
NGC 1662	04:48:28	+10:56	187.7	-21.1	437	0.304	8.625	12	21.2	1.5
NGC 2168 (M35)	06:08:52	+24:20	186.6	+02.2	816	0.262	7.979	25	21.6	4
NGC 2232	06:26:34	-04:45	214.4	-07.7	359	0.030	7.727	45	18.7	1
NGC 2287 (M41)	06:47:03	-20:44	231.1	-10.2	693	0.027	8.385	39	21.1	2.5
NGC 2281	06:49:19	+41:03	175.0	+17.1	558	0.063	8.554	25	20.9	2.5
NGC 2301	06:51:46	+00:27	212.6	+00.3	872	0.028	8.216	14	21.3	1
NGC 2302	06:51:56	-07:04	219.3	-03.1	1182	0.207	7.847	5	21.9	1
NGC 2323 (M50)	07:03:12	-08:20	221.7	-01.2	929	0.213	8.096	14	21.9	3
NGC 2353	07:14:34	-10:18	224.7	+00.4	1119	0.072	7.974	18	21.7	2
NGC 2395	07:27:07	+13:35	204.6	+14.0	512	0.120	9.070	14	21.6	1
Bochum 4	07:31:03	-16:57	232.5	+00.8	872	0.194	7.545	15	21.0	1
NGC 2422 (M47)	07:36:36	-14:29	231.0	+03.1	490	0.070	7.861	25	19.7	1

[a] Richness Class as given in Janes & Adler (1982)

Table 2.1: (cont.)

Cluster Name	RA (J2000)	Dec (J2000)	ℓ	b	d (pc)	$E(B-V)$	age	diam ($'$)	$m_{V,\mathrm{faint}}$	Richness Class[a]
NGC 2548 (M48)	08:13:46	-05:48	227.9	+15.4	769	0.031	8.557	29	21.5	1
NGC 2632 (M44)	08:40:04	+19:59	205.5	+32.5	187	0.009	8.863	70	18.8	4
IC 4665	17:46:15	+05:43	30.6	+17.1	352	0.174	7.634	70	18.9	2
NGC 6633	18:27:44	+06:34	36.1	+08.3	376	0.182	8.629	20	20.6	3
IC 4725 (M25)	18:31:39	-19:15	13.6	-04.5	620	0.473	7.965	29	21.6	3
IC 4756	18:38:57	+05:27	36.4	+05.3	484	0.192	8.699	39	21.3	3
Stephenson 1	18:53:33	+36:55	66.9	+15.5	390	0.040	7.731	20	18.9	1
NGC 6716	18:54:33	-19:53	15.4	-09.6	789	0.220	7.961	10	21.3	2
Roslund 5	20:10:02	+33:46	71.4	+00.3	389	0.098	7.832	50	19.2	⋯
NGC 7039	21:11:12	+45:39	88.0	-01.7	951	0.131	7.820	14	21.2	2
NGC 7063	21:24:27	+36:30	83.1	-09.9	689	0.091	7.977	9	20.7	3
NGC 7092 (M32)	21:32:12	+48:26	92.5	-02.3	326	0.013	8.445	29	19.4	1
NGC 7243	22:15:17	+49:53	98.9	-05.6	808	0.220	8.058	29	21.5	2

[a] Richness Class as given in Janes & Adler (1982)

Chapter 3

Photometry: Approach, Observations, and Analysis

3.1 White Dwarf Models

Photometric indices for WD models have been published for WDs of a constant $\log g$ (Bergeron et al., 1995b). Cooling WDs do not maintain a constant surface gravity; WDs shrink as they cool, resulting in an increasing surface gravity for a constant WD mass. To study WDs of a given mass, it is necessary to calculate the photometric indices.

As described in Chapter 1, the W95 C/O models are used for the WD evolutionary models. Synthetic spectra of pure-hydrogen (DA) atmospheric models are kindly provided by D. Koester Details of an earlier version of these constantly-updated atmospheric models are published in Finley, Koester, & Basri (1997). These synthetic spectra were used in conjunction with the W95 models to determine the UBV photometric indices in the following manner.

The bolometric correction, BC, is defined as

$$BC = m_{bol} - V, \tag{3.1}$$

where m_{bol} is the apparent bolometric magnitude. Using the definition of the magnitude system,

$$m_X - m_{X,\odot} = -2.5 \log \frac{\int_0^\infty f_\lambda S_X(\lambda) d\lambda}{\int_0^\infty f_\lambda^\odot S_X(\lambda) d\lambda}, \tag{3.2}$$

where f_λ is the observed flux distribution above Earth's atmosphere and $S_X(\lambda)$ is the response function of filter X,

$$BC = 2.5 \log \frac{\int_0^\infty f_\lambda S_V(\lambda) d\lambda}{\int_0^\infty f_\lambda d\lambda} - 2.5 \log \frac{\int_0^\infty f_\lambda^\odot S_V(\lambda) d\lambda}{f^\odot} + BC_\odot, \tag{3.3}$$

where $f^{\odot}$ is the solar constant and $BC_{\odot}$ is the bolometric correction for the sun.

Since

$$V_{\odot} - V_{Vega} = -2.5\log(\int_0^{\infty} f_{\lambda}^{\odot} S_V(\lambda)d\lambda) + 2.5\log(\int_0^{\infty} f_{\lambda}^{Vega} S_V(\lambda)d\lambda), \quad (3.4)$$

and by canceling the distance and radius dependences in the f_{λ} terms, the bolometric correction equation becomes

$$BC = 2.5\log\frac{\int_0^{\infty} H_{\lambda} S_V(\lambda)d\lambda}{\frac{1}{4\pi}\sigma T_{\rm eff}^4} - 2.5\log\frac{\int_0^{\infty} f_{\lambda}^{Vega} S_V(\lambda)d\lambda}{f^{\odot}} + V_{\odot} - V_{Vega} + BC_{\odot}, \quad (3.5)$$

where H_{λ} is the Eddington flux from the model atmosphere.

Using the measured flux of Vega from Hayes (1985), $V_{\odot} = -26.76$, $V_{Vega} = 0.03$, $BC_{\odot} = -0.07$, and $f^{\odot} = 1.371 \times 10^6$ erg/cm^2/s (Bessell et al., 1998), this equation reduces to

$$BC = 2.5\log\frac{\int_0^{\infty} H_{\lambda} S_V(\lambda)d\lambda}{\frac{1}{4\pi}\sigma T_{\rm eff}^4} + 2.220. \quad (3.6)$$

The bolometric magnitude of a model WD is simply

$$M_{bol} = -2.5\log\frac{L}{L_{\odot}} + M_{bol}^{\odot}, \quad (3.7)$$

where $L = 4\pi R^2 \sigma T_{\rm eff}^4$, $L_{\odot} = 3.8556 \times 10^{33}$ erg/s, and $M_{bol}^{\odot} = 4.74$ (Bessell et al., 1998). R is the WD radius from the cooling models. From M_{bol}, M_V is determined via Eq. 3.1.

A color index $X - Y$ is determined from the equation

$$X - Y = -2.5\log\frac{\int_0^{\infty} H_{\lambda} S_X(\lambda)d\lambda}{\int_0^{\infty} H_{\lambda} S_Y(\lambda)d\lambda} + C_{X-Y}, \quad (3.8)$$

where C_{X-Y} is determined from the Vega fluxes of Hayes (1985). For this work, $(U-B)_{Vega}$=-0.005 and $(B-V)_{Vega}$=-0.003, values assumed by Kurucz (Kurucz, 1979) as the indices of Vega. It is noted that several different observed values of these indices have been used (e.g. Castelli 1999), all within 0.007 mag of the adopted values. Any change in the adopted color indices for Vega are additive to the calculated WD indices.

The Koester synthetic spectra are tabulated for $50000\text{K} \geq T_{\rm eff} \geq 10000\text{K}$ and $9.0 \geq \log g \geq 7.0$. The provided spectra only contain data from 3300Å$\leq \lambda \leq$ 8000Å, whereas the U-band filter response continues to $\sim$ 3000Å. Therefore, the U-band integrals are not evaluated blueward of 3300Å. The net effect of this should be a small underestimate of the U-band magnitude most noticeable for the hottest WDs.

Photometric indices were calculated for each provided synthetic spectrum. To obtain the evolutionary sequences of photometric indices for WDs of constant mass, the surface gravity for each WD mass at each tabulated $T_{\rm eff}$ was interpolated from the W95 models. A two-dimensional spline interpolation (Press et al., 1992) in $T_{\rm eff}$ and $\log g$ was then used to determine the photometric indices, which are presented in Tables 3.1-3.7.

These photometric indices can be compared with those of Bergeron et al. (Bergeron et al., 1995b). Figure 3.1 compares the results in the $B-V$ color-magnitude diagram (CMD). The new calculations match well with the previously published results. For a given $T_{\rm eff}$, the Bergeron et al. (1995b) $B-V$ are about 0.01 mags bluer; this is due to differences in the assumed values for $V_{\odot}$ and $BC_{\odot}$. Figure 3.2 compares the two sets of indices in the $B-V$, $U-B$ color-color plane. Here significant (0.04 mag) differences are seen between the Bergeron et al. (1995b) indices and these calculations among the hotter WDs, with the current indices being redder. This could be due to the effect of not integrating the U-band fluxes blueward of 3300Å. Also, as mentioned in the discussion in Finley et al. (1997), differences between the Bergeron models and Koester models are apparent for the hottest stars, though the reasons for these differences are uncertain.

3.2 Main-sequence models

For the clusters in this sample, the ages and distances are determined by isochrone fitting. The derived distances and ages for the clusters vary depending upon the isochrone input physics. This implies that the derived initial-final mass relation will also vary depending on the isochrones used. For this work, the theoretical isochrones of Girardi et al. (2002) are used. The Y^2 isochrones (Yi et al., 2001) do not include the upper main sequence for young clusters ($M > 5M_{\odot}$), and so are not useful in studying progenitors with masses in this interesting range.

The Girardi et al. (2002) isochrones are calculated with moderate convective overshooting and a range of metallicities. There is also a set of solar-metallicity isochrones with no convective overshoot. For most of the sample clusters, the metallicities are poorly determined or controversial. Therefore, for each WD, the progenitor mass will be determined using stellar evolutionary models for a range of metallicities ($Z = 0.008, 0.018, 0.03$) and for the solar-metallicity models without convective overshoot. The range of initial masses thus derived will give some insight into the systematics introduced by assumptions in the metallicity and convection physics.

3.3 Observations

Imaging of several open clusters was obtained over two runs totaling five nights using the Prime Focus Camera (PFCam) on the 3-meter telescope at Lick Observatory. PFCam provides a $10' \times 10'$ field-of-view and $0''.296$ pixels using a SITe 2048×2048 thinned CCD. Images were binned 2×2 on-chip. During the September 21-23 2001 (UT) observing run, seeing was excellent for Lick Observatory, averaging around $0''.8$ in all bands. This resulted in moderately undersampled images of point sources. The weather was photometric only for the second night, with high thin cirrus on the other nights. During this run, the PFCam shutter timing was unreliable, with random errors in exposure times estimated at ~ 0.5 seconds. Fields in each cluster were tiled to cover as large of an area of the cluster as possible.

A second PFCam run on Sept. 7-8, 2002 obtained additional images. Weather was photometric both nights. Seeing was $\sim 2''$ on the first night, and steadily improved during the second night from $2''$ to $\sim 1''$.

Due to the shutter errors, weather, and saturation of the brightest stars on the shortest images, several fields in each cluster were imaged as calibrations using the Nickel Imager on the 1-meter Nickel telescope at Lick Observatory during a photometric observing run on July 6-8 2002. The imager has a field of view of $\sim 6' \times 6'$ using an LL thinned 2048×2048 CCD with $0''.18$ pixels. Images were binned 2×2, and seeing was highly variable, ranging from $1''.5$ to $\gtrsim 4''$. The fields were chosen to include the brightest cluster stars.

As the clusters IC 4665, NGC 6633, and NGC 1039 (M34) have too large of an angular extent to tile completely with PFCam, BV images of these clusters from the CFHT CFH12K archive were obtained. The observations of these clusters are described in Kalirai et al. (2001a).

Observing logs for the clusters presented in this paper are listed in Table 3.8. The imaged fields are indicated in Figs. 3.3-3.7. Figs. 3.8 and 3.9 show composite color images of the PFCam fields in NGC 2168 and NGC 7063, respectively.

3.4 Image reduction and photometric analysis

Images were reduced using the Image Reduction and Analysis Facility (IRAF) in standard fashion. Bias levels were determined for each frame using a third-order Legendre polynomial fit to the image overscan and were subtracted. Images of the twilight sky were used to construct a flat field in each band. Program frames were corrected for efficiency variations on all spatial scales by dividing them by the appropriate, normalized flat field image. Multiple images of the same program field with the same exposure time were registered and were combined by rejecting the highest pixel and

averaging the remaining values.

Photometry was obtained for the PFCam and CFHT images using the PSF-fitting routines of DAOPHOT II (Stetson, 1992). DAOPHOT determines the point-spread function (PSF) by fitting an analytic function and an empirically-determined lookup table to selected PSF stars. For these fields, the PSF was determined separately for each frame, and was permitted to vary quadratically across the frame. The analytic function was selected by selecting the functional form which minimized the χ^2 fits of the PSF stars to the model PSF.

As the stellar fields are crowded, ALLSTAR was used to redetermine photometry and subtract detected stars from each frame. A second detection and photometry run was then used to detect and analyze any previously-hidden stars.

The goodness-of-fit for the PSF is given by the DAOPHOT output χ, which is the observed pixel-to-pixel scatter divided by pixel-to-pixel scatter expected from Poisson noise from the object flux and the measured background noise. In theory, points sources should exhibit a scatter about $\chi = 1.0$, and extended objects should have relatively high χ values. In these data, the χ value for point sources increases for bright objects, due either to an imperfect PSF or an error in the input CCD gain. In order to separate out non-point sources from the sample, a fourth-order polynomial was fit to and subtracted from the chi values in each cluster. A χ-cut was then made to remove those points with highly-discrepant residuals.

The resultant PFCam photometry reveals a substantial non-linearity in the images from the Sept. 2001 observing run. Fig. 3.10 compares the (instrumental) magnitudes obtained from NGC 7063 in a 30-second B-band exposure with those obtained in a 120-second exposure. For a linear CCD response, the plot should show a scatter about a constant value (zero in this case). For these images, a trend in the magnitude offset with magnitude is observed, indicating a non-linear CCD response. This trend has only a weak spatial dependence, indicating that shutter problems are not the cause of the non-linearity. The image headers indicate nothing unusual, such as voltage or temperature fluctuations. The non-linearity is observed in all frames except for the images of NGC 2168. Analysis of the unprocessed frames also contained the non-linearity, indicating that image processing was not the cause. Subsequent testing of PFCam has failed to detect any non-linearity in the CCD response.

The only data for this dissertation affected by the non-linearity were the NGC 7063 images. Therefore, the 2002 NGC 7063 data were compared with those of 2001, and a linear function was fit to the magnitude differences to compensate for the non-linear response.

The CFHT images presented some minor challenges. Flat fields taken during the same observing run were taken in areas of high stellar background, and it was not possible to create flat fields free of features due to residual stars. Therefore, flat fields

were constructed from archived flat fields from a subsequent CFH12K archived run. Also, since only one long exposure was taken in each frame, the inter-chip gaps and cosmic rays remain, the net result of which was numerous spurious source detections. One chip in the CFH12K mosaic contained sufficient bad columns that it was not possible to obtain useful photometry from that chip; therefore, data on that chip were ignored.

3.4.1 Calibrations

Because of the shutter timing errors and non-photometric weather experienced during the PFCam runs, and because the photometric quality of the archival CFHT data is unstated, it was necessary to establish local calibrator stars for each cluster.

The Nickel images were used for this purpose. After being reduced as stated above, photometry was obtained using the aperture photometry routines of DAOPHOT. For each frame, instrumental magnitudes and aperture corrections were determined. Images of several Landolt standard fields (Landolt, 1992) were used to establish the photometric calibration coefficients in Eqns. 3.9-3.11. Each field was then calibrated using the equations

$$u = U + A_0 + A_1(U-B) + A_2(X-1.25) + A_3T - 2.5\log t_{exp} \quad (3.9)$$

$$b = B + B_0 + B_1(B-V) + B_2(X-1.25) + B_3T - 2.5\log t_{exp} \quad (3.10)$$

$$v = V + C_0 + C_1(B-V) + C_2(X-1.25) + C_3T - 2.5\log t_{exp} \quad (3.11)$$

where u, b, v are the instrumental magnitudes, U, B, V are the standard-system magnitudes, X is the airmass, T is the time, and $A_0 \ldots C_3$ are the coefficients to be determined. The coefficients were determined via least-squares fitting.

Color terms were determined first by permitting the zero points to vary from frame to frame and solving the equations. The color terms were then fixed, and each night's frames were reduced separately to obtain zero points, airmass terms, and time variance. B_3 and C_3 were found to be near zero, and the inclusion of these terms in the fit increased the errors in the other terms, so B_3 and C_3 were set equal to zero for the final determination. The values from the final fit are given in Tab. 3.9.

U-band calibrations for 2002 July 6 & 7 have large errors in absolute zero-points due to a lack of well-measured U-band standards in the observed standard fields SA 110 and SA 112. On 2002 July 8, PG 1633 was used as the primary standard field, resulting in much tighter U-band solutions. For this reason, U-band data for the first two nights were shifted to produce the tightest possible main sequences in the program clusters on a cluster-by-cluster basis.

The calibrations were then applied to the Nickel observations of open cluster fields to bring the observed cluster stars onto the standard system. These stars were then used

as local calibration stars to calibrate the PFCam and CFHT images by solving modified versions of Eqns. 3.9 including only the zero point and color terms. Zero points were allowed to float from frame to frame. The color terms for PFCam and CFH12K are given in Tab. 3.9.

As no Nickel images were obtained for NGC 2168, the photometry of Sung & Bessell (1999) was used to calibrate the PFCam images of this cluster. The PFCam color terms determined from this calibration agreed with those determined from the Nickel-calibrated fields.

3.4.2 Distances, reddening and ages

Determination of the initial-final mass relation and M_w requires knowledge of the cluster age, distance, and reddening, quantities which are often poorly determined. An ultimate goal of this research is to obtain distance, reddening, and age information from the Nickel photometry of the upper main sequence stars. That work has not yet been completed, so it is necessary to use the best available published numbers.

NGC 1039 (M34). — According to Dias et al. (2002), M34 has a distance modulus $(m-M)_0 = 8.50$, $E(B-V) = 0.070$, and a logarithmic age of 8.249. Jones & Prosser (1996) find a distance modulus of $(m-M)_0 = 8.38$, $E(B-V) = 0.070$, and a logarithmic age of between 8.30 and 8.40.

NGC 2168. — Sung & Bessel (1999) presented CCD observations of this cluster and determined $(m-M)_0 = 9.60 \pm 0.10$, $E(B-V) = 0.255 \pm 0.024$, and logarithmic age of 8.3 ± 0.3, as well as a binary fraction of 35%. The metallicity was determined to be fairly sub-solar, with $Z \approx 0.008$. Data from the WIYN Open Cluster Survey indicate $(m-M)_0 = 9.55$, $E(B-V) = 0.2$ and logarithmic age of 8.15 (von Hippel et al., 2002), while the compilation of data by Dias et al. (2002) suggests $(m-M)_0 = 9.56$, $E(B-V) = 0.262$, and logarithmic age of 7.98. The PFCam photometry data are noisy on the upper-main sequence, and Nickel data have not yet been reduced. Fig. 3.11 shows the color magnitude diagrams for isochrones with Z=0.008 and Z=0.019. While far from conclusive, these data suggest that $(m-M)_0 \approx 9.5$, $E(B-V) \approx 0.255$, and an age of ~ 8.0. Neither metallicity produces satisfactory results in either CMD, suggesting the metallicity is intermediate to these two values.

IC 4665. — No useful Nickel images were obtained for IC 4665, so the upper main sequence of Prosser (1993) was used to determine age, reddening, and distance. Dias et al. (2002) claim $(m-M)_0 = 7.73$, $E(B-V) = 0.174$ and a logarithmic age of 7.634. The Prosser data are plotted with solar-metallicity isochrones of this distance and reddening in Fig. 3.12, and the data appear to agree with the models. The age is difficult to determine accurately, but the brightest stars suggest an age of less than 7.80.

NGC 6633. — For NGC 6633, the distance and reddening were carefully determined by Jeffries et al. (2002) to be $(m-M)_0 = 8.01 \pm 0.09$ and $E(B-V) = 0.172 \pm 0.011$.[1] The metallicity of NGC 6633 was also found to be $[\mathrm{Fe/H}] = -0.096 \pm 0.081$, or slightly sub-solar.

Figure 3.13 shows the upper-main sequence region of NGC 6633. Indicated are all stars detected in the Nickel photometry as well as those stars found to be proper motion members by Sanders (1973). Also indicated are four brighter proper motion members stars without Nickel photometric measurements due to saturation. Two of these objects appear to be potential blue stragglers (SAN 194 and SAN 258), and the other two are evolved members. The age of NGC 6633 is estimated through the use of Girardi et al. (2002) solar-metallicity isochrones to be $\log(\mathrm{age}) = 8.675 \pm 0.025$. This is significantly lower than the previously-published value of 8.82 published by Janes, Tilley, & Lyngå(1988) but older than the 8.629 quoted by Dias et al. (2002).

NGC 7063. — Little work has been done on this cluster. The values for the age, distance, and reddening quoted in Dias et al. (2002) are $(m - M)_0 = 9.191$, $E(B - V) = 0.091$, and logarithmic age of 7.977. Figure 3.14 shows the upper main sequence of NGC 7063. Proper motion members cluster members (Dias et al., 2002; Glushkova & Uglova, 1997) are indicated, as are solar-metallicity isochrones for ages of 8.0 and 8.15. While sparse, the data suggest that the cluster has an age of 8.15 ± 0.05.

3.4.3 Candidate White Dwarf Selection

The preferred method to find WDs would be to select all objects with photometry within $\sim 3\sigma$ of the WD cooling sequence. This method suffers from the shortcoming that any systematic errors, such as incorrect distance modulus, reddening, model errors, etc., could result in the rejection of cluster white dwarfs from the sample. For this reason, candidate WDs were selected by their location in large regions of the color-color plane (if UBV data are available) or location in the color-magnitude diagram (if only BV data are available).

The candidates in M34 were selected from as-yet uncalibrated CMDs derived from aperture photometry of the M34 fields just prior to a spectroscopic observation run. Further photometric analysis of M34 has yet to be completed.

The resulting photometry for NGC 2168, IC 4665, NGC 6633 and NGC 7063 is presented in Figs. 3.15-3.20. Heavy contamination from galactic disk field stars is apparent in each diagram. The white dwarf candidates for each cluster are presented in Tabs. 3.10- 3.14.

[1] Quoted values are for the "long" Pleiades modulus of 5.60 and assume a color-independent color excess.

Table 3.1: Calculated photometric indices for $0.4M_{\odot}$ W95 white dwarf cooling model.

$T_{\rm eff}$	log (age)	$\log g$	$M_{\rm bol}$	B.C.	M_V	$B-V$	$U-B$
50000	5.569	7.122	3.076	-4.500	7.576	-0.278	-1.183
45000	5.922	7.194	3.714	-4.150	7.864	-0.269	-1.171
40000	6.274	7.266	4.406	-3.774	8.181	-0.255	-1.154
35000	6.595	7.336	5.160	-3.383	8.543	-0.234	-1.125
30000	6.887	7.399	5.988	-3.012	8.999	-0.194	-1.063
28000	7.006	7.424	6.348	-2.860	9.208	-0.172	-1.025
26000	7.128	7.447	6.729	-2.688	9.417	-0.147	-0.984
24000	7.256	7.470	7.134	-2.487	9.621	-0.121	-0.941
22000	7.398	7.492	7.567	-2.261	9.828	-0.092	-0.892
20000	7.559	7.513	8.034	-2.010	10.043	-0.058	-0.833
19000	7.647	7.524	8.282	-1.873	10.155	-0.039	-0.799
18000	7.742	7.534	8.543	-1.729	10.272	-0.018	-0.762
17000	7.845	7.544	8.817	-1.576	10.394	0.006	-0.721
16000	7.953	7.555	9.107	-1.415	10.522	0.033	-0.676
15000	8.060	7.564	9.410	-1.244	10.655	0.065	-0.629
14000	8.165	7.573	9.732	-1.065	10.797	0.101	-0.583
13000	8.271	7.582	10.075	-0.880	10.955	0.141	-0.541
12000	8.378	7.590	10.444	-0.684	11.129	0.176	-0.517
11000	8.487	7.599	10.843	-0.477	11.320	0.201	-0.513
10000	8.599	7.607	11.277	-0.349	11.626	0.225	-0.529

Table 3.2: Calculated photometric indices for $0.5M_{\odot}$ W95 white dwarf cooling model.

$T_{\rm eff}$	log (age)	$\log g$	$M_{\rm bol}$	B.C.	M_V	$B-V$	$U-B$
50000	6.081	7.531	3.857	-4.504	8.361	-0.274	-1.187
45000	6.283	7.575	4.423	-4.153	8.575	-0.264	-1.175
40000	6.476	7.615	5.036	-3.775	8.810	-0.250	-1.159
35000	6.678	7.653	5.711	-3.380	9.092	-0.228	-1.131
30000	6.919	7.691	6.474	-3.005	9.479	-0.187	-1.072
28000	7.031	7.705	6.810	-2.853	9.663	-0.163	-1.036
26000	7.157	7.719	7.167	-2.680	9.847	-0.137	-0.997
24000	7.302	7.733	7.548	-2.479	10.027	-0.110	-0.954
22000	7.477	7.746	7.959	-2.254	10.213	-0.080	-0.906
20000	7.673	7.759	8.405	-2.003	10.408	-0.045	-0.848
19000	7.776	7.765	8.644	-1.866	10.511	-0.026	-0.816
18000	7.881	7.772	8.895	-1.722	10.617	-0.004	-0.780
17000	7.983	7.778	9.159	-1.570	10.729	0.021	-0.740
16000	8.084	7.784	9.437	-1.408	10.845	0.050	-0.699
15000	8.182	7.790	9.732	-1.238	10.970	0.082	-0.654
14000	8.280	7.795	10.046	-1.060	11.106	0.119	-0.612
13000	8.380	7.801	10.383	-0.875	11.258	0.157	-0.578
12000	8.480	7.807	10.744	-0.672	11.417	0.185	-0.561
11000	8.583	7.813	11.136	-0.477	11.614	0.208	-0.555
10000	8.692	7.818	11.564	-0.358	11.922	0.228	-0.567

Table 3.3: Calculated photometric indices for $0.6M_{\odot}$ W95 white dwarf cooling model.

$T_{\rm eff}$	log (age)	$\log g$	$M_{\rm bol}$	B.C.	M_V	$B-V$	$U-B$
50000	6.343	7.801	4.334	-4.506	8.840	-0.271	-1.190
45000	6.452	7.830	4.863	-4.154	9.017	-0.261	-1.179
40000	6.581	7.857	5.442	-3.774	9.217	-0.247	-1.163
35000	6.755	7.884	6.090	-3.378	9.468	-0.224	-1.136
30000	6.992	7.909	6.822	-2.999	9.822	-0.182	-1.080
28000	7.118	7.918	7.145	-2.847	9.992	-0.157	-1.045
26000	7.272	7.928	7.490	-2.675	10.165	-0.130	-1.006
24000	7.457	7.937	7.861	-2.473	10.334	-0.102	-0.965
22000	7.653	7.946	8.261	-2.248	10.510	-0.071	-0.917
20000	7.853	7.956	8.700	-1.997	10.696	-0.035	-0.861
19000	7.947	7.960	8.934	-1.861	10.794	-0.015	-0.829
18000	8.039	7.965	9.180	-1.717	10.896	0.008	-0.794
17000	8.128	7.969	9.438	-1.564	11.003	0.034	-0.757
16000	8.216	7.973	9.712	-1.403	11.115	0.064	-0.716
15000	8.304	7.977	10.003	-1.234	11.237	0.097	-0.675
14000	8.393	7.982	10.314	-1.056	11.370	0.133	-0.638
13000	8.484	7.986	10.646	-0.870	11.516	0.166	-0.612
12000	8.577	7.990	11.004	-0.661	11.665	0.191	-0.598
11000	8.676	7.994	11.392	-0.479	11.871	0.211	-0.589
10000	8.783	7.999	11.817	-0.366	12.182	0.230	-0.598

Table 3.4: Calculated photometric indices for $0.7M_{\odot}$ W95 white dwarf cooling model.

$T_{\rm eff}$	log (age)	$\log g$	$M_{\rm bol}$	B.C.	M_V	$B-V$	$U-B$
50000	6.272	8.016	4.704	-4.507	9.211	-0.269	-1.192
45000	6.385	8.036	5.212	-4.154	9.366	-0.259	-1.181
40000	6.549	8.057	5.774	-3.774	9.548	-0.244	-1.166
35000	6.767	8.077	6.404	-3.376	9.780	-0.221	-1.140
30000	7.083	8.093	7.116	-2.994	10.110	-0.177	-1.087
28000	7.262	8.101	7.433	-2.842	10.275	-0.152	-1.053
26000	7.460	8.107	7.772	-2.670	10.441	-0.124	-1.015
24000	7.654	8.114	8.137	-2.468	10.605	-0.096	-0.974
22000	7.838	8.122	8.534	-2.243	10.777	-0.063	-0.928
20000	8.006	8.129	8.965	-1.992	10.957	-0.026	-0.873
19000	8.086	8.132	9.196	-1.855	11.051	-0.005	-0.842
18000	8.164	8.135	9.439	-1.711	11.150	0.019	-0.808
17000	8.243	8.139	9.695	-1.559	11.254	0.046	-0.772
16000	8.323	8.142	9.967	-1.398	11.365	0.076	-0.733
15000	8.404	8.145	10.255	-1.229	11.485	0.110	-0.696
14000	8.486	8.148	10.563	-1.052	11.615	0.144	-0.664
13000	8.573	8.152	10.893	-0.864	11.756	0.173	-0.643
12000	8.665	8.155	11.248	-0.650	11.898	0.194	-0.629
11000	8.764	8.158	11.634	-0.481	12.115	0.214	-0.617
10000	8.873	8.161	12.056	-0.373	12.429	0.230	-0.623

Table 3.5: Calculated photometric indices for $0.8M_{\odot}$ W95 white dwarf cooling model.

$T_{\rm eff}$	log (age)	$\log g$	$M_{\rm bol}$	B.C.	M_V	$B-V$	$U-B$
50000	6.226	8.204	5.028	-4.508	9.536	-0.267	-1.194
45000	6.382	8.219	5.524	-4.155	9.679	-0.257	-1.183
40000	6.585	8.235	6.075	-3.774	9.848	-0.242	-1.169
35000	6.879	8.249	6.689	-3.374	10.064	-0.218	-1.144
30000	7.336	8.262	7.392	-2.990	10.382	-0.173	-1.093
28000	7.524	8.268	7.705	-2.837	10.542	-0.147	-1.060
26000	7.695	8.273	8.041	-2.665	10.705	-0.119	-1.023
24000	7.854	8.279	8.404	-2.463	10.867	-0.089	-0.984
22000	8.000	8.285	8.796	-2.238	11.034	-0.056	-0.938
20000	8.139	8.290	9.222	-1.987	11.209	-0.018	-0.885
19000	8.209	8.292	9.452	-1.850	11.302	0.004	-0.855
18000	8.280	8.295	9.693	-1.706	11.399	0.029	-0.822
17000	8.352	8.298	9.947	-1.554	11.502	0.057	-0.787
16000	8.427	8.300	10.217	-1.394	11.611	0.087	-0.751
15000	8.504	8.303	10.504	-1.225	11.729	0.121	-0.717
14000	8.585	8.305	10.810	-1.048	11.858	0.152	-0.690
13000	8.671	8.308	11.138	-0.855	11.993	0.177	-0.672
12000	8.763	8.310	11.492	-0.643	12.135	0.197	-0.658
11000	8.863	8.313	11.876	-0.484	12.360	0.216	-0.643
10000	8.972	8.315	12.297	-0.380	12.677	0.230	-0.645

Table 3.6: Calculated photometric indices for $0.9M_{\odot}$ W95 white dwarf cooling model.

$T_{\rm eff}$	log (age)	$\log g$	$M_{\rm bol}$	B.C.	M_V	$B-V$	$U-B$
50000	6.231	8.379	5.339	-4.509	9.848	-0.266	-1.195
45000	6.436	8.392	5.827	-4.155	9.982	-0.255	-1.186
40000	6.737	8.403	6.368	-3.773	10.141	-0.240	-1.171
35000	7.192	8.414	6.975	-3.372	10.348	-0.216	-1.148
30000	7.611	8.425	7.672	-2.985	10.657	-0.170	-1.099
28000	7.752	8.430	7.983	-2.832	10.814	-0.143	-1.067
26000	7.884	8.435	8.317	-2.660	10.977	-0.114	-1.031
24000	8.009	8.439	8.675	-2.458	11.133	-0.083	-0.993
22000	8.132	8.443	9.064	-2.233	11.297	-0.049	-0.949
20000	8.258	8.447	9.488	-1.982	11.469	-0.009	-0.897
19000	8.323	8.449	9.716	-1.845	11.561	0.013	-0.867
18000	8.390	8.451	9.956	-1.702	11.657	0.039	-0.836
17000	8.460	8.453	10.209	-1.550	11.759	0.067	-0.802
16000	8.532	8.455	10.477	-1.390	11.867	0.098	-0.768
15000	8.608	8.457	10.763	-1.222	11.985	0.129	-0.739
14000	8.688	8.459	11.068	-1.044	12.112	0.157	-0.717
13000	8.773	8.462	11.395	-0.844	12.238	0.179	-0.700
12000	8.865	8.463	11.747	-0.640	12.387	0.198	-0.684
11000	8.997	8.465	12.130	-0.487	12.617	0.216	-0.666
10000	9.141	8.468	12.550	-0.387	12.937	0.229	-0.665

Table 3.7: Calculated photometric indices for $1.0 M_{\odot}$ W95 white dwarf cooling model.

$T_{\rm eff}$	log (age)	$\log g$	$M_{\rm bol}$	B.C.	M_V	$B-V$	$U-B$
50000	6.314	8.554	5.662	-4.510	10.172	-0.265	-1.197
45000	6.705	8.564	6.144	-4.155	10.299	-0.253	-1.188
40000	7.173	8.573	6.679	-3.773	10.451	-0.238	-1.174
35000	7.533	8.582	7.281	-3.371	10.652	-0.213	-1.152
30000	7.822	8.591	7.973	-2.981	10.954	-0.167	-1.105
28000	7.931	8.595	8.282	-2.827	11.109	-0.139	-1.075
26000	8.039	8.598	8.612	-2.654	11.266	-0.109	-1.040
24000	8.148	8.602	8.968	-2.452	11.421	-0.077	-1.002
22000	8.261	8.605	9.355	-2.228	11.582	-0.042	-0.959
20000	8.380	8.609	9.777	-1.976	11.754	-0.001	-0.909
19000	8.442	8.610	10.004	-1.840	11.844	0.022	-0.880
18000	8.506	8.612	10.243	-1.697	11.940	0.048	-0.850
17000	8.573	8.613	10.495	-1.545	12.040	0.077	-0.818
16000	8.643	8.615	10.763	-1.385	12.148	0.107	-0.787
15000	8.717	8.617	11.047	-1.217	12.264	0.136	-0.762
14000	8.817	8.619	11.351	-1.036	12.387	0.160	-0.743
13000	8.929	8.620	11.676	-0.832	12.508	0.180	-0.727
12000	9.039	8.622	12.028	-0.639	12.667	0.199	-0.708
11000	9.148	8.623	12.410	-0.491	12.901	0.216	-0.688
10000	9.255	8.625	12.829	-0.394	13.223	0.228	-0.684

Table 3.8: Observing log for imaging data presented herein

Date (UT)	Instrument	Cluster	Field	RA (J2000)	Dec (J2000)	Filter	Exposure (s)
2001 Sept 21	PFCam	NGC 7063	P1	21:24:30	+36:30	U	$1, 30, 3 \times 300$
						BV	$1, 30, 4 \times 120$
2001 Sept 22	PFCam	NGC 2168	P1	6:08:46	+24:16	U	$1, 30, 3 \times 300$
						BV	$1, 30, 3 \times 120$
			P2	6:09:23	+24:24	U	$1, 30, 3 \times 300$
						BV	$1, 30, 3 \times 120$
2002 July 6	Nickel	NGC 6633	N1	18:26:54	+06:24	U	$1, 5, 30, 120$
						BVI	$1, 5, 30$
			N2	18:27:13	+06:32	U	$1, 5, 30, 120$
						BVI	$1, 5, 30$
		NGC 7063	N1	21:24:31	+36:31	U	$1, 5, 30, 120$
						BVI	$1, 5, 30$
			N2	21:10:99	+36:25	U	$1, 5, 30, 120$
						BVI	$1, 5, 30$
2002 July 7	Nickel	NGC 7063	N3	21:24:42	+36:27	U	$5, 30, 120$
						BVI	$1, 5, 30$
2002 July 8	Nickel	NGC 6633	N3	18:27:36	+06:35	U	$1, 5, 30, 120$
						BVI	$1, 5, 30$
			N4	18:26:47	+06:32	U	$5, 30, 120$
						BVI	$1, 5, 30$
			N5	18:28:06	+06:37	U	$5, 30, 120$
						BVI	$1, 5, 30$

[a] PFCam = Lick Observatory Prime Focus Camera; Nickel = Lick Observatory Nickel Camera; CFHT = CFHT CFH12K Mosaic Camera Archive

Table 3.8: (cont.)

Date (UT)	Instrument	Cluster	Field	RA (J2000)	Dec (J2000)	Filter	Exposure (s)
2002 Sept 7	PFCam	NGC 7063	P1	21:24:30	+36:30	U	$5, 30, 180, 3 \times 600$
						B	$5, 30, 3 \times 240$
						V	$5, 30, 3 \times 180$
1999 Oct 16	CFHT	NGC 6633	C1	18:27:44	+06:34	BV	$10, 50, 300$
		NGC 1039	C1	2:42:01	+42:47	BV	$10, 50, 300$
1999 Oct 17	CFHT	IC 4665	C1	17:46:15	+05:43	BV	$10, 50, 300$

[a] PFCam = Lick Observatory Prime Focus Camera; Nickel = Lick Observatory Nickel Camera; CFHT = CFHT CFH12K Mosaic Camera Archive

Table 3.9: Adopted calibrations for photometry.

Instrument	Date (UT)	Filter	Zero Point	Color Term	Airmass Term	Time
Nickel	2002 Jul 6	U	3.820 ± 0.091	-0.0608 ± 0.0019	0.4192 ± 0.0687	0.0043 ± 0.0117
		B	2.2479 ± 0.0034	-0.0834 ± 0.0019	0.2227 ± 0.0077	$\cdots$
		V	1.9858 ± 0.0050	0.0597 ± 0.0011	0.1360 ± 0.0050	$\cdots$
	2002 Jul 7	U	4.6368 ± 0.0514	-0.0608 ± 0.0019	0.6424 ± 0.0648	-0.0375 ± 0.0053
		B	2.6196 ± 0.0158	-0.0834 ± 0.0019	0.1557 ± 0.0377	$\cdots$
		V	2.3507 ± 0.0094	0.0597 ± 0.0011	0.0703 ± 0.0637	$\cdots$
	2002 Jul 8	U	4.1986 ± 0.0091	-0.0608 ± 0.0019	0.5112 ± 0.0122	0.0055 ± 0.0012
		B	2.5725 ± 0.0024	-0.0834 ± 0.0019	0.2481 ± 0.0082	$\cdots$
		V	2.3296 ± 0.0024	0.0597 ± 0.0011	0.1453 ± 0.0076	$\cdots$
PFCam	all	U	$\cdots$ [a]	0.0954 ± 0.0085	$\cdots$	$\cdots$
		B	$\cdots$ [a]	-0.0926 ± 0.0052	$\cdots$	$\cdots$
		V	$\cdots$ [a]	0.0791 ± 0.0047	$\cdots$	$\cdots$
CFH21K	all	B	$\cdots$ [a]	0.057 [b]	$\cdots$	$\cdots$
		V	$\cdots$ [a]	-0.0248 ± 0.0290	$\cdots$	$\cdots$

[a] Due to the use of local calibrators, zero points vary from frame to frame.

[b] Taken from CFH12K web site, `http://www.cfht.hawaii.edu/Instruments/Imaging/CFH12K/`

Table 3.10: White dwarf candidates in NGC 1039 (M34)

Candidate	Other ID	RA(2000)	Dec(2000)	V	$B-V$	$U-B$
WB 2	LB 3569	2:41:05.9	42:48:14.4	18.97[a]	0.90[a]	-0.38[a]
WB 3	...	2:43:00.0	42:48:13.5	... [b]	... [b]	... [b]

[a] From Anthony-Twarog (1981)

[b] Currently only uncalibrated photometry available

Table 3.11: White dwarf candidates in NGC 2168

Candidate	Other ID	RA(2000)	Dec(2000)	V	δV	$B-V$	$\delta(B-V)$	$U-B$	$\delta(U-B)$
WB 1	RA 2168-1	6:08:38.8	+24:15:06	20.924	0.047	0.029	0.067	-0.853	0.069
WB 2	···	6:08:42.4	+24:10:15	21.527	0.058	0.253	0.107	-0.973	0.115
WB 3	···	6:09:04.9	+24:21:38	20.561	0.098	0.042	0.132	-0.922	0.102
WB 4	RA 2168-2	6:09:05.8	+24:12:11	20.950	0.059	0.268	0.077	-0.665	0.071

Table 3.12: White dwarf candidates in IC 4665

Candidate	RA(2000)	Dec(2000)	V	δV	$B-V$	$\delta(B-V)$
WB 1	17:46:21.4	+05:44:30.0	18.203	0.134	0.112	0.147
WB 3	17:47:05.6	+05:45:51.3	19.517	0.020	0.310	0.029
WB 4	17:47:35.7	+05:37:09.7	19.766	0.021	0.407	0.032
WB 6	17:45:25.8	+05:53:28.6	20.149	0.022	0.160	0.033
WB 14	17:46:38.2	+05:50:22.6	18.309	0.019	0.154	0.027
WB 15	17:47:08.5	+05:38:13.8	18.413	0.041	0.360	0.078
WB 16	17:46:30.1	+05:40:38.8	18.704	0.019	0.405	0.027
WB 17	17:46:48.3	+05:42:55.9	18.753	0.019	0.308	0.027
WB 18	17:46:52.5	+05:43:32.9	18.782	0.019	0.346	0.027
WB 19	17:47:41.0	+05:42:08.5	19.516	0.022	0.425	0.086
WB 20	17:47:03.3	+05:39:57.4	20.527	0.022	0.352	0.033
WB 21	17:47:02.3	+05:50:47.6	20.677	0.024	0.288	0.035
WB 22	17:46:58.3	+05:35:41.8	20.976	0.029	0.377	0.040
WB 23	17:45:55.8	+05:37:48.2	16.761	0.019	0.197	0.026
WB 24	17:45:39.6	+05:47:28.1	17.119	0.019	0.187	0.027
WB 25	17:45:13.4	+05:31:35.6	18.157	0.019	0.345	0.027
WB 26	17:45:46.4	+05:35:11.7	19.006	0.019	0.273	0.027
WB 27	17:45:31.0	+05:32:44.6	19.239	0.019	0.364	0.028
WB 28	17:46:08.8	+05:41:21.5	19.507	0.020	0.498	0.028
WB 29	17:45:14.8	+05:28:34.9	19.795	0.021	-0.039	0.030
WB 30	17:46:01.3	+05:52:42.2	19.772	0.021	0.492	0.031
WB 31	17:45:41.2	+05:45:09.7	19.920	0.043	0.233	0.064
WB 32	17:45:35.2	+05:39:25.6	20.716	0.025	-0.136	0.035
WB 33	17:45:11.8	+05:45:24.3	20.840	0.025	0.273	0.042
WB 34	17:46:05.9	+05:33:14.5	20.870	0.038	0.455	0.047
WB 35	17:45:06.0	+05:44:17.0	20.936	0.025	0.467	0.037

Table 3.13: White dwarf candidates in NGC 6633

Candidate	RA(2000)	Dec(2000)	V	δV	$B-V$	$\delta(B-V)$
WB 1	18:28:16.7	6:34:10.8	17.059	0.018	0.082	0.026
WB 2	18:27:13.6	6:19:54.5	17.144	0.019	0.124	0.026
WB 3	18:27:03.0	6:24:28.3	17.960	0.019	0.118	0.026
WB 4	18:27:10.4	6:26:15.7	18.816	0.019	0.159	0.027
WB 5	18:26:14.9	6:29:01.5	19.060	0.019	0.025	0.027
WB 6	18:27:43.7	6:32:57.1	19.069	0.019	0.384	0.027
WB 7	18:27:49.9	6:20:51.8	19.272	0.019	0.230	0.027
WB 8	18:27:23.4	6:19:49.8	19.744	0.019	0.231	0.027
WB 9	18:26:57.5	6:43:32.0	20.676	0.022	0.153	0.030
WB 10	18:26:52.4	6:27:29.3	20.699	0.024	0.282	0.034
WB 11	18:26:29.1	6:43:22.3	20.740	0.021	0.176	0.030
WB 12	18:28:49.9	6:26:12.0	20.787	0.021	0.365	0.030
WB 13	18:27:14.9	6:20:04.1	21.072	0.023	0.139	0.031
WB 14	18:27:12.2	6:21:35.8	16.927	0.019	0.132	0.026
WB 15	18:26:08.1	6:24:51.0	19.626	0.020	0.115	0.028
WB 16	18:28:04.7	6:45:06.3	20.083	0.020	0.139	0.029
WB 17	18:28:03.0	6:41:27.3	20.267	0.124	0.535	0.142
WB 18	18:28:03.1	6:23:19.4	20.481	0.020	0.508	0.029
WB 19	18:27:35.5	6:38:11.5	20.550	0.021	0.548	0.030
WB 20	18:26:56.4	6:39:05.3	20.855	0.229	0.615	0.233
WB 21	18:27:49.0	6:45:27.8	21.016	0.025	0.414	0.036
WB 22	18:27:07.8	6:42:29.7	21.041	0.024	0.634	0.036
WB 23	18:26:17.5	6:22:32.5	18.768	0.019	0.163	0.027
WB 24	18:27:36.7	6:26:42.7	19.020	0.040	0.159	0.059
WB 25	18:26:13.6	6:31:05.5	19.934	0.020	0.269	0.029
WB 26	18:27:17.4	6:22:55.9	20.086	0.020	0.496	0.029
WB 27	18:27:12.3	6:21:02.1	20.084	0.021	0.293	0.029
WB 28	18:27:22.2	6:36:26.0	20.308	0.020	0.555	0.029
WB 29	18:27:52.6	6:32:55.0	20.522	0.022	0.435	0.031
WB 30	18:27:30.3	6:24:59.7	20.782	0.021	0.507	0.030
WB 31	18:26:21.6	6:45:48.0	20.934	0.122	0.394	0.129
WB 32	18:26:16.0	6:22:58.6	21.066	0.025	0.468	0.036

Table 3.14: White dwarf candidates in NGC 7063

Candidate	RA(2000)	Dec(2000)	V	δV	$B-V$	$\delta(B-V)$	$U-B$	$\delta(U-B)$
WB 1	21:24:10.3	+36:26:02.2	20.083	0.038	0.241	0.062	-0.342	0.068
WB 2	21:24:21.5	+36:26:00.7	19.204	0.031	0.152	0.052	-0.476	0.058
WB 3	21:24:07.3	+36:24:45.6	20.887	0.057	0.146	0.099	-0.524	0.114
WB 4	21:24:32.9	+36:27:51.5	21.142	0.042	0.411	0.075	-0.454	0.092
WB 5	21:24:43.6	+36:28:05.6	22.727	0.128	0.430	0.228	-0.369	0.276
WB 6	21:24:49.4	+36:33:16.4	21.969	0.136	0.422	0.242	-0.395	0.261
WB 12	21:24:33.5	+36:30:33.5	22.494	0.135	0.390	0.243	-0.597	0.279
WB 16	21:24:50.4	+36:34:08.2	21.067	0.052	0.484	0.091	-0.736	0.010
WB 18	21:24:20.7	+36:35:32.0	20.063	0.055	0.272	0.095	-0.459	0.110

Figure 3.1: $B-V$, V CMD for photometric models of WD cooling curves. Bergeron et al. (1995) model (blue dashed line) is for $\log g$=8.0. Red lines indicate cooling curves for current work (W95 models with Koester atmospheres), with masses $0.4M_{\odot}$($0.1M_{\odot}$)$1.0M_{\odot}$(top to bottom). Points on Bergeron et al. (!995) model and alternating present cooling curves indicate temperatures of (left to right) 50, 40, 30, 20, 16, 14, 12, 10 10^3K

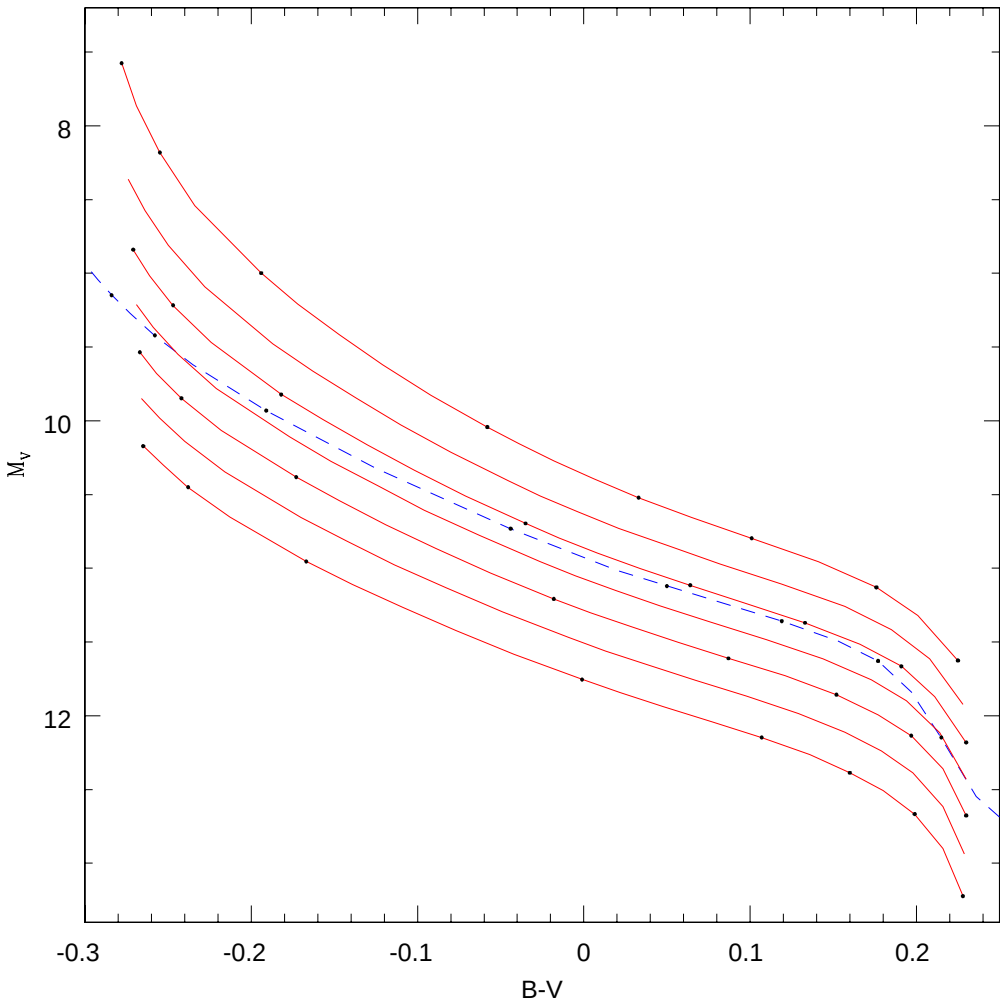

Figure 3.2: $B-V, U-B$ color-color plot for photometric models of WD cooling curves. Bergeron et al. (1995) model (blue dashed line) is for $\log g$=8.0. Red lines indicate cooling curves for current work (W95 models with Koester atmospheres), with masses $0.4M_{\odot}(0.1M_{\odot})1.0M_{\odot}$(bottom to top). Points on Bergeron et al. (!995) model and alternating present cooling curves indicate temperatures of (left to right) 50, 40, 30, 20, 16, 14, 12, 10 10^3K

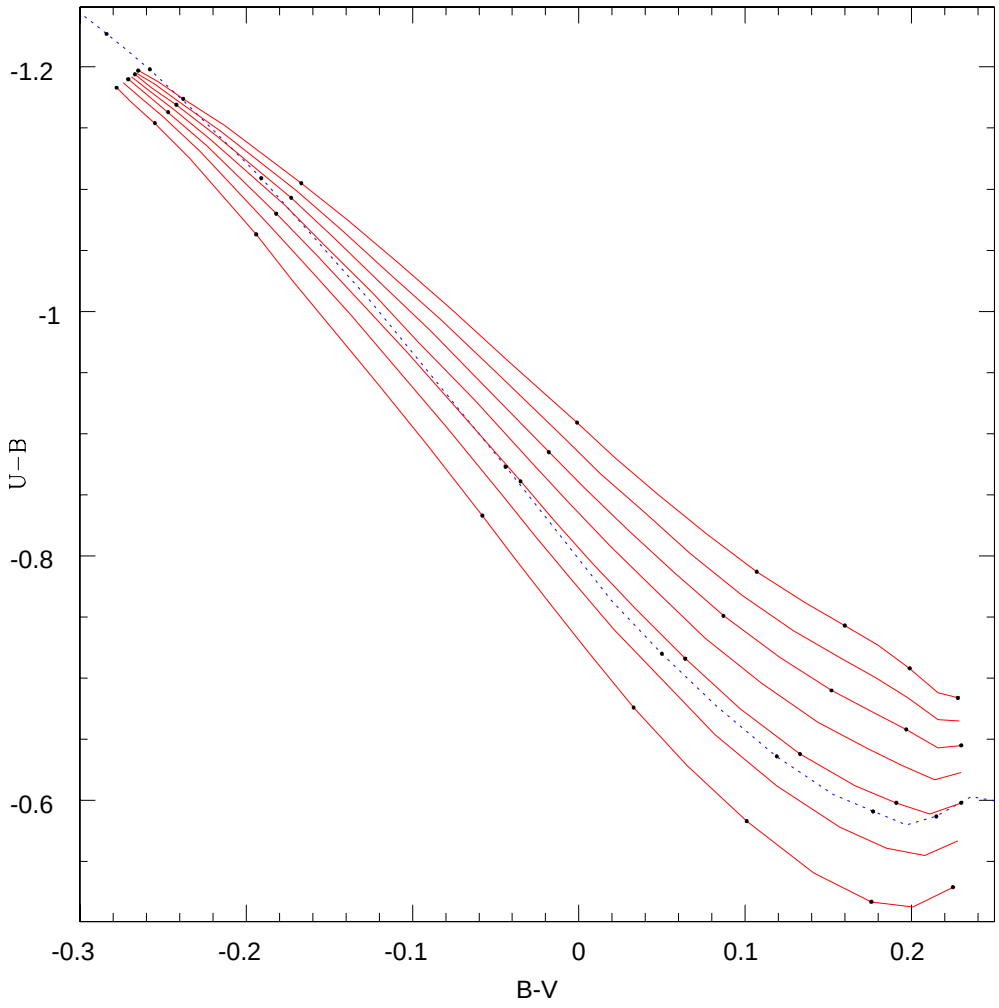

Figure 3.3: Digitized sky survey image of NGC 1039 (M34). CFHT image field-of-view is indicated by the green box.

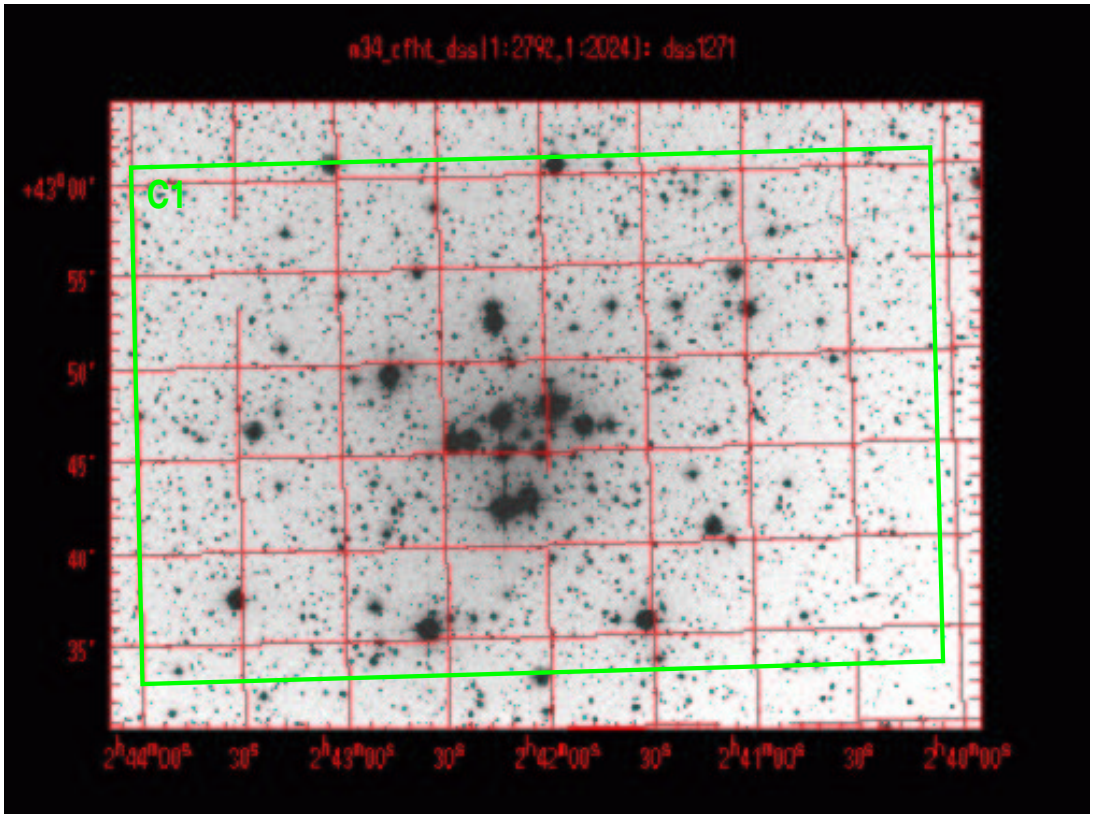

Figure 3.4: Digitized sky survey image of NGC 2168, with reduced PFCam fields indicated by yellow boxes.

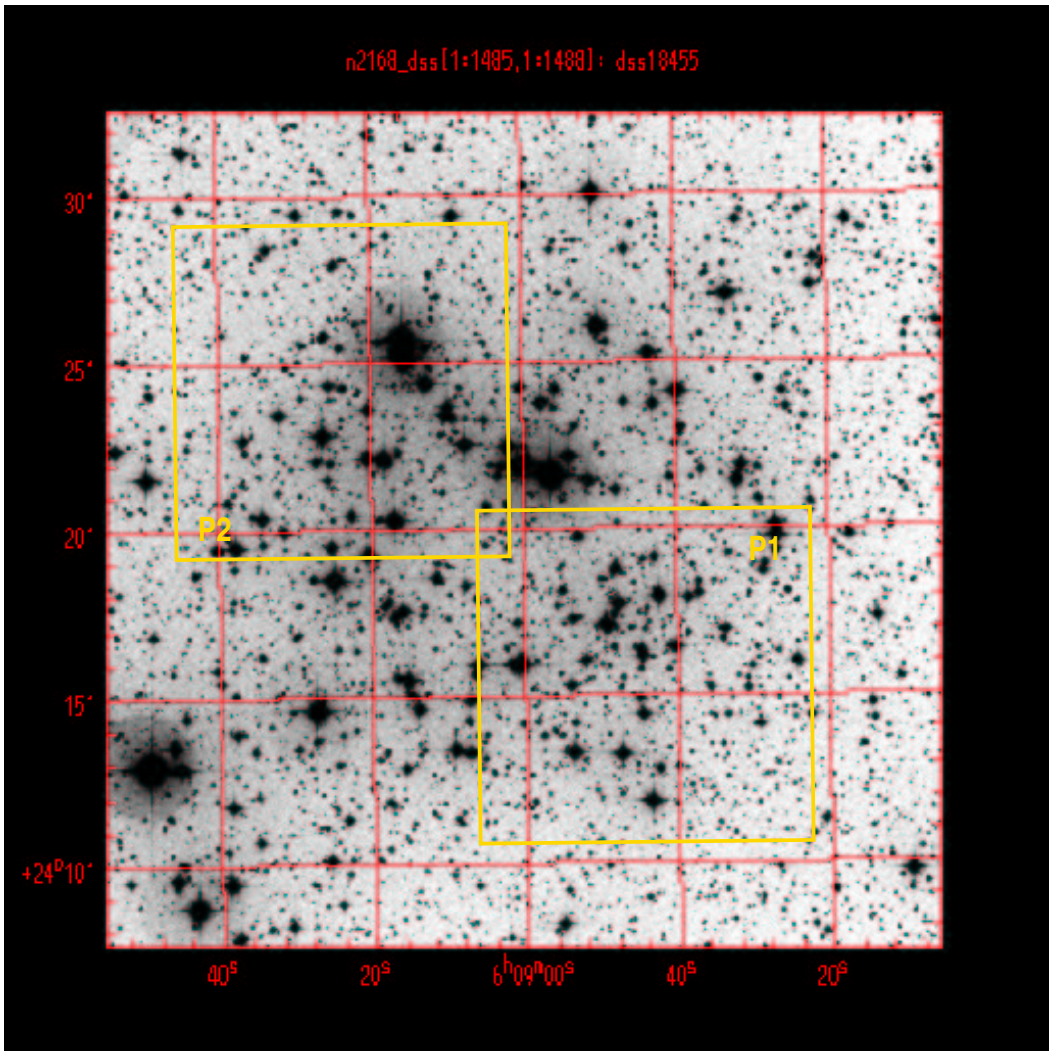

Figure 3.5: Digitized sky survey image of IC 4665, with CFHT field indicated by green box.

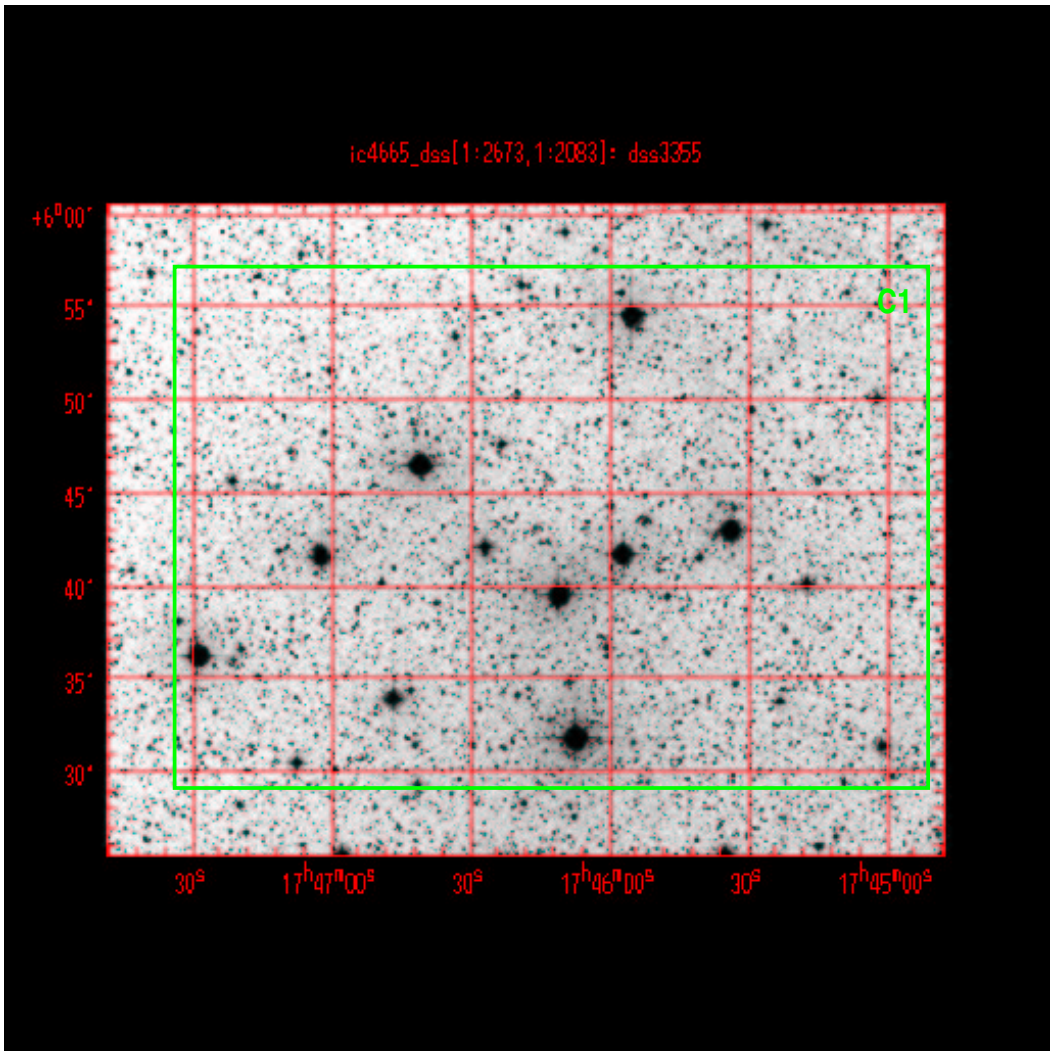

Figure 3.6: Digitized sky survey image of NGC 6633, with CFHT field indicated by the red box, and Nickel fields indicated by blue boxes.

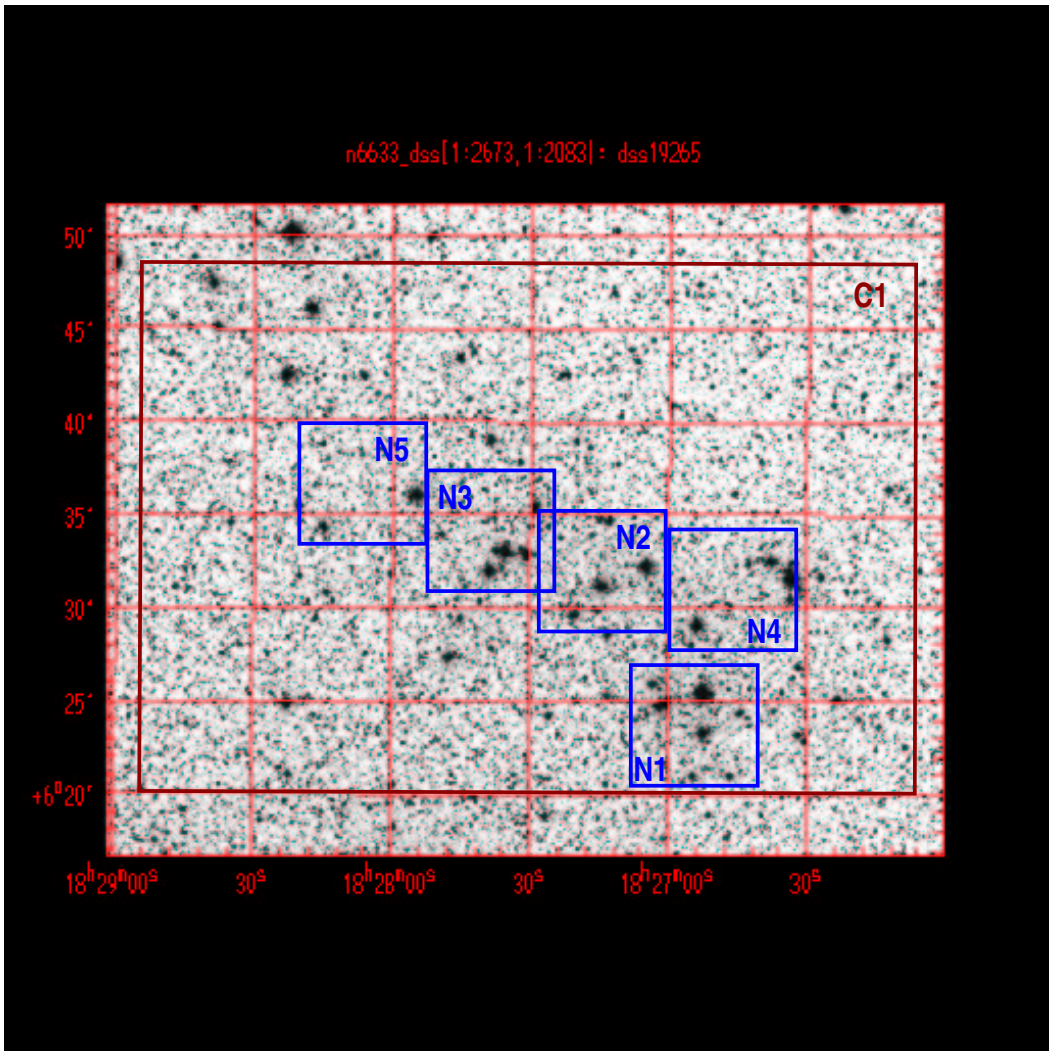

Figure 3.7: Digitized sky survey image of NGC 7063, with PFCam field indicated by the yellow box and Nickel fields indicated by blue boxes.

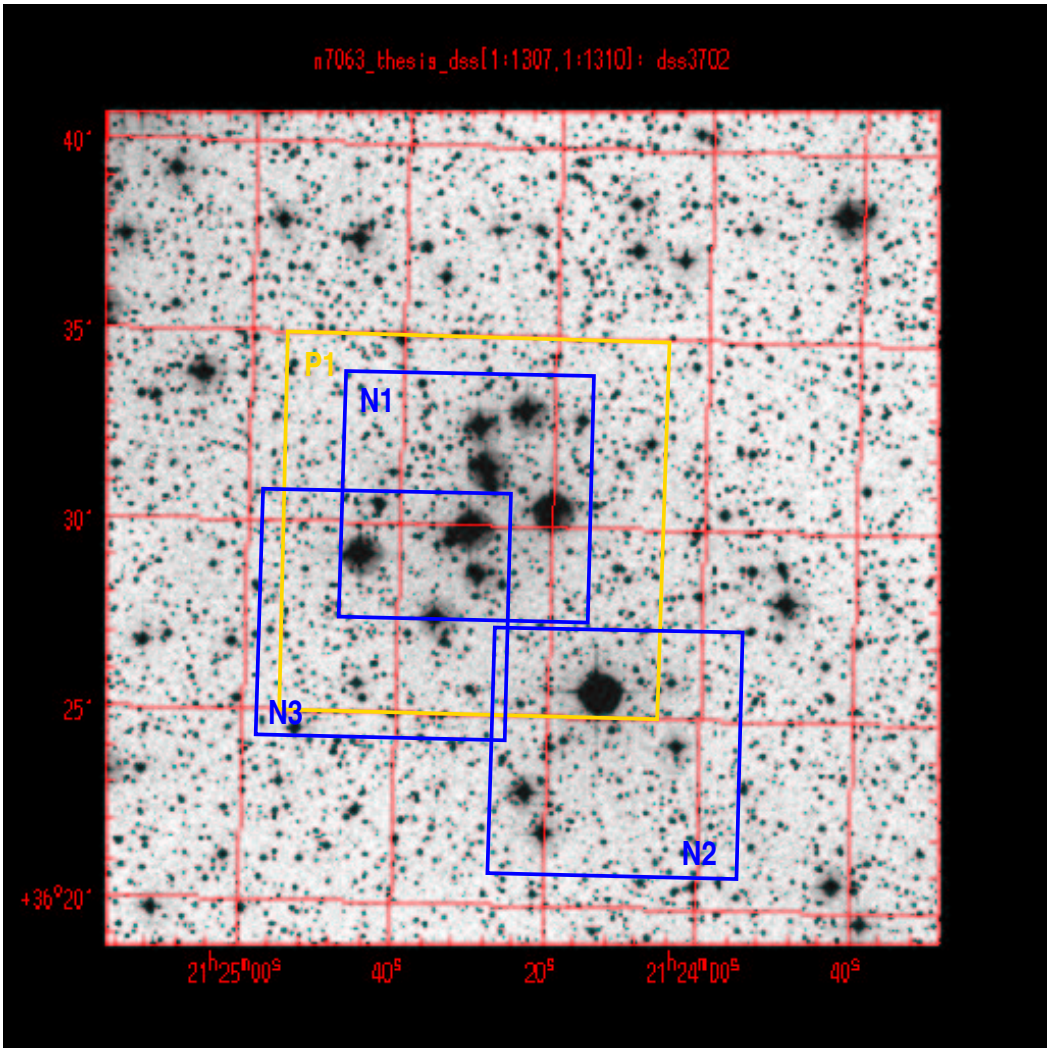

Figure 3.8: Color composite image of NGC 2168 created from PFCam UBV images. The logarithmic stretches were adjusted to produce aesthetically pleasing results.

Figure 3.9: Color composite image of NGC 7063 created from PFCam UBV images. The logarithmic stretches were adjusted to produce aesthetically pleasing results.

Figure 3.10: Evidence of non-linearity in the PFCam CCD response in Sept. 2001. Plot compares the instrumental B-band magnitudes of stars in NGC 7063 for 30s and 120s images. The 120s magnitudes have been offset by a 1.442 mag zero-point shift. Other filters and clusters show this same effect except for NGC 2168.

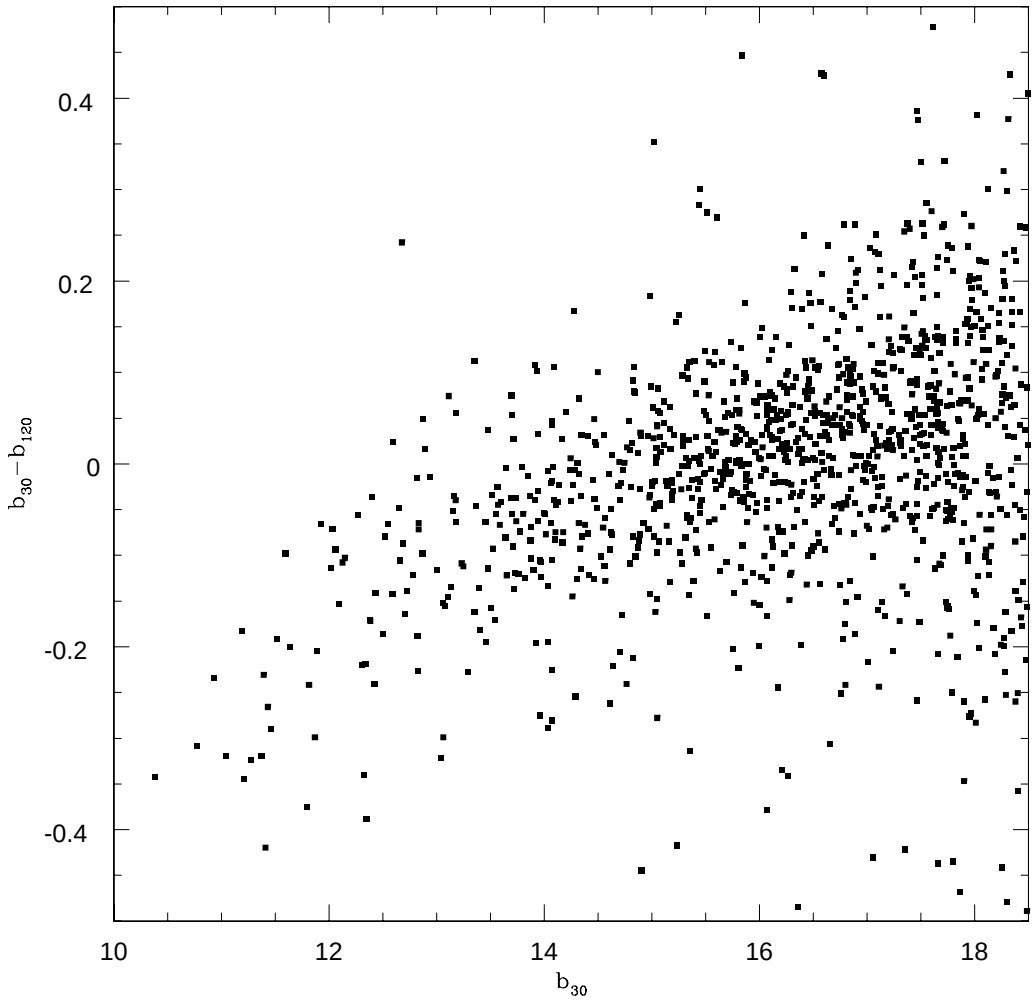

Figure 3.11: CMDs of the upper main sequence of NGC 2168. Points are from PFCam photometry. Lines indicate isochrones for $Z = 0.008$, age=8.0 (solid); $Z = 0.008$, age=8.3 (dotted); and $Z = 0.019$, age=8.0 (dashed). All isochrones are for $(m - M)_0 = 9.5$ and $E(B - V) = 0.255$.

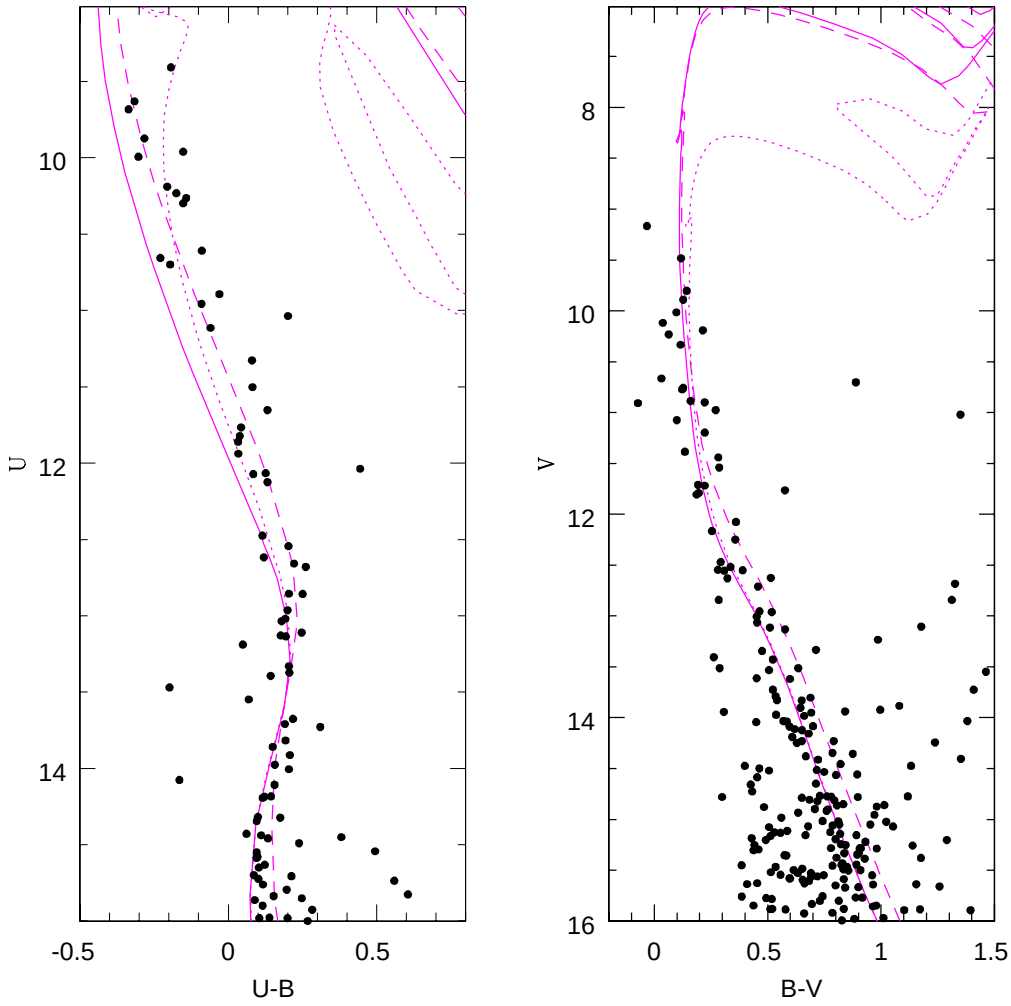

Figure 3.12: $V, B-V$ CMD of the upper main sequence of IC 4665. Data are from Prosser (1993), and isochrones are solar-metallicity of logarithmic ages 7.5 (dashed), 7.65 (solid), and 7.8 (dotted).

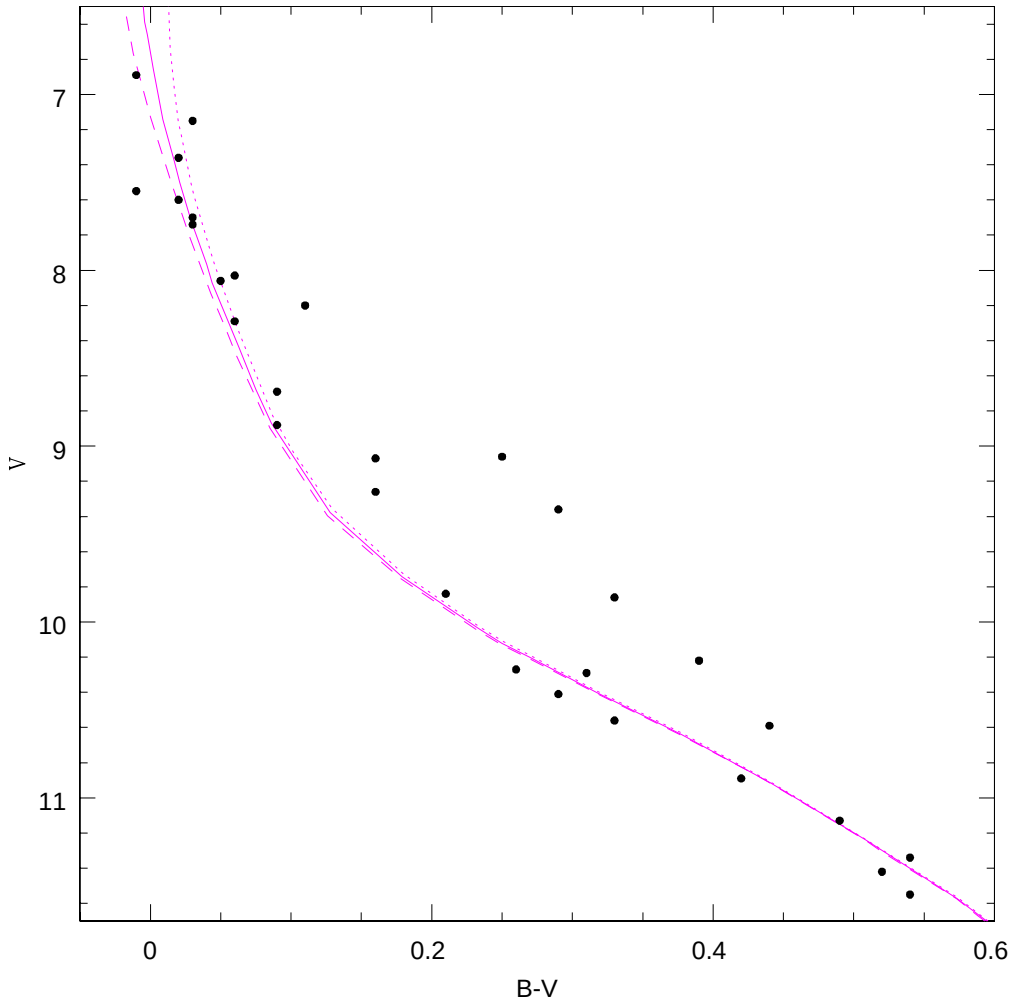

Figure 3.13: $V, B-V$ CMD of the upper main sequence of NGC 6633. Points indicate stars measured from Nickel and CFHT data; green filled points indicate proper motion members ($P \geq 70\%$) from Sanders (1973). Green stars indicate stars without Nickel or CFHT photometry; photometry for these points is from Sanders (1973). Magenta lines indicate isochrones for solar-metallicity clusters with logarithmic ages of 8.7 (solid), 8.65 (dotted), and 8.6 (dashed).

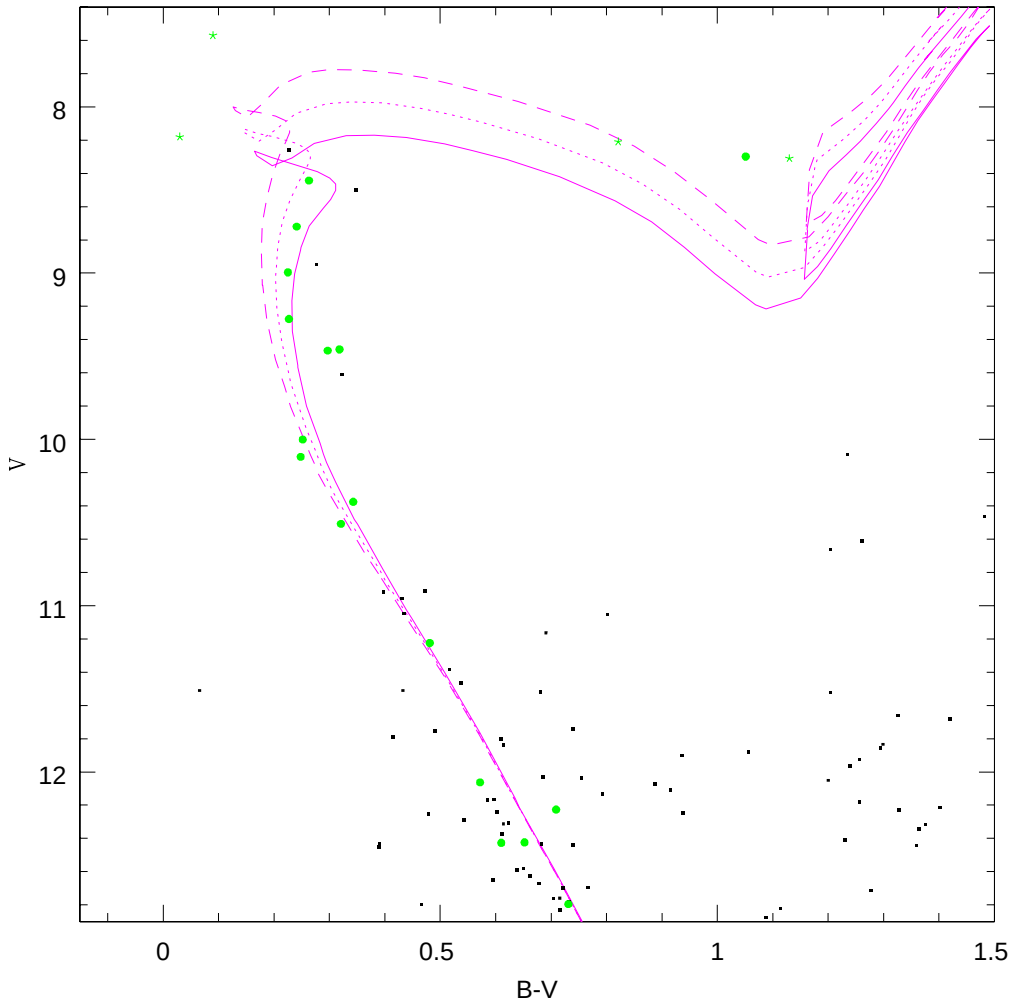

Figure 3.14: CMDs of the upper main sequence of NGC 7063. Points indicate stars measured from Nickel and PFCam data; green filled points indicate proper motion members ($P \geq 70\%$). The open green circle indicates a proper-motion member outside the PFCam and Nickel fields, HD 203921 (Hoag et al., 1961). Magenta lines indicate isochrones for solar-metallicity clusters with logarithmic ages of 8.0 (solid) and 8.15 (dotted).

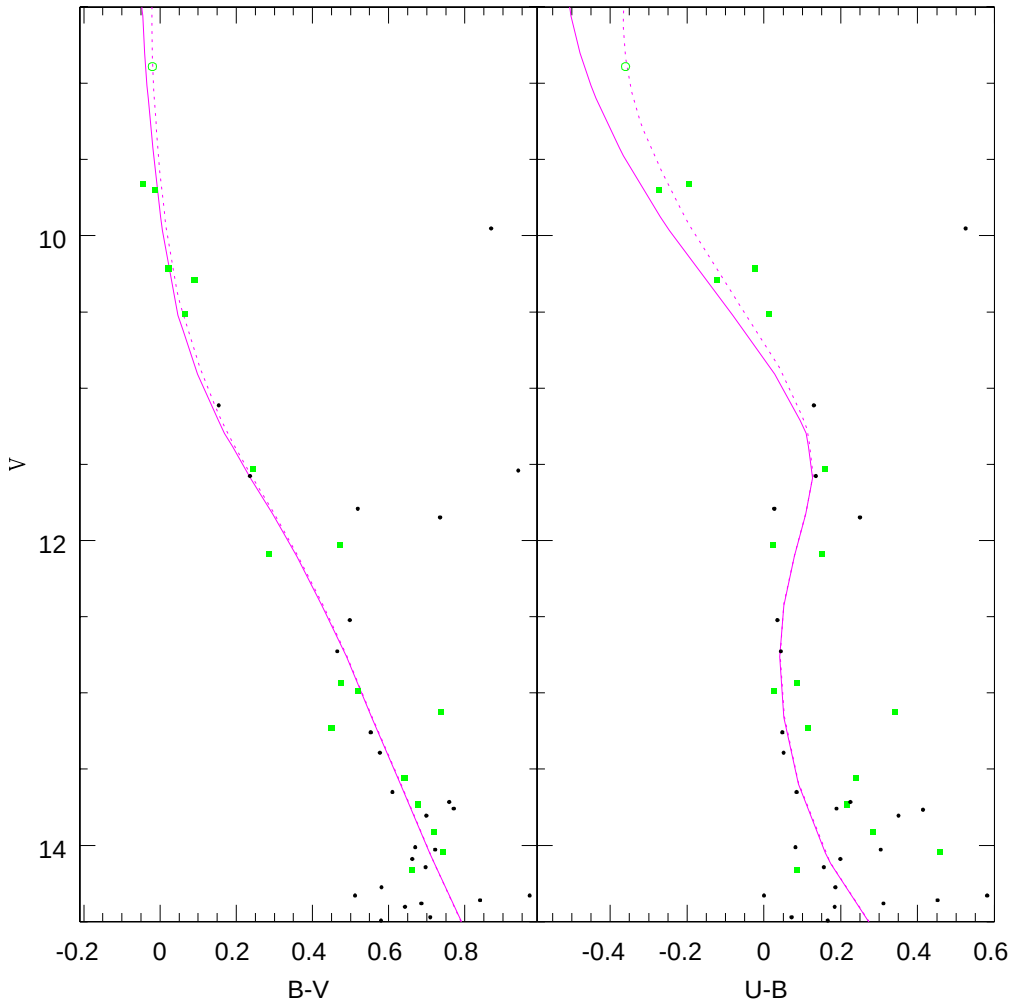

Figure 3.15: Color magnitude diagrams for NGC 2168. The magenta line indicates the Z=0.008 for $(m - M)_0 = 9.50$, $E(B - V) = 0.255$, and a logarithmic age of 8.0. Solid blue curves are cooling sequences for cluster WDs of masses $0.4M_\odot$, $0.7M_\odot$, and $1.0M_\odot$ (top to bottom). Dashed blue lines indicate WD cooling ages of 7.0(0.3)8.5. Solid black lines indicate WD cooling ages of 8.0 and 8.3, corresponding with two published values of the cluster age. Cyan points indicate color-selected WD candidates; error bars are 1σ photometric errors. Dashed lines indicate the selection criteria for WDs. Non-candidate objects within a selection region do not fulfill the criteria in other colors.

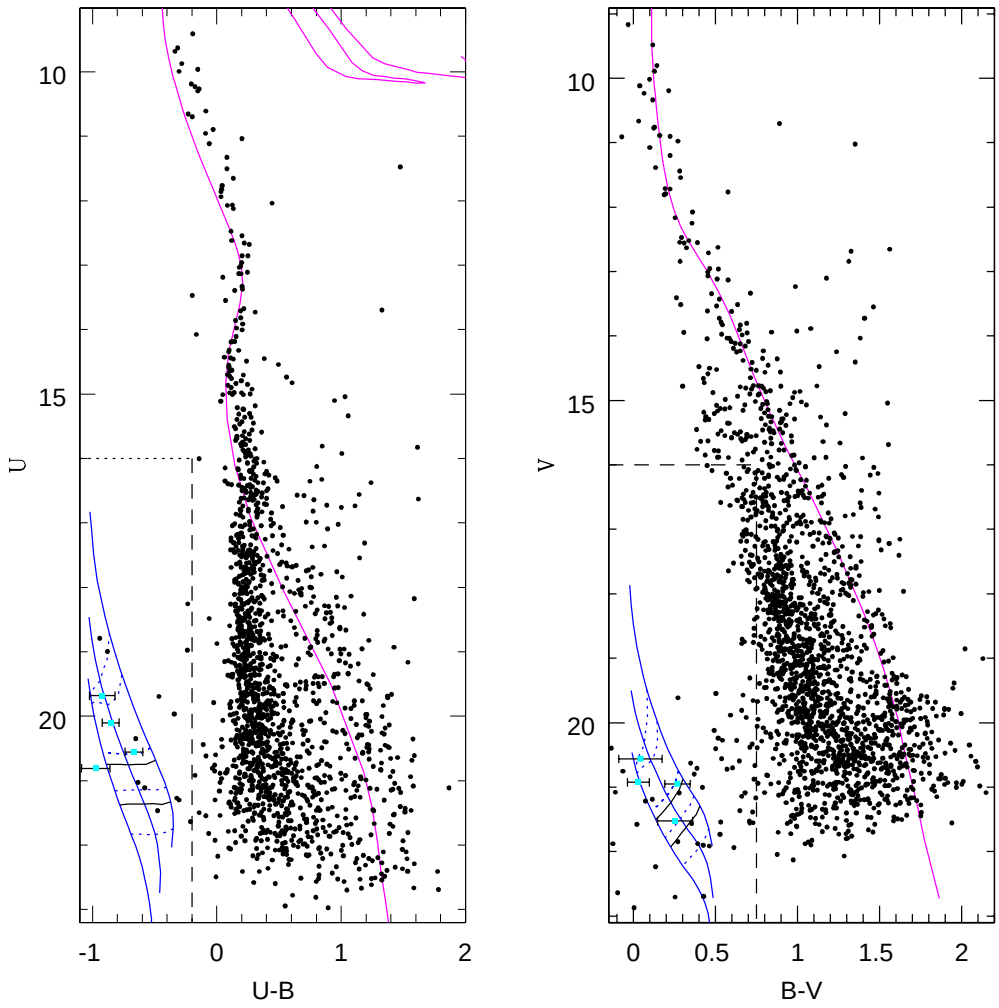

Figure 3.16: $B-V, U-B$ color-color diagram for NGC 2168. Objects are as indicated in previous figure, except WD cooling curves are for $0.4M_{\odot}$, $0.7M_{\odot}$, $1.0M_{\odot}$ *bottom to top*. The solid red line indicates the reddening vector.

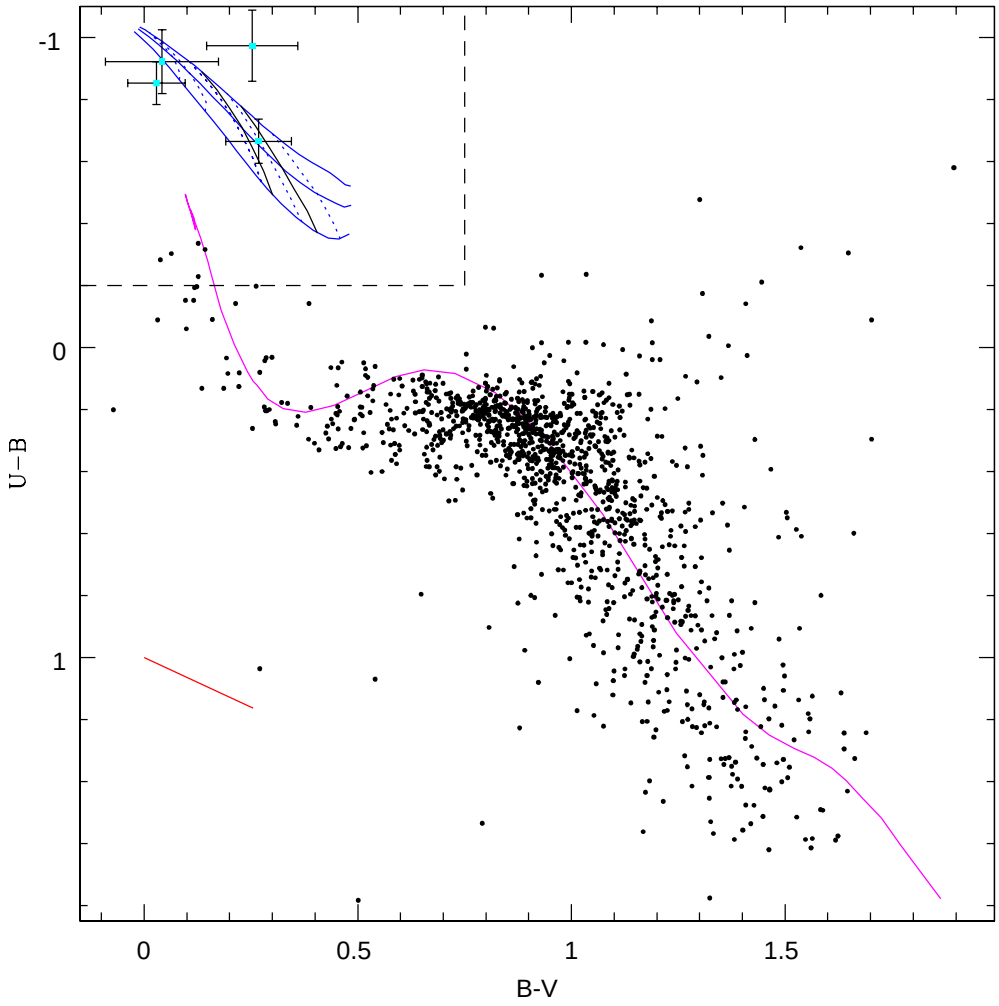

Figure 3.17: $B-V, V$ CMD for IC 4665. Magenta line is an isochrone for solar-metallicity with a logarithmic age of 7.8, $(m-M)_0 = 7.73$ and $E(B-V) = 0.174$. Blue lines are WD cooling curves for $0.4M_\odot$, $0.7M_\odot$, and $1.0M_\odot$ (top to bottom). The dotted blue lines indicate logarithmic WD cooling ages of 7.0(0.3)8.5, and the solid black line indicates a WD cooling age of 7.8. The dashed black line indicates selection criteria, and cyan points indicate the WD candidates. Open points on the upper-main sequence are photometry from Prosser (1993). The numerous blue objects with $V \gtrsim 21$ are mostly spurious detections; these were manually removed for brighter magnitudes.

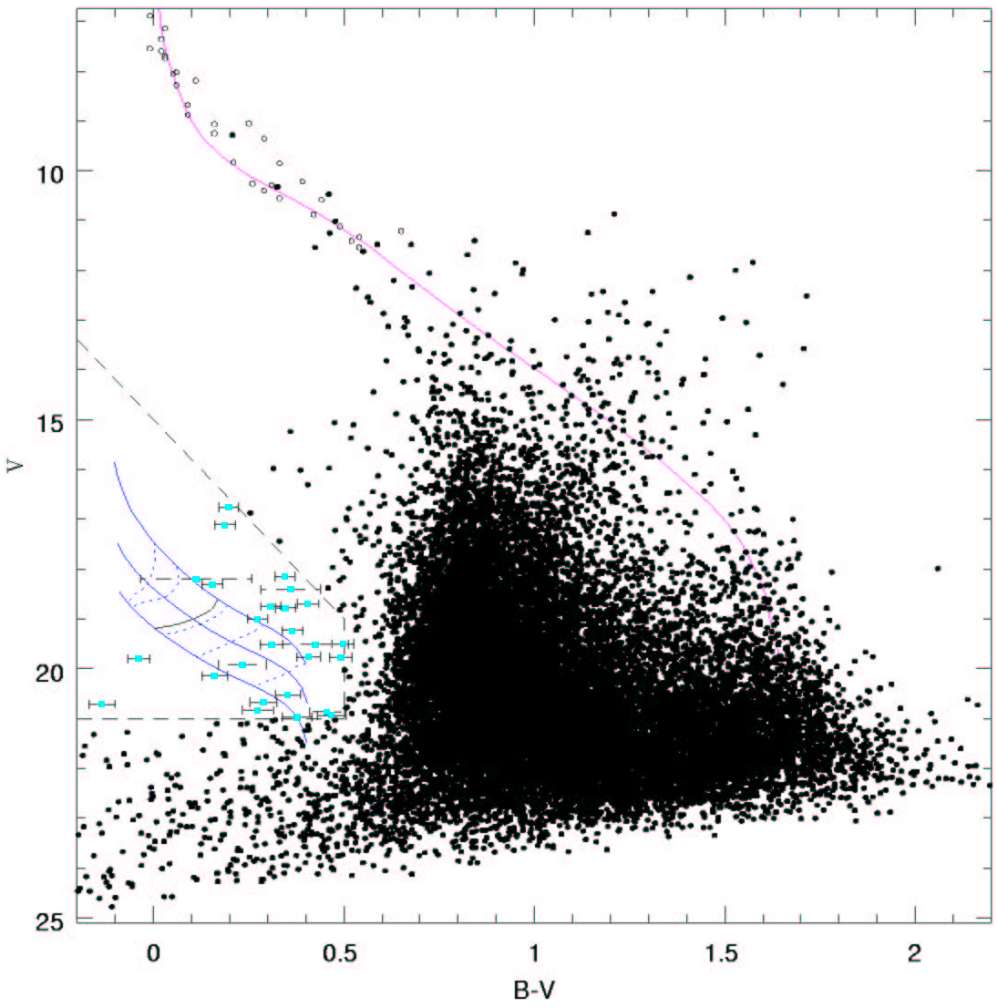

Figure 3.18: $B-V, V$ CMD for NGC 6633. Magenta line is isochrone for solar-metallicity isochrone with $(m-M)_0 = 8.01$, $E(B-V) = 0.172$ and a logarithmic age of 8.7. Blue lines are WD cooling models for $0.4M_\odot$, $0.7M_\odot$, and $1.0M_\odot$ (top to bottom). The dotted blue lines indicate logarithmic WD cooling ages of 7.0(0.3)8.5, and the solid black line indicates a WD cooling age of 8.7. The dashed black line indicates selection criteria, and cyan points indicate the WD candidates.

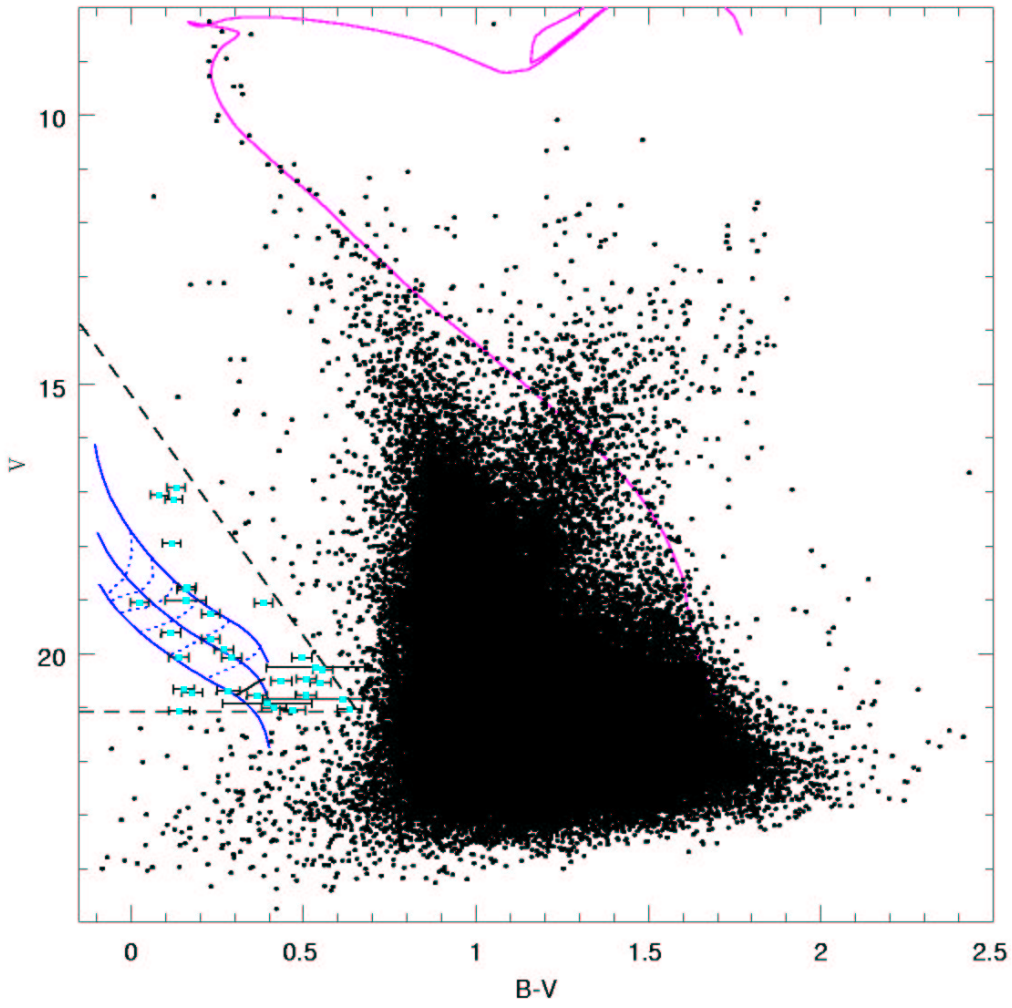

Figure 3.19: CMDs for NGC 7063. Magenta lines indicate isochrones for a solar-metallicity population with $(m-M)_0 = 9.191$, $E(B-V) = 0.091$, and a logarithmic age of 8.15. Blue lines are WD cooling models for $0.4M_\odot$, $0.7M_\odot$, and $1.0M_\odot$ (top to bottom). The dotted blue lines indicate logarithmic WD cooling ages of 7.0(0.3)8.5, and the solid black line indicates a WD cooling age of 8.2. The dashed black line indicates selection criteria, and cyan points indicate the WD candidates.

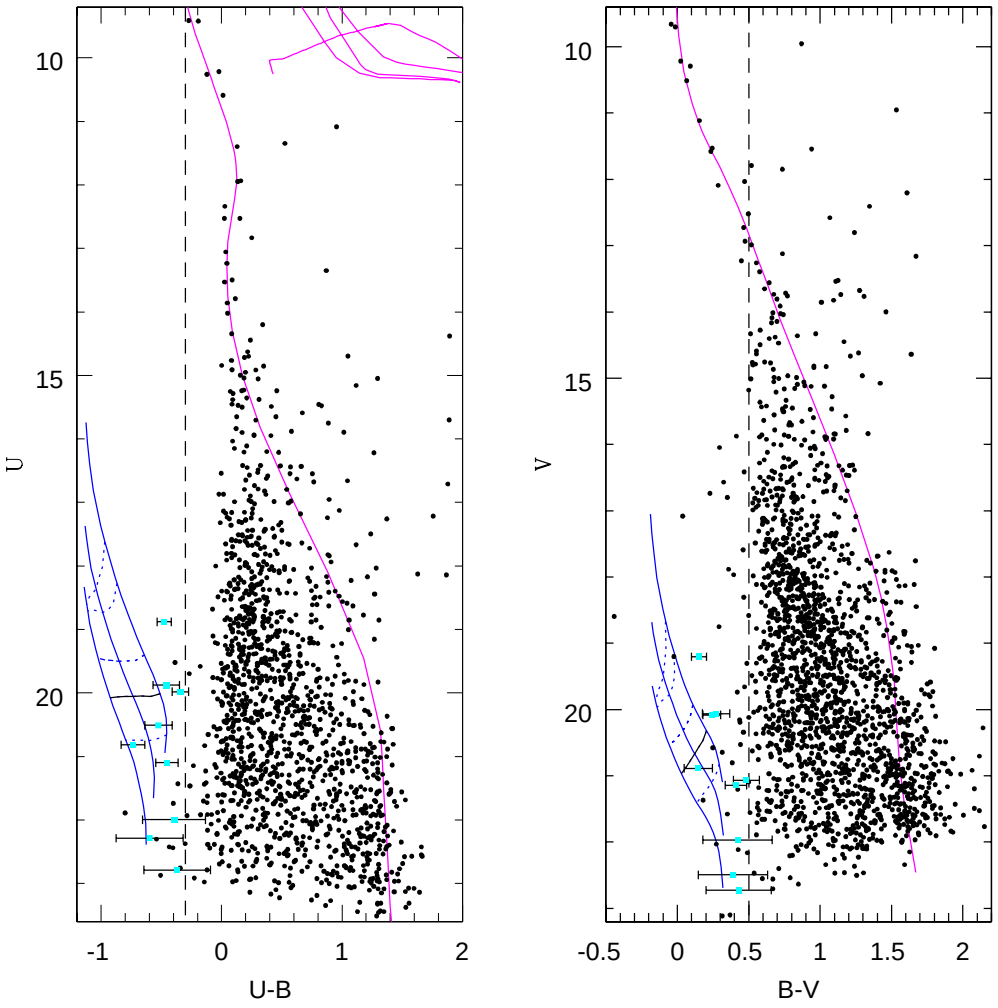

Figure 3.20: $B-V, U-B$ color-color diagram for NGC 7063. Symbols are as in previous plot, except solid blue lines are for $0.4M_{\odot}$, $0.7M_{\odot}$, and $1.0M_{\odot}$ *bottom to top*. Red line indicates reddening vector.

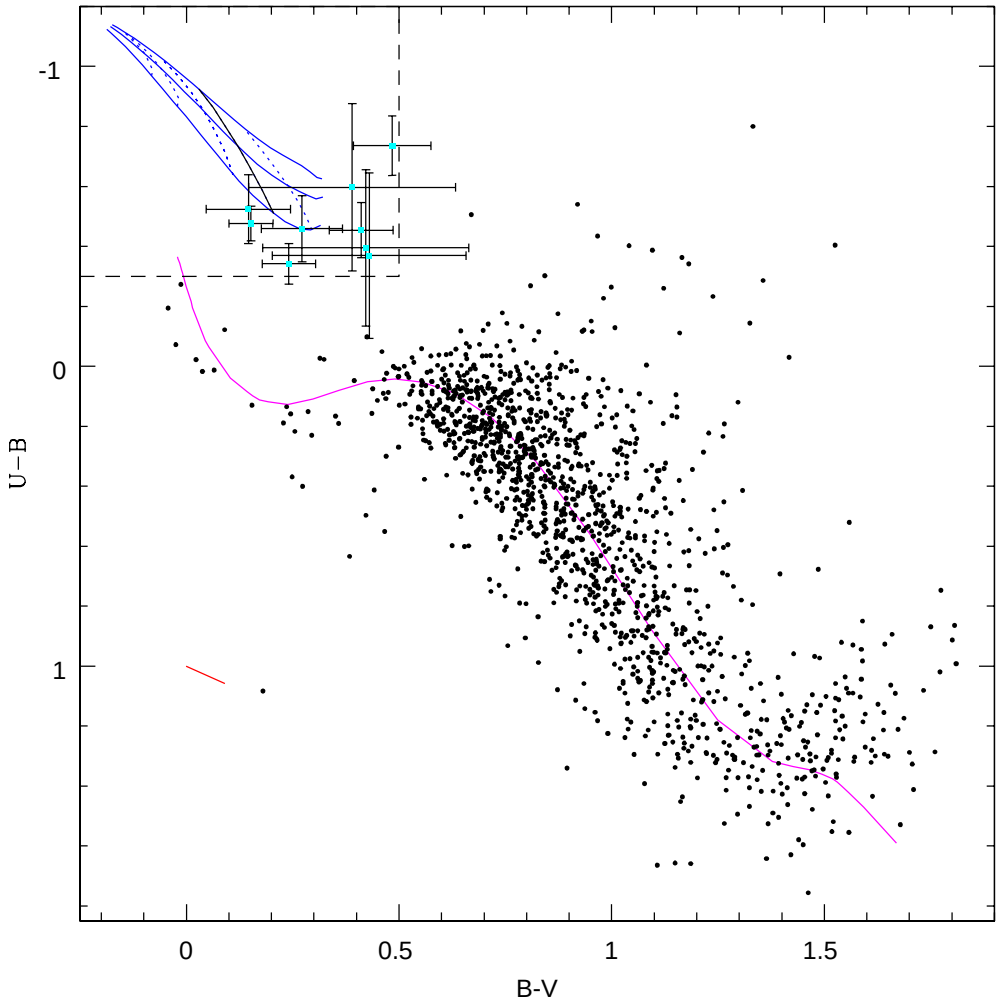

Chapter 4

Spectroscopy: Data and results

While broad-band imaging is useful for identifying potential white dwarfs, it is not able to identify white dwarfs unambiguously or to confirm cluster membership in the absence of a well-defined sequence, nor can broad-band imaging determine physical parameters such as $T_{\rm eff}$ or $\log g$ with high precision.

Estimates of $\log g$ and $T_{\rm eff}$ are possible using Strömgren photometry. These data are most reliable for $T_{\rm eff} \lesssim 15000\,{\rm K}$, and surface gravity estimates are unreliable for $T_{\rm eff} \gtrsim 20000\,{\rm K}$ due to the disappearance of the Balmer jump (Bergeron, Saffer & Liebert 1992, hereafter BSL). As the open cluster WD sample is likely to include hotter WDs, Strömgren photometry will not suffice for this project.

Spectroscopy of WD candidates permits unambiguous identification of white dwarfs. In addition, $T_{\rm eff}$ and $\log g$ can be determined from the absorption line profiles. A simultaneous fitting of the Balmer lines from synthetic spectra to the observed spectra results in very tight constraints on the surface gravity and effective temperature, a method pioneered by Bergeron et al. (1990) and used to analyze a large population of field WDs in BSL.

4.1 Observations and reductions

Spectra were taken during two observing runs, 2001 Aug 22-23 UT and 2002 Aug 7-8 UT using the blue side of the Low-Resolution Imaging Spectrometer (LRIS) on the Keck I telescope (Oke et al., 1995).

During the August 2001 run, the instrument was fitted with a SITe/Tektronix 2048×2048 UV/AR-coated CCD. Due to the extremely high readout noise of amplifier #2, a single-amp readout using only amplifier #1 was used. The 400 l mm^{-1} grism, blazed at 3400Å, was used along with the $1''$-wide longslit, resulting in a spectral resolution of 6Å and wavelength coverage from the dichroic limit (~ 5700Å) to

the blue atmospheric cutoff (~ 3000Å). The D560 dichroic was used as a beam splitter; red-side spectra were obtained but not analyzed. The weather was photometric, and seeing averaged $\sim 0''.6$ over both nights.

During this run, spectra were obtained for several WD candidates in IC 4665, NGC 6633, and M34. In addition, several spectra of bright field WDs were obtained for the purposes of comparison with previous analysis.

The blue side of LRIS was retrofitted prior to the August 2002 observing run. The SITe CCD was replaced with a 2-chip 2048×4096 Marconi CCD mosaic, resulting in higher throughput for short wavelengths. Two-amplifier readout was used for each chip; no binning was performed. As before, the 400 l mm^{-1}, 3400Å-blaze grism was used with the D560 dichroic. The weather was partly cloudy, with variably-thick cirrus clouds affecting observations both nights. Seeing was $\sim 0''.6$ on August 7 and $0''.7$ on August 8.

Observations in August 2002 were made with both a $1''$ long slit and $1''$ slit masks, with resulting spectral resolution of 6Å. The candidate-WD coordinates had an accuracy of $\sim 0''.5$, so many slit-mask spectra suffer from vignetting. Additional problems with LRIS control software resulted in several images being read out but not recorded. In spite of this, the majority of candidate WDs in NGC 6633 and NGC 7063 were observed.

Data were reduced using standard methods in IRAF. Wavelength calibration was accomplished using HgCdZn arc lamps; the resulting calibrations have RMS deviations of 0.5Å. Night sky lines were used to shift the zero points of individual spectral wavelength scales as needed.

4.2 Balmer-line fitting technique

Balmer-line fitting of synthetic spectra to WD spectra is a precise technique because of the differing sensitivities of individual Balmer lines to $\log g$ and $T_{\rm eff}$. Figure 4.1 shows changes in theoretical line profiles with changes in these parameters. From the figure it can be seen that, for a given Balmer line, there are strong degeneracies in $T_{\rm eff}$ and $\log g$. The use of multiple Balmer lines lifts the degeneracy and permits the determination of $\log g$ and $T_{\rm eff}$.

The technique used to fit the lines is a modification of that used in BSL and Claver et al. (2001). A two-step process was used to normalize the line flux. Curvature in the spectrum was removed by fitting and dividing out a fourth-order Legendre polynomial. Next, the flux was set to unity at a fixed distance from the line center by fitting a linear function at these distances. The wavelength ranges used in each step are listed in Table 4.1. Constant offsets were added to the wavelength solutions as needed so that the line centers matched with the rest wavelength of each line. Model spectra were

convolved with a Gaussian profile to the instrumental resolution, and line flux was normalized in the same method.

The observed line profiles are compared to the Koester model spectra by calculation of χ^2. Each sampled point n in the observed spectrum contains the normalized spectral flux H_ν^{obs} averaged over the wavelength interval $(\frac{\lambda_n-\lambda_{n-1}}{2}, \frac{\lambda_{n+1}-\lambda_n}{2})$. The model flux was calculated by dividing this interval into ten sub-intervals. The normalized model flux was evaluated at the midpoint of each sub-interval i by a bicubic spline interpolation of the input model spectrum. The model flux averaged over the entire interval, $\bar{H}_\nu^{mod}(\lambda_n)$, is then

$$\bar{H}_\nu^{mod}(\lambda_n) = \frac{1}{10}\sum_{i=1}^{10} H_\nu^{mod}(\lambda_i)\,. \tag{4.1}$$

The χ^2 value is calculated independently for each Balmer line in each available model atmosphere using the standard formula:

$$\chi^2 = \sum_{i=1}^{N}\left(\frac{\bar{H}_\nu^{mod}(\lambda_i) - H_\nu^{obs}(\lambda_i)}{\sigma_i}\right), \tag{4.2}$$

where λ_i ranges from the low-wavelength to high-wavelength ends of the fit region.

The standard deviation σ_i is taken to be constant over each Balmer line fitting region and is the rms noise in the pseudo-continuum regions nearest the line. This value of σ is an underestimate of the true standard deviation, as the relative noise should increase in the line core.

The result is a grid of χ^2 values at each model $T_{\rm eff}$ and $\log g$. A two-dimensional interpolation is then used to determine the global minimum of χ^2. The $T_{\rm eff}$ interpolation is defined over the range 10000K$\leq T_{\rm eff} \leq$50000K at 200K intervals ($T_{\rm eff} \leq 30000$K) or 500K intervals ($T_{\rm eff} > 30000$K). The $\log g$ interpolation is defined over the range $7.00 \leq \log g \leq 9.00$ at 0.05 dex intervals.

Confidence intervals for each model atmosphere are determined as follows. Let $\Delta \equiv \chi^2 - \chi^2_{min}$, where χ^2 is the computed chi-square value for a given $T_{\rm eff}$ and $\log g$ model of a given Balmer line and χ^2_{min} is the global minimum χ^2 for the line. The probability that the true model has a $\chi^2 - \chi^2_{min} > \Delta$ is given by the incomplete gamma function

$$Q(\frac{\nu}{2}, \frac{\Delta}{2}, H_i) \equiv \frac{1}{\Gamma(\nu/2)}\int_{\Delta/2}^{\infty} e^{-t}t^{\nu/2-1}dt \tag{4.3}$$

where ν is the number of degrees of freedom (=2) (Press et al., 1992) and H_i is the Balmer transition. The level of confidence at each model grid point is then just the

product of the Q from the individual Balmer lines,

$$Q = \prod_{H_i=H\beta}^{H8} Q(\frac{\nu}{2}, \frac{\Delta}{2}, H_i) \tag{4.4}$$

These confidence contours are only strictly valid if two conditions are met. First, the measurement errors must be normally distributed, which is likely. Second, the models must have a linear dependence on $T_{\rm eff}$ and $\log g$ *or* the models must be able to be represented by a linearized model over the region containing the minimum and the uncertainties. This latter condition is not is not strictly true for the synthetic spectral models, although plots of model line fluxes show that over small regions ($\Delta T_{\rm eff} \sim 5000$K and $\Delta \log g \sim 0.75$) the flux variations are relatively linear in $T_{\rm eff}$ and $\log g$.

This method of determining the confidence contours differs from that of BSL, who use the Levenberg-Marquardt method to determine the χ^2 minimum and the covariance matrix, from which confidence intervals can be determined. Given the limited number of degrees of freedom and the relatively small number of models, it is not necessary to use the Levenberg-Marquardt method to determine χ^2_{min}, as the entire χ^2 space can be evaluated in a matter of minutes, even if the model resolution were to be greatly increased. The calculation of the covariance matrix resulting from the use of the method is the formally correct means of determining the errors on the fitted parameters, and will be used in future WD spectral analyses.

The usefulness of the simultaneous Balmer line fitting techniques is shown in Fig. 4.2, which shows confidence contours in $T_{\rm eff}$, $\log g$ space for the individual Balmer line fits and the combined fit for WD 0352+096. Figure 4.4 compares the best-fit spectral model for each Balmer line to the data.

Once $T_{\rm eff}$ and $\log g$ are known from the fitting, the mass and cooling age can be derived for each WD from the WD evolutionary models. These quantities were interpolated from the W95 models using a two-dimensional spline (Press et al., 1992). Grids of constant mass and cooling age are included for reference in Fig. 4.2.

4.2.1 Testing and comparison with previous results

Internal consistency checks on the Balmer-line fitting technique were performed by examining spectra from WDs with multiple observations. As none of the DA WDs were observed on multiple observing runs, these checks only probe the consistency within a given run. Fig. 4.3 shows results from two observations of NGC 6633 WB 12. The solutions from individual images are consistent with each other and the combined results, suggesting that the fitting technique gives consistent results and reasonable confidence limits.

The Balmer-line fitting technique was tested on several WDs with previously-determined values of $T_{\rm eff}$ and $\log g$. Table 4.2 indicates the object, measured $T_{\rm eff}$ and $\log g$, and the previously-published values. Parameters from BSL do not contain individual errors on atmospheric parameters, but the overall errors are stated to be $\langle \Delta T_{\rm eff} \rangle = 350$K and $\langle \Delta \log g \rangle = 0.049$. Errors quoted for this work indicate 90% confidence intervals; ellipses indicate that no 90% confidence interval was obtained.

From Table 4.2, it is apparent that the stated errors in published $T_{\rm eff}$ are often much smaller than the scatter, implying that systematic differences between the models dominate, and that these systematics have not been fully accounted for in the error budget. The surface gravities generally agree to within stated errors.

Table 4.3 gives the derived parameters of WD mass and cooling age for most of the WDs in Table 4.2. For comparison purposes, the masses of WDs in previous observations were re-derived from the W95 models and the previously-published $T_{\rm eff}$ and $\log g$. The derived masses generally agree to within stated errors, but cooling ages have scatter larger than the stated errors. This is due to the derived ages being highly sensitive to $T_{\rm eff}$ and the associated (understated) errors.

The current observations are of sufficient quality ($\frac{\rm S}{\rm N} \geq 150$ per resolution element) that systematic errors within the models prevent convergence upon a solution. An example of a systematic is shown in Fig. 4.4 as a consistent depression of the line flux in the red wings of the observed lines in comparison with the model profiles.

Another systematic issue arises at high temperatures, where the model grid spacing is large. In the cases of hot WDs, the correct model can be distant enough from all grid points that the χ^2 fits give no satisfactory solution, as illustrated in Fig. 4.5. For most of the program WDs, however, the observational errors are large enough and $T_{\rm eff}$ cool enough that these systematics are not large issues.

4.2.2 Cluster membership determination

While there are numerous methods for determining whether a star is a member of a given cluster, few of these methods work well with the WD sample. Proper motion studies are not deep enough to detect these candidates and confirm membership. The wavelength solution for the spectra are not accurate enough to permit radial velocity measurements. Photometry alone is insufficient, as the distance is degenerate with WD mass and temperature in photometric space.

Another possible technique is the use of interstellar Ca II K-line absorption. Although the low-resolution spectral observations do not permit observations of lines from individual clouds, the equivalent width of the interstellar K-line as measured in the spectra of member WDs will equal that seen in the spectra of cluster B stars. While initially a promising technique, the WD spectra obtained were not generally of

sufficient signal-to-noise to observe the interstellar K line.

The selected technique for determining membership combines spectroscopic results with the photometry. The mass and cooling age derived from a WD spectrum can be combined with the photometric calibrations of §3.1 to determine the absolute magnitude of the WD. The apparent distance modulus of the WD can then be derived and compared to the apparent distance modulus of the cluster. If the apparent distance modulii are in agreement, then the WD is a likely cluster member. If the distance modulii disagree, than the WD is either foreground or background. Fig. 4.6 shows an example of this technique.

4.2.3 Non-white dwarf identification

Non-WDs were generally identified based on a qualitative inspection of the spectra. The high surface gravity of WDs quenches the higher-order Balmer lines, so that lines higher than H9 are difficult to observe. Objects with lower surface gravities, such as early-type stars, field horizontal branch stars, and hot subdwarf stars, have these higher-order lines, making the presence of these lines a strong qualitative diagnostic for identification of a star as a WD.

Quantitatively, non-WDs with Balmer lines result in poor χ^2 fits in the Balmer-line fitting technique. The best-fitting models tend toward the lowest model atmosphere surface gravities, and fits from individual Balmer lines do not necessarily converge on a single $T_{\rm eff}$, as shown in Figs. 4.7-4.8. Therefore, we have high confidence that the spectral identifications are accurate.

4.3 Candidate white dwarf results

The results of the spectroscopy are summarized in Table 4.4. For each observed WD candidate, the identification is presented, and, if relevant, the observed and derived WD parameters are listed. Identifications of non-WDs are subject to uncertainty. Stars with narrow hydrogen and helium features were identified as hot subdwarfs on the basis that the distances to main sequence O and B stars of these magnitudes would be $\gtrsim 100$kpc. Stars with narrow Balmer lines were identified as field horizontal branch (FHB) stars if the breadth of Hδ at 20% below the continuum was less than 30Å (Beers et al., 1988). The major contaminants of the sample are, as expected, QSOs and hot field stars.

The resulting $T_{\rm eff}$ and $\log g$ measurements can then be used along with the W95 C/O WD models to determine the WD mass, cooling age, and distance modulus. For each detected DA WD, these derived quantites are given in Tab. 4.5. Results of individual clusters are discussed below.

NGC 1039. — Spectra are shown in Fig. 4.9. Both candidates are DA WDs, but the Balmer-line fitting did not converge for WB 3. Based on the results of Balmer-line fitting (Figs. 4.10 & 4.11), WB 2 is a cluster member.

IC 4665. — Spectra are shown in Fig. 4.9. Neither observed candidate was a white dwarf.

NGC 6633. — Numerous candidates were observed. DA WD spectra are shown in Fig. 4.12, and all other spectra are shown in Fig. 4.13. Individual Balmer-line fits are plotted for each observed DA WD in Figs. 4.14-4.27. Of DA WDs, only two are potential members – WB 8 and WB 27.

Two DB white dwarfs were detected, WB 14 and WB 16. WB 14 was previously analyzed by Reimers & Koester (1994), and is a foreground, cool ($T_{\rm eff} \sim 13000$K) WD. The $T_{\rm eff}$ and $\log g$ of WB 16 were estimated as in Koester, Schulz, & Wegner (1981) and are given in Tab. 4.4. Based on the helium-atmosphere cooling models presented in Bergeron et al. (1995b), the distance modulus of WB 16 is $(m-M)_V \approx 9.0$, about 0.5 mags more distant than NGC 6633. The other non-DA WD is WB 5, whose spectrum shows strong, broad He I λ4471 and He II λ4686. This object is therefore classified as a DO WD. Because DO WDs are hot and intrinsically bright ($M_V \lesssim 10$), this WD is in the background of NGC 6633.

NGC 7063. — The spectra obtained are displayed in Fig. 4.28. Five DA WDs were detected, though only one (WB 1) is a potential cluster member. WB 1 has an abnormally low mass ($M_{WD} = 0.39 M_\odot$) as compared with the distribution of field DA WD masses, which is sharply peaked between $\sim 0.5 M_\odot$ to $\sim 0.6 M_\odot$ (Bergeron et al., 1992). Given the cluster age and the empirical initial-final mass relation in Claver et al. (2001), any WDs in the cluster should have masses $M_{WD} \gtrsim 0.75 M_\odot$. It is therefore likely that WB 1 is a helium-core white dwarf, WDs formed by binary-star interactions truncating the post-main sequence evolution of a star before He ignition.

Based on the He-core WD evolutionary models and the observed $T_{\rm eff}$ and $\log g$, the logarithmic cooling age of WB 1 is ~ 8.4 (Althaus & Benvenuto, 1997), in sharp disagreement with the cluster age. This suggests three possibilities: that WB 1 is a field He-core WD very near the cluster, that the evolutionary models are incorrect, or that the secondary minimum visible in Fig. 4.29 is the correct model. In the latter case, WB 1 is a normal DA WD foreground to to the cluster. This will be examined by planned higher signal-to-noise observations. Should the He-core interpretation remain the favored model, this object may be useful in constraining the evolution of He-core WDs.

4.3.1 Non-cluster member WDs

Out of seventeen white dwarfs, four were cluster members. The remaining WDs are field WDs, which raises the interesting question of how many field WDs should be expected in these fields. The local space density of field WDs and field WDLF has been measured from proper motion surveys of high-galactic latitude fields, such as Liebert, Dahn, & Monet (1988, hereafter LDM). The open cluster observations might be useful in constraining the field WDLF more accurately, especially for faint WDs.

For example, the NGC 7063 contains four field WDs brighter than $V = 22$ and hotter than $\sim 13000\,\mathrm{K}$. A crude integration of the LDM WDLF results in an expected 1.6 WDs in this field brighter than $V = 22$ and with $T_{\mathrm{eff}} \gtrsim 13000\,\mathrm{K}$, suggesting the LDM WDLF may underestimate the true disk WDLF for hot WDs.

It must be stressed that this example involves a very rudimentary calculation, but this example illustrates that the open cluster WD sample is also a useful series of pencil-beam surveys in the galactic disk extending much fainter than existing field WD surveys. In addition, each of these field WDs has a measured T_{eff} and $\log g$, and so reasonable distance moduli can be established for individual WDs. Careful analysis of the field WD population from the open cluster WD study may permit comparisons of the pencil-beam field WD survey to the local WDLF, local WD mass function, current disk star formation rates, and planetary nebula populations, among many other things.

Table 4.1: Continuum Flux sample regions

Line	Line Center λ_c(Å)	Legendre polynomial sampling ranges (Å)	Linear fit sample ranges (Å)	χ^2 fit range $\lvert\lambda - \lambda_c\rvert$ (Å)
Hβ	4861.3	4460.5-4721.3; 5001.3-5300.3	4716.3-4726.3; 4996.3-5006.3	140
Hγ	4340.5	4176.7-4220.5; 4460.5-4721.3	4215.5-4225.5; 4455.5-4465.5	120
Hδ	4101.7	3915.1-3922.1; 4018.1-4028.7; 4176.7-4220.5	4023.7-4033.7; 4171.7-4181.7	75
Hϵ	3970.1	3850.0-3859.1; 3915.1-3922.1; 4018.1-4028.7	3917.1-3927.1; 4013.1-4023.1	50
H8	3889.1	3850.0-3859.1; 3915.1-3922.1; 4018.1-4028.7	3854.1-3864.1; 3910.1-3920.1	30

Table 4.2: Comparison of measured $T_{\rm eff}$ and $\log g$ to previously-published measurements

	This Work				Previous Measurements				
Object	$T_{\rm eff}$ K	$\delta T_{\rm eff}$ K	$\log g$	$\delta \log g$	$T_{\rm eff}$ K	$\delta T_{\rm eff}$ K	$\log g$	$\delta \log g$	Reference[a]
WD 0302+027	38500	···	7.70	···	35830	···	7.79	···	BSL
					35082	257	7.64	0.06	FKB
WD 0346-011	39500	···	>9.00	···	40540	···	9.22	···	BSL
					43102	1982	9.09	0.09	BRB
					34282	696	8.03	0.19	M89
WD 0349+247	31500	···	8.45	···	32920	···	8.60	···	BSL
(Pleiad WD)					31660	···	8.78	···	BLF
					28574	449	8.25	0.20	KSW
WD 0352+096	14800	425	8.15	0.05	14770	···	8.16	···	BLF
					14176	147	8.26	0.08	M89
					14548	178	8.19	0.10	KSW
WD 1737+419	20600	550	7.95	0.11	19458	309	7.97	0.08	FKB
WD 1936+327	20200	100	7.85	0.02	21260	···	7.84	···	BSL
					21240	92	7.77	0.02	FKB
					23265	143	8.17	0.03	M89
WD 2025+554	29800	300	7.95	0.06	30486	112	7.76	0.02	FKB
WD 2046+396	> 50000	···	7.45	···	63199	921	7.77	0.05	FKB

[a]BLF=Bergeron, Liebert, & Fulbright (1995); BRB=Bragaglia, Renzini, & Bergeron (1995); BSL=Bergeron, Saffer, & Liebert (1992); FKB=Finley, Koester, & Basri (1997); KSW=Koester, Schulz, & Weidemann (1979); M89=McMahan (1989).

Table 4.3: Comparison of derived M_{WD} and cooling ages to those derived from previously-published measurements of $T_{\rm eff}$ and $\log g$.

	This Work				Previous Measurements[a]				
Object	M_{WD} $M_\odot$	δM_{WD} $M_\odot$	log(age)	$\delta_{\rm age}$	M_{WD} $M_\odot$	δM_{WD} $M_\odot$	log(age)	$\delta_{\rm age}$	Reference[a]
WD 0302+027	0.53	···	6.57	···	0.56	···	6.70	···	BSL
					0.50	0.02	6.67	0.01	FKB
WD 0349+247	0.92	···	7.54	···	1.01[c]	···	7.68[c]	···	BSL
(Pleiad WD)					1.12[c]	···	7.90[c]	···	BLF
					0.79	0.12	7.45	0.33	KSW
WD 0352+096	0.70	0.03	8.42	0.06	0.71	···	8.43	···	BLF
					0.77	0.05	8.54	0.06	M89
					0.73	0.06	8.47	0.07	KSW
WD 1737+419	0.60	0.06	7.79	0.16	0.61	0.04	7.92	0.10	FKB
WD 1936+327	0.54	0.01	7.73	0.03	0.54	···	7.61	···	BSL
					0.51	0.01	7.56	0.02	FKB
					0.73	0.02	7.79	0.05	M89
WD 2025+554	0.62	0.03	7.02	0.04	0.53	0.01	6.92	0.01	FKB

[a]Derived from W95 models using published values of $T_{\rm eff}$ and $\log g$

[b]BLF=Bergeron, Liebert, & Fulbright (1995); BRB=Bragaglia, Renzini, & Bergeron (1995); BSL=Bergeron, Saffer, & Liebert (1992); FKB=Finley, Koester, & Basri (1997); KSW=Koester, Schulz, & Weidemann (1979); M89=McMahan (1989).

[c] Extrapolated value; outside grid of W95 models

Table 4.4: Results of spectroscopy – identifications and fit model parameters

Cluster	Object	Other Name[a]	ID[b]	$T_{\rm eff}$(K)	$\log g$
NGC 1039	2	LB 3569	DA	20600^{+1200}_{-1700}	$7.80^{+0.30}_{-0.23}$
	3		DA	···	···
IC 4665	26		A	···	···
	32		QSO	···	···
NGC 6633	1		sd	···	···
	2	RA 6633-7	FHB	···	···
	3	RA 6633-4	sd	···	···
	4	RA 6633-5	DA	19200^{+1000}_{-1100}	$8.30^{+0.15}_{-0.18}$
	5	RA 6633-1	DO	···	···
	6		FHB	···	···
	7		DA	17600^{+1000}_{-1100}	$8.40^{+0.13}_{-0.15}$
	8		DA	19600^{+4100}_{-3500}	$8.05^{+0.50}_{-0.50}$
	9		FHB	···	···
	10		sd	···	···
	11		sd	···	···
	12		DA	18200^{+1300}_{-1600}	$8.00^{+0.28}_{-0.23}$
	13		DA	$\gtrsim 35000$	···
	14	RA 6633-6	DB	···	···
	15		DA	26600^{+2350}_{-3000}	$7.75^{+0.43}_{-0.41}$
	16		DB	~ 16300	~ 8.0
	19		QSO($z = 1.97$)	···	···
	23	RA 6633-2	sd	···	···
	27		DA	13800^{+2300}_{-1850}	$7.75^{+0.53}_{-0.54}$
	29		QSO($z = 1.6$)	···	···
	32		A	···	···
NGC 7063	1		DA	15000^{+1300}_{-4000}	$7.55^{+0.47}_{-0.28}$
	2		DA	15600^{+400}_{-600}	$7.95^{+0.09}_{-0.07}$

[a] RA=Romanishin & Angel (1980)

[b] sd=hot subdwarf; FHB=field horizontal branch; A=A-type star, B=B-type star

[c] 90% confidence level spans entire model range

Table 4.4: (cont.)

Cluster	Object	Other Name[a]	ID[b]	$T_{\rm eff}$(K)	$\log g$
	3		DA	18200^{+1700}_{-1300}	$7.85^{+0.24}_{-0.29}$
	4		DA	13800^{+8830}_{-3800}	7.90^{c}
	6		DA	17200^{+8300}_{-5900}	7.75^{c}
	16		QSO($z = 1.4$)	$\cdots$	$\cdots$

[a] RA=Romanishin & Angel (1980)

[b] sd=hot subdwarf; FHB=field horizontal branch; A=A-type star, B=B-type star

[c] 90% confidence level spans entire model range

Table 4.5: Masses, cooling ages, and distance moduli of observed white dwarfs

Cluster	WB	$M_{WD}(M_\odot)$	log(age)[a]	$(m-M)_V^b$	Member[c]
NGC 1039	2[d]	$0.52^{+0.16}_{-0.09}$	$7.65^{+0.36}_{-0.22}$	$8.56^{+0.35}_{-0.48}$	1
NGC 6633	4	$0.81^{+0.09}_{-0.11}$	$8.20^{+0.15}_{-0.16}$	$7.52^{+0.28}_{-0.30}$	0
	7	$0.87^{+0.08}_{-0.10}$	$8.38^{+0.14}_{-0.13}$	$7.66^{+0.28}_{-0.27}$	0
	8	$0.65^{+0.31}_{-0.24}$	$7.97^{+0.51}_{-0.63}$	$8.87^{+0.86}_{-0.95}$	1
	12	$0.62^{+0.11}_{-0.12}$	$8.05^{+0.25}_{-0.25}$	$9.86^{+0.35}_{-0.45}$	0
	13	$\cdots$	$\lesssim 7.0$	$\gtrsim 10.5$	0
	15	$0.52^{+0.23}_{-0.15}$	$7.13^{+0.51}_{-0.16}$	$9.78^{+0.68}_{-0.75}$	0
	16[e]	~ 0.59	~ 8.3	~ 9.0	0
	27	$0.48^{+0.31}_{\star}$	$8.28^{+0.29}_{-0.21}$	$9.01^{+0.40}_{-0.72}$	1
NGC 7063	1[f]	$0.39^{+0.22}_{-0.13}$	$8.05^{+0.62}_{-0.17}$	$9.45^{+0.39}_{-1.27}$	1
	2	$0.59^{+0.05}_{-0.03}$	$8.24^{+0.08}_{-0.07}$	$8.08^{+0.11}_{-0.15}$	0
	3	$0.54^{+0.13}_{-0.13}$	$7.92^{+0.27}_{-0.28}$	$10.18^{+0.42}_{-0.43}$	0
	4	0.55[g]	$8.36^{\star}_{-0.96}$	$9.86^{+1.74}_{\star}$	0
	6	0.49[g]	$7.95^{+0.95}_{-0.61}$	$11.30^{+0.60}_{-1.80}$	0

[a] WD cooling age

[b] apparent distance modulus

[c] 1=photometry consistent with cluster membership; 0=inconsistent with cluster membership

[d] Photometry from Anthony-Twarog (1982)

[e] Estimates determined using Bergeron et al. (1995)

[f] Age assumes C/O core

[g] 90% confidence level spans entire model range

$\star$ 90% confidence limit extends beyond model grid

Figure 4.1: Profiles of Koester model atmosphere Balmer lines for different effective temperatures and surface gravities. From bottom to top, lines are Hβ through H8; fluxes have been normalized to a pseudo-continuum as described in text and have been vertically offset. Surface gravities are $\log g$ =7.0 (solid line), 7.5 (dotted), 8.0 (dashed), 8.5 (long-dashed) and 9.0 (dot-dashed).

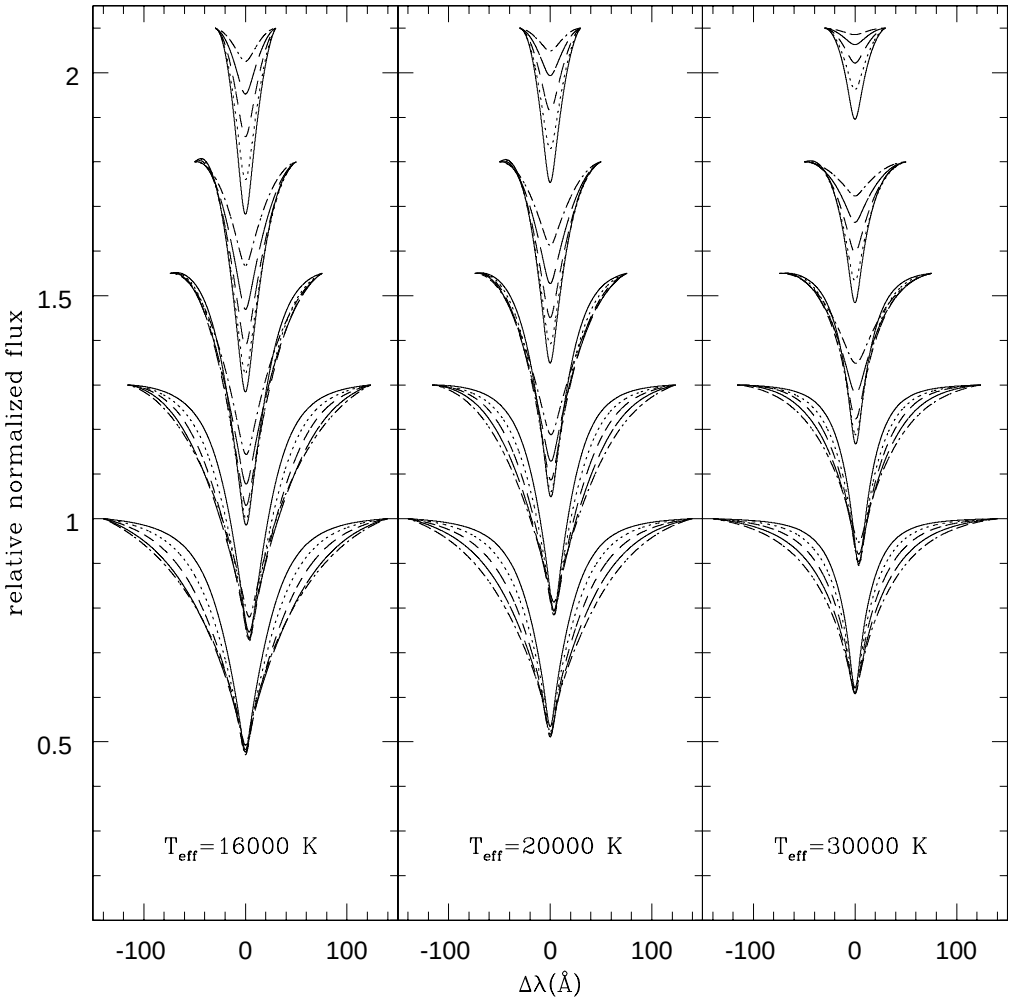

Figure 4.2: Contour plot of confidence levels from χ^2 fitting of models to spectral data for WD 0352+096. Black lines indicate 90% confidence levels for Hβ (solid), Hγ (dotted), Hδ (dashed), Hϵ (dot-dashed) and H8(dash-dot-dot-dotted). Thick blue line indicates 95% confidence level for simultaneous fit. Dashed magenta lines indicate cooling tracks of WDs of a constant mass; dotted blue lines represent lines of constant cooling age.

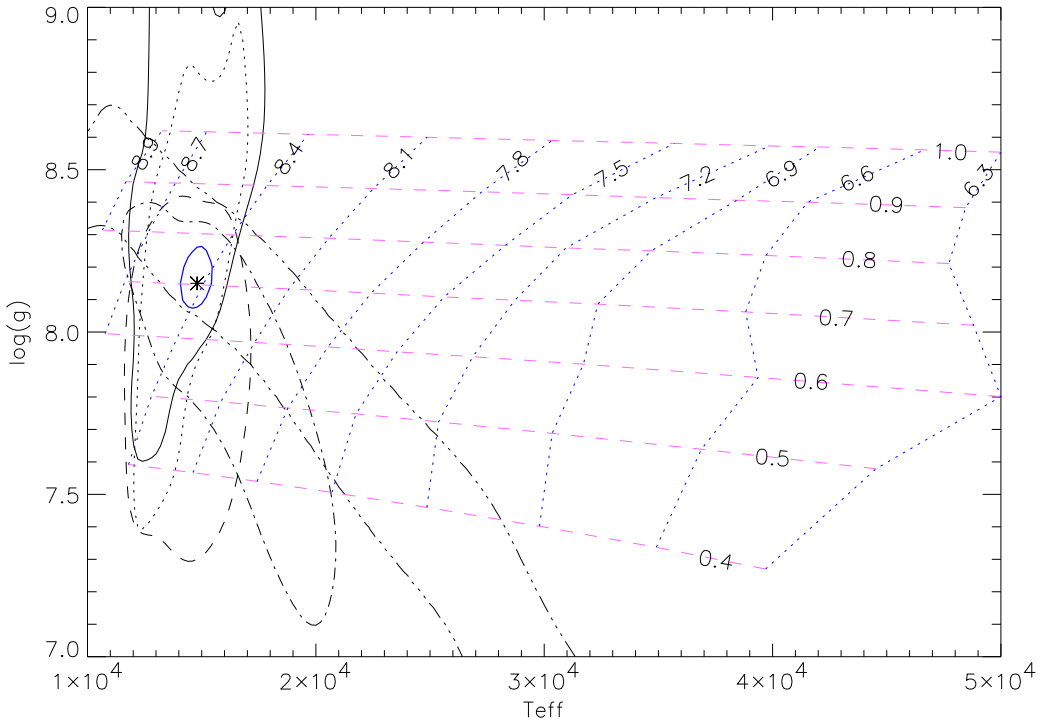

Figure 4.3: Consistency check for Balmer-line fitting of the spectrum of NGC 6633 WB12. Dashed and dotted lines indicates the 68.3%, and 90% confidence contours for $T_{\rm eff}$ and $\log g$ as determined from individual observations. Solid lines indicate 68.3%, 90%, and 95.4% confidence levels for the combined observations. Starred symbols indicate the best fitting models in each case. The 68.3% confidence contours for individual observations overlap with each other and the combined result, indicating consistent results.

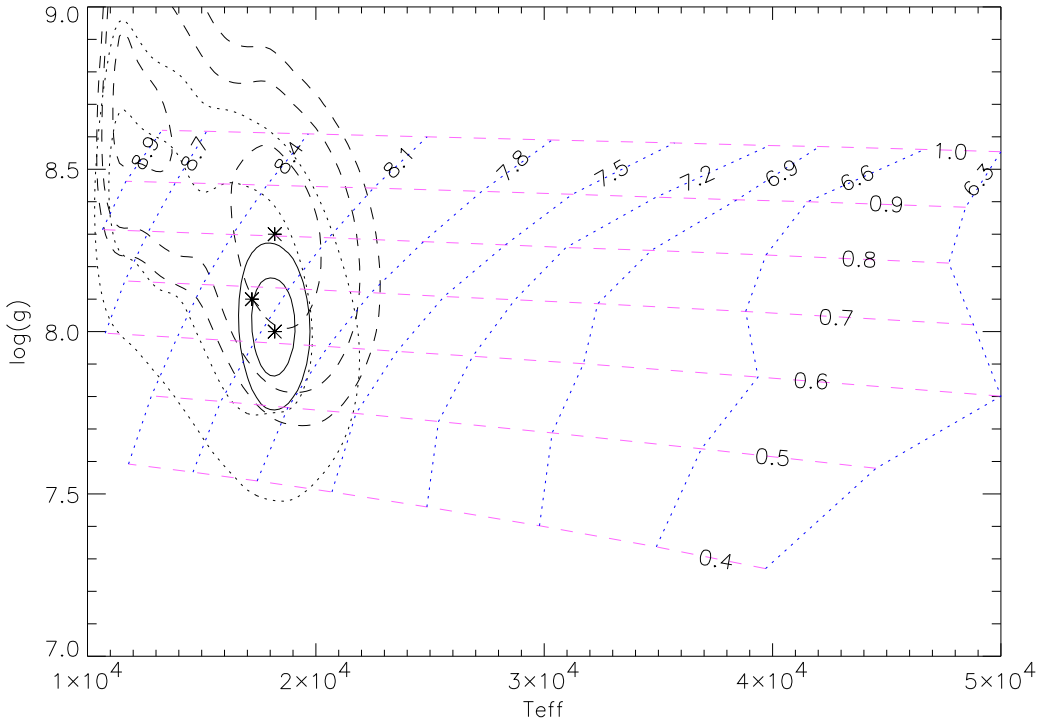

Figure 4.4: Comparison of observed, normalized spectrum for WD 0352+096 (histogram) to atmospheric models closest to best fit $T_{\rm eff}$ and $\log g$. Models are $T_{\rm eff}$ =14000K, $\log g$ =8.00 (dotted) and $T_{\rm eff}$ =15000K, $\log g$ =8.25 (dashed).

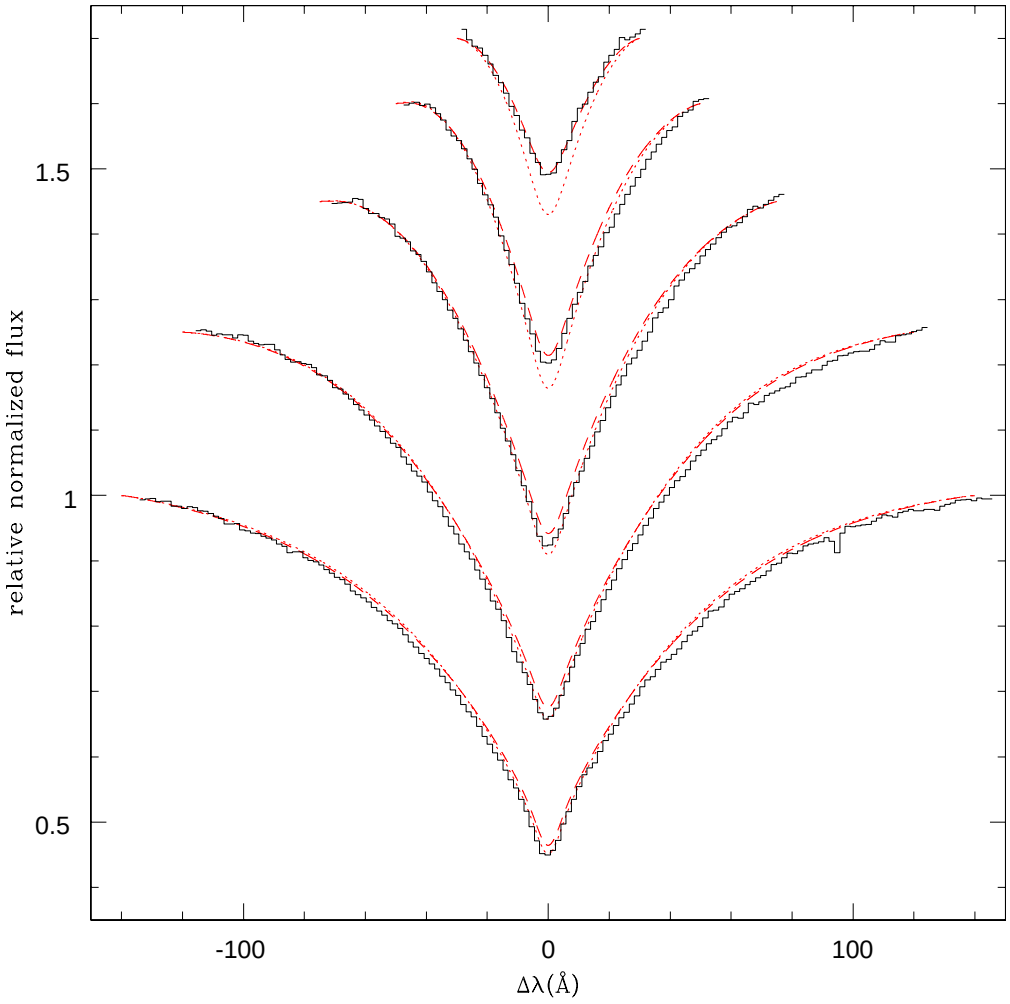

Figure 4.5: Four atmospheric models nearest χ^2 minimum for the Pleiades white dwarf (WD 0349+247). Models shown are for $T_{\rm eff}$ =30000K (red), 35000K (blue) and $\log g$ =8.5 (solid), 9.0 (dotted).

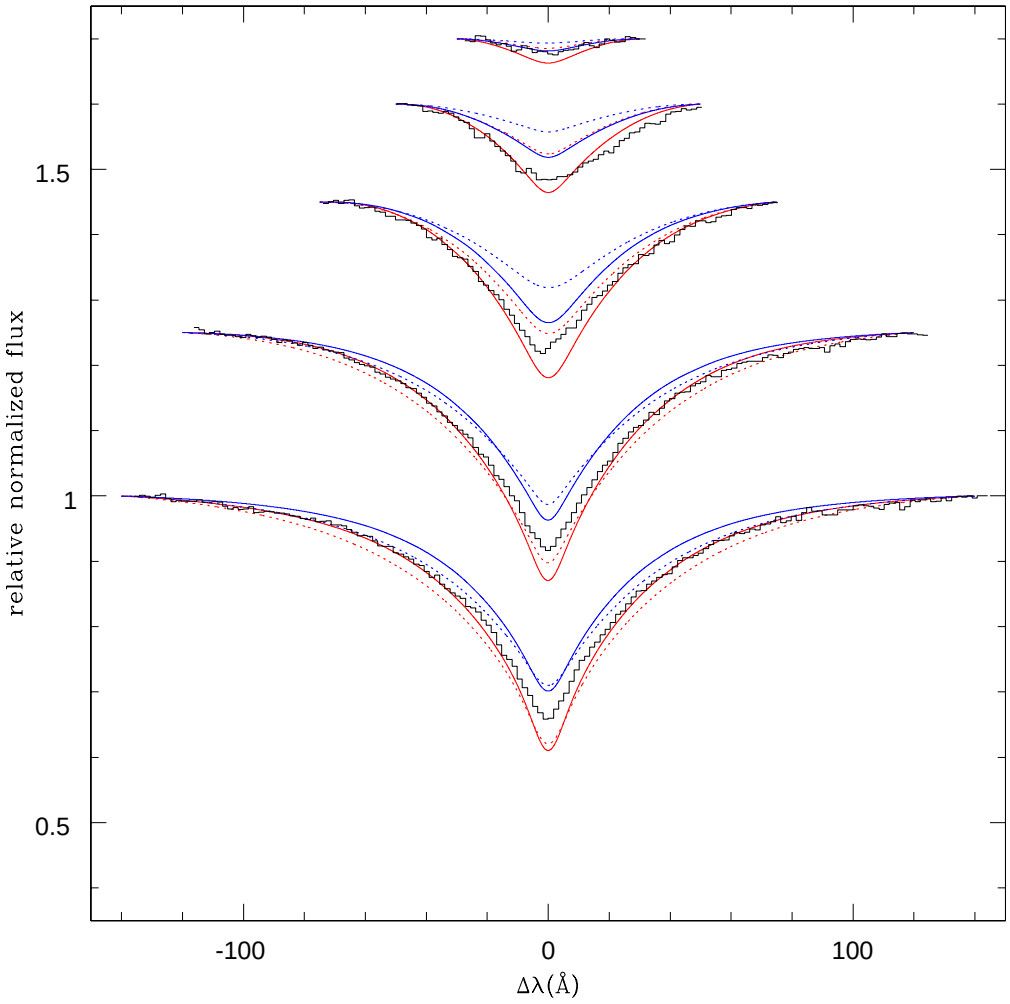

Figure 4.6: An example of cluster membership determination using a combination of spectroscopic and photometric data. Contours of 68.3%, 90%, and 95.4% confidence for the atmospheric parameters of WD N6633 WB 4 are shown in black. Green contours indicate the possible locations of a cluster member WD with the same apparent V magnitude as the WD, with 2σ contours including uncertainties in photometry and cluster distance modulus indicated. Since the WD contours do not overlap with the photometric contours, the WD is not a cluster member.

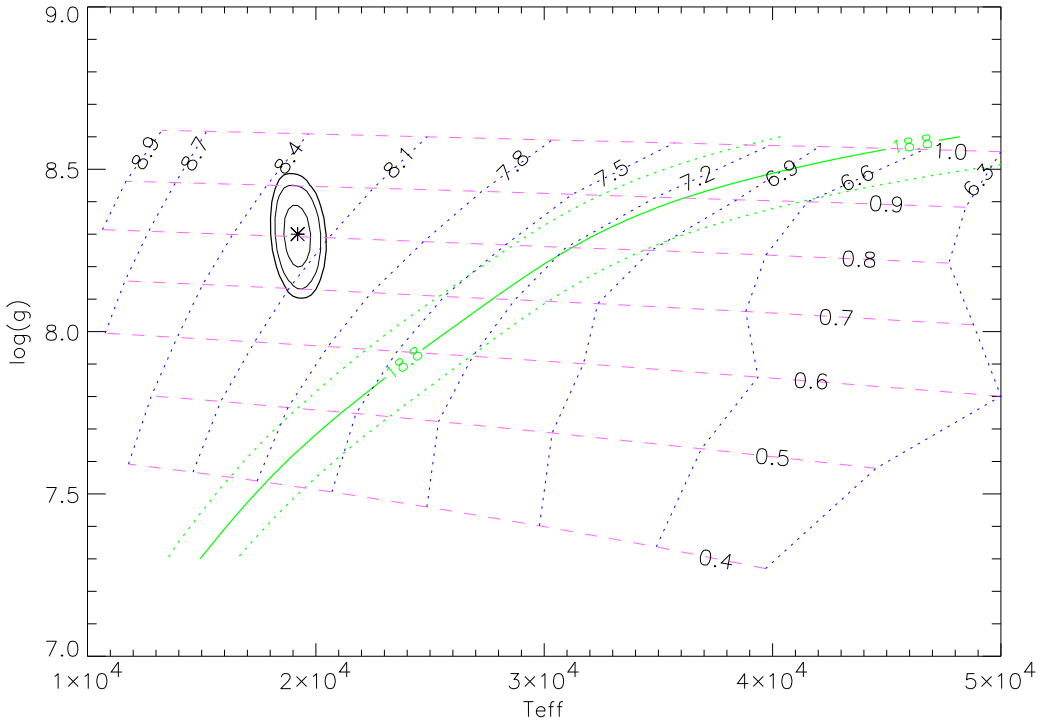

Figure 4.7: Confidence intervals in $T_{\rm eff}$ and $\log g$ for the non-white dwarf/sdB NGC6633 WB 1, analyzed as if it were a WD. Contours indicate 90% likelihood levels for Hβ (solid), Hγ (dotted), Hδ (dashed) and H8 (dot-dashed); Hϵ produced no 90% or better fit.

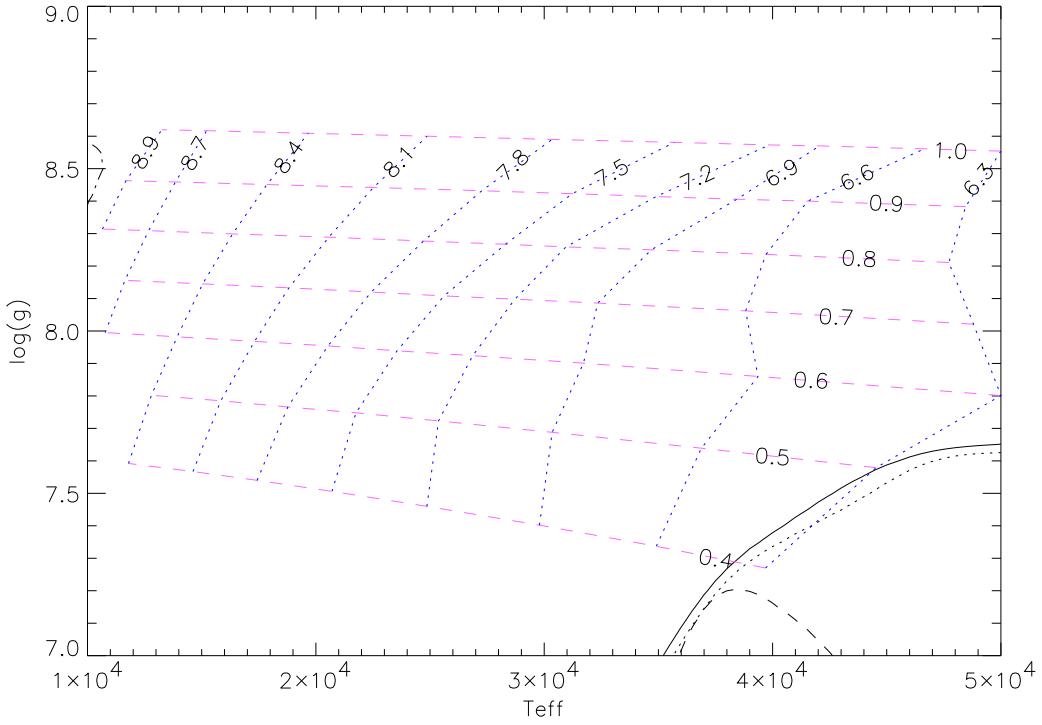

Figure 4.8: Balmer-line profiles from non-WD NGC 6633 WB 1 (histogram) compared with best-fitting models: $T_{\rm eff}$ =30000K, $\log g$ =7.0 (dotted) and $T_{\rm eff}$ =40000K, $\log g$ =7.0 (dashed). The observed Balmer lines are clearly narrower than the models, signifying lower surface gravity.

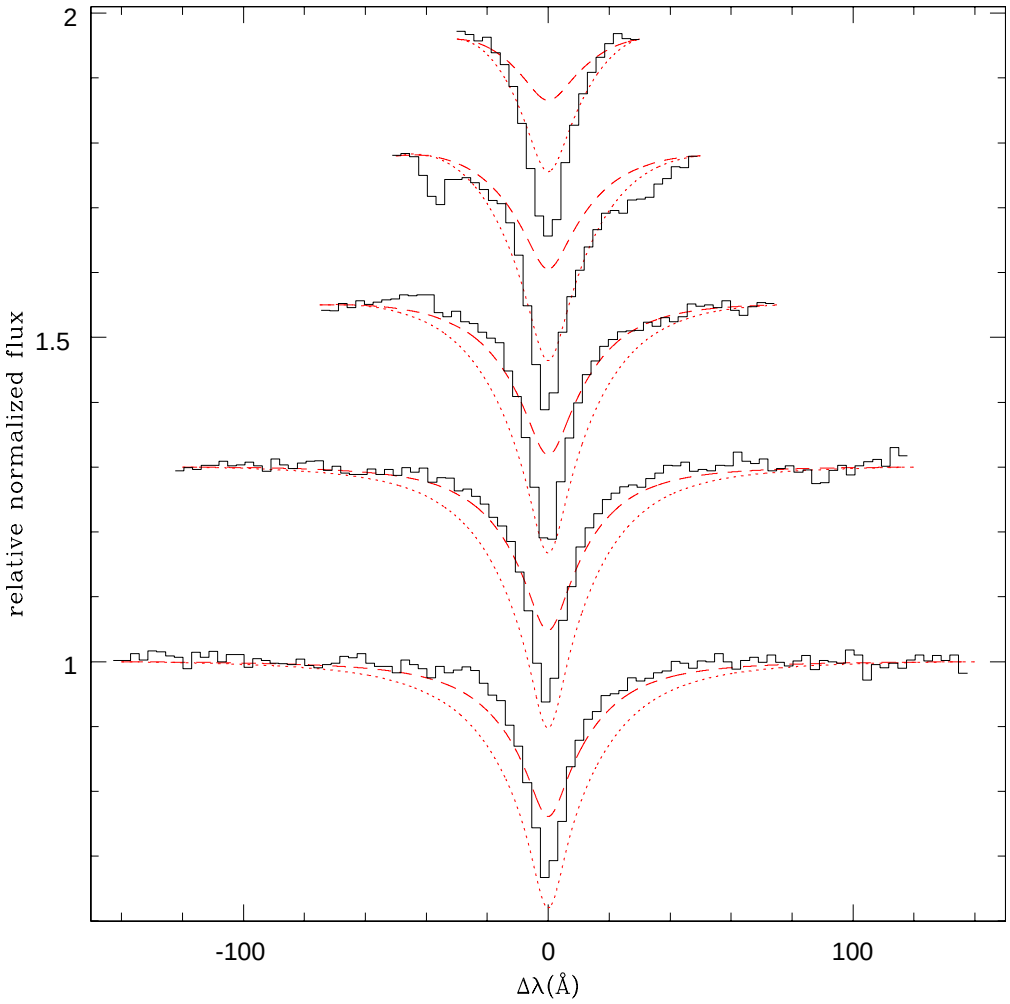

Figure 4.9: Spectra obtained in NGC 1039 (top panel) and IC 4665 (bottom panel). Spectra have been normalized and offset by arbitrary amounts.

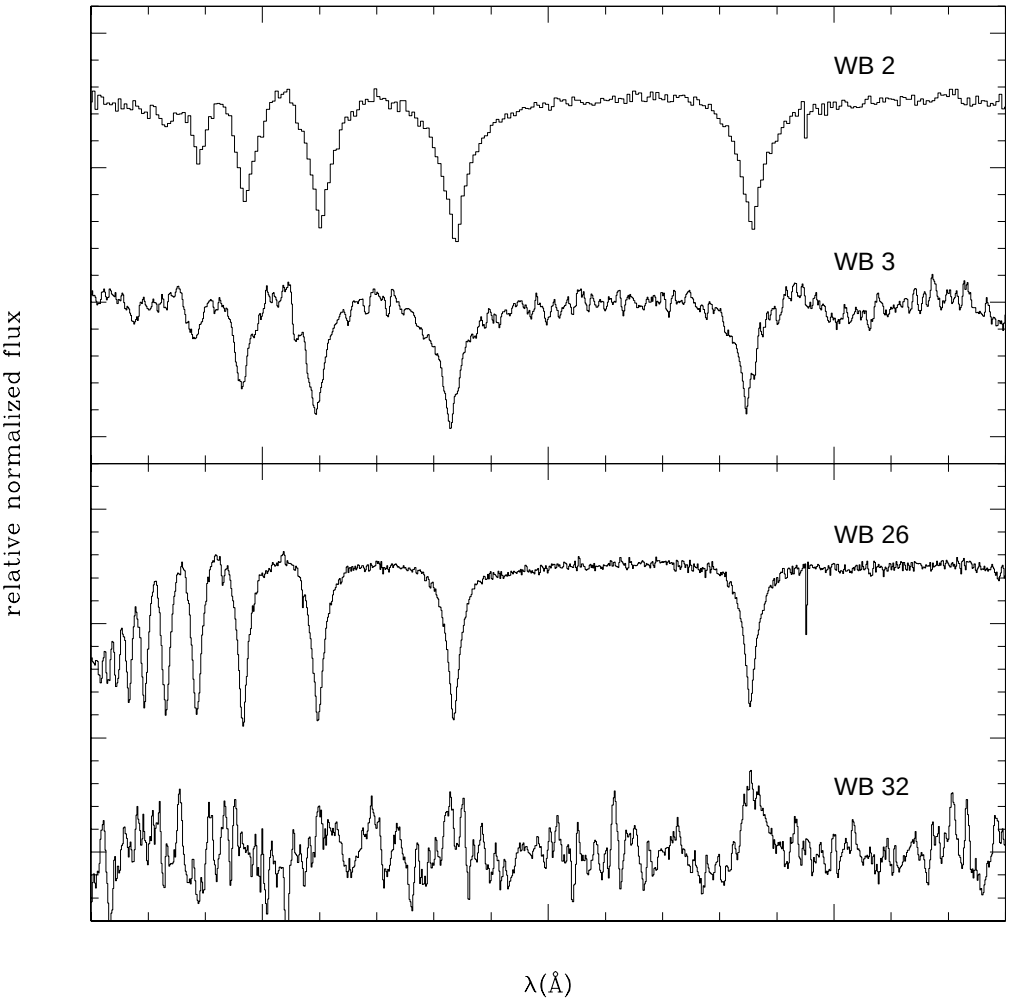

Figure 4.10: $T_{\rm eff} - \log g$ plot for NGC 1039 WB 2. Black contours indicate 90% and 95.4% confidence levels; the star indicates the best-fitting model. Dotted blue lines indicate lines of constant WD cooling age, labels give logarithmic ages. The solid blue line approximates the cluster age. The dashed magenta lines indicate lines of constant WD mass, indicated in solar masses. The solid green curve indicates possible locations in the plane for cluster-member WDs with the same V-band photometry as the candidate. Dotted green lines indicate 2σ photometric errors, including errors in distance modulus and extinction. Intersection of the green curves with the confidence contours suggests cluster membership for the WD.

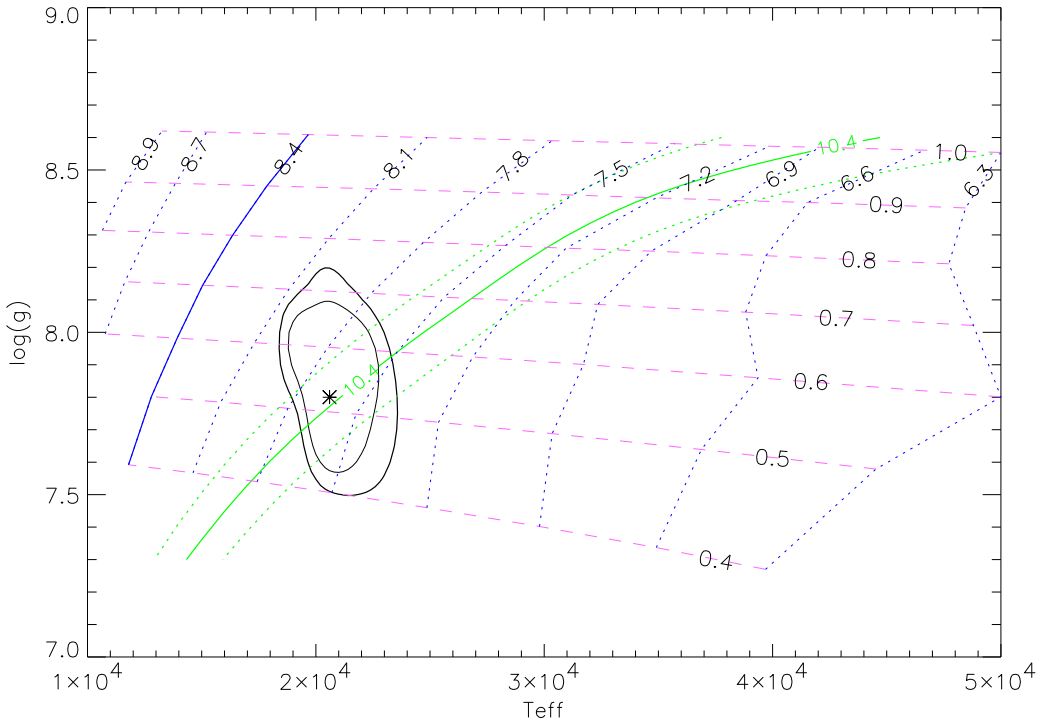

Figure 4.11: Plot of Balmer-line profiles for NGC 1039 WB 2. Black histogram is observed spectrum. The magenta curve is the model for $T_{\rm eff} = 20000$K and $\log g = 7.75$; the dashed blue curve is the model profile for $T_{\rm eff} = 22000$K, $\log g = 8.25$

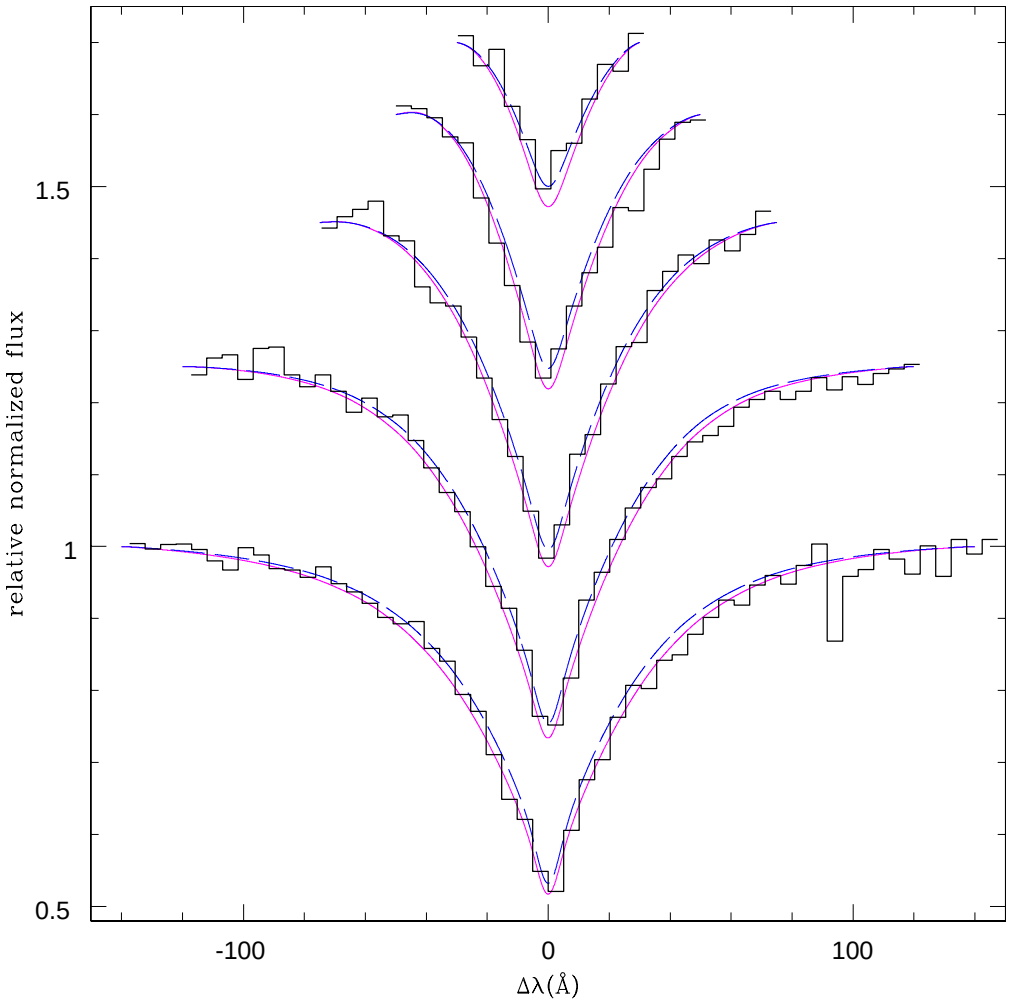

Figure 4.12: Spectra of confirmed DA WDs obtained in the field of NGC 6633. Spectra are normalized by the continuum and offset by arbitrary amounts.

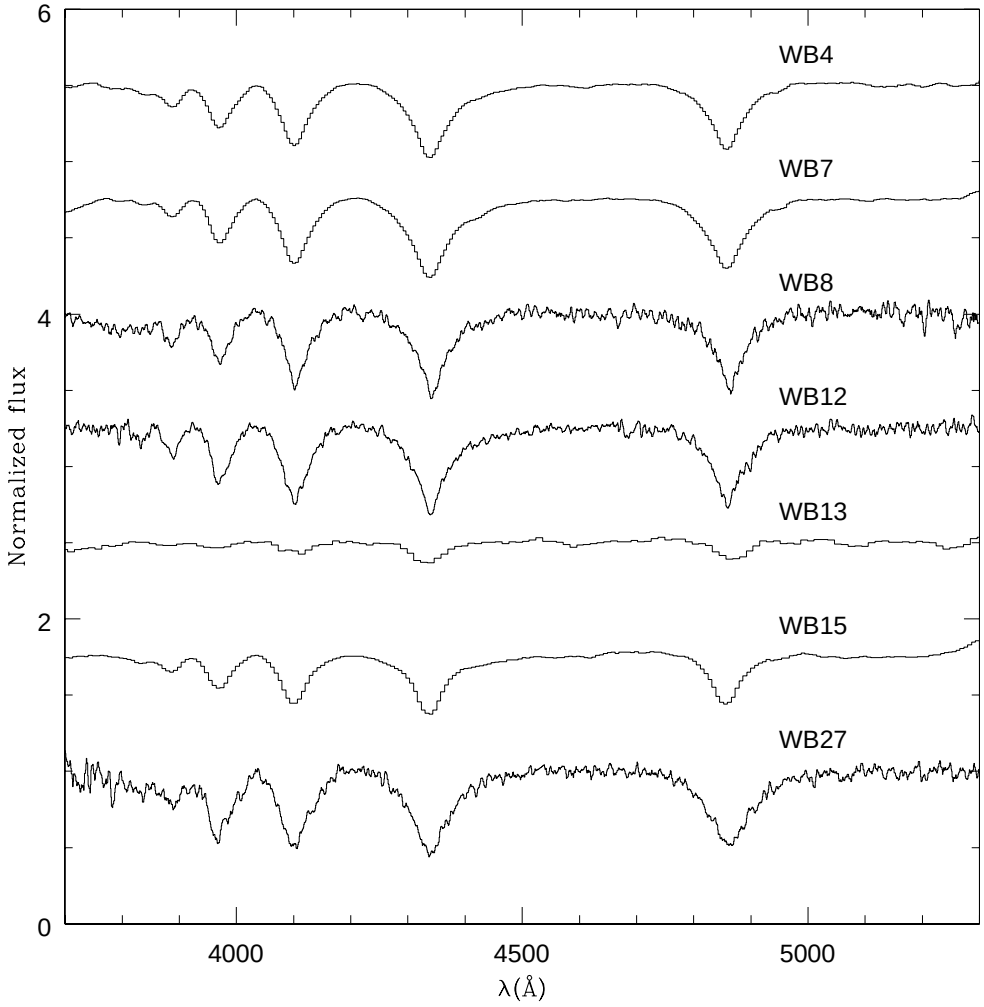

Figure 4.13: Spectra of non-DA objects obtained in the field of NGC 6633. The objects include DB WDs (top panel), hot subdwarf and other B-type stars (second panel), field horizontal branch and other A-type stars (third panel), and QSOs (bottom panel). Spectra are normalized by the continuum and offset by arbitrary amounts.

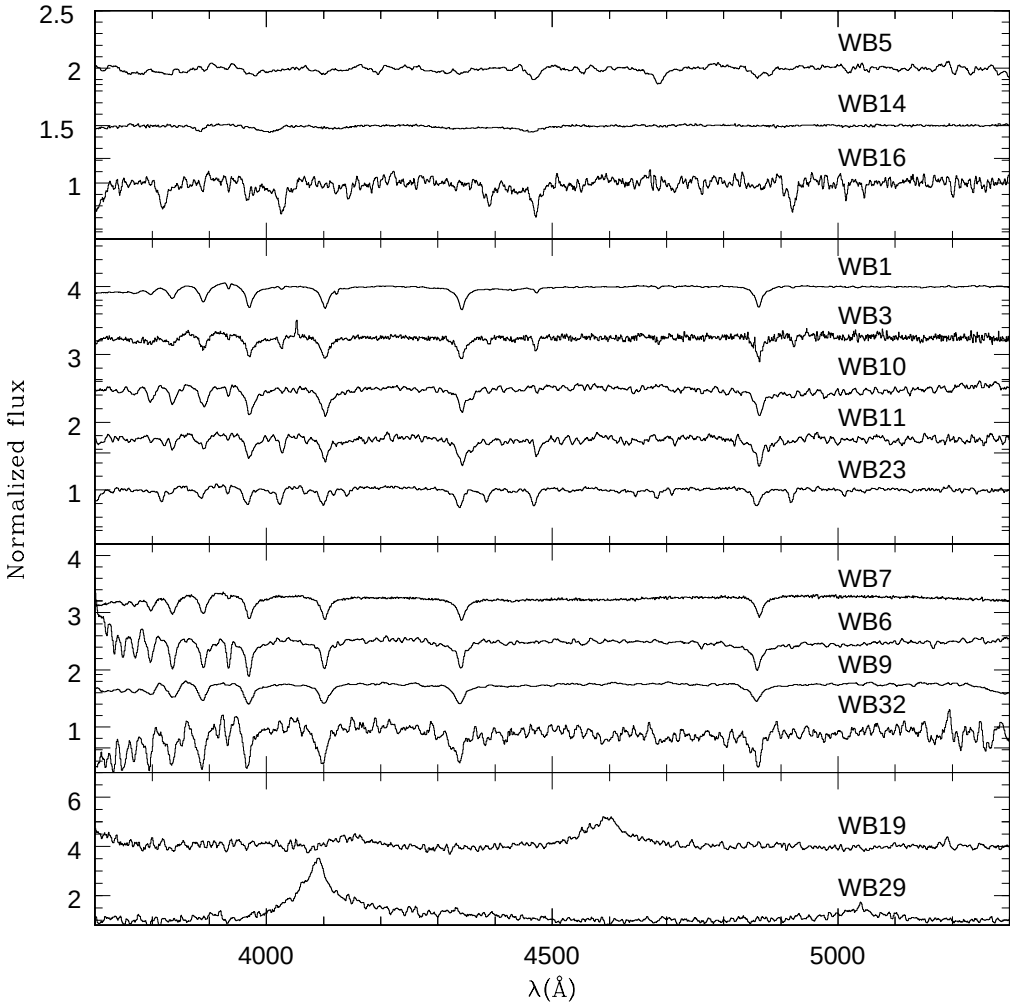

Figure 4.14: $T_{\rm eff} - \log g$ plot for NGC 6633 WB 4. Black contours indicate 68.3%, 90%, and 95.4% confidence levels; the star indicates the best-fitting model. Dotted blue lines indicate lines of constant WD cooling age, labels give logarithmic ages. The solid blue line approximates the cluster age. The dashed magenta lines indicate lines of constant WD mass, indicated in solar masses. The solid green curve indicates possible locations in the plane for cluster-member WDs with the same V-band photometry as the candidate. Dotted green lines indicate 2σ photometric errors, including errors in distance modulus and extinction. Intersection of the green curves with the confidence contours suggests cluster membership for the WD.

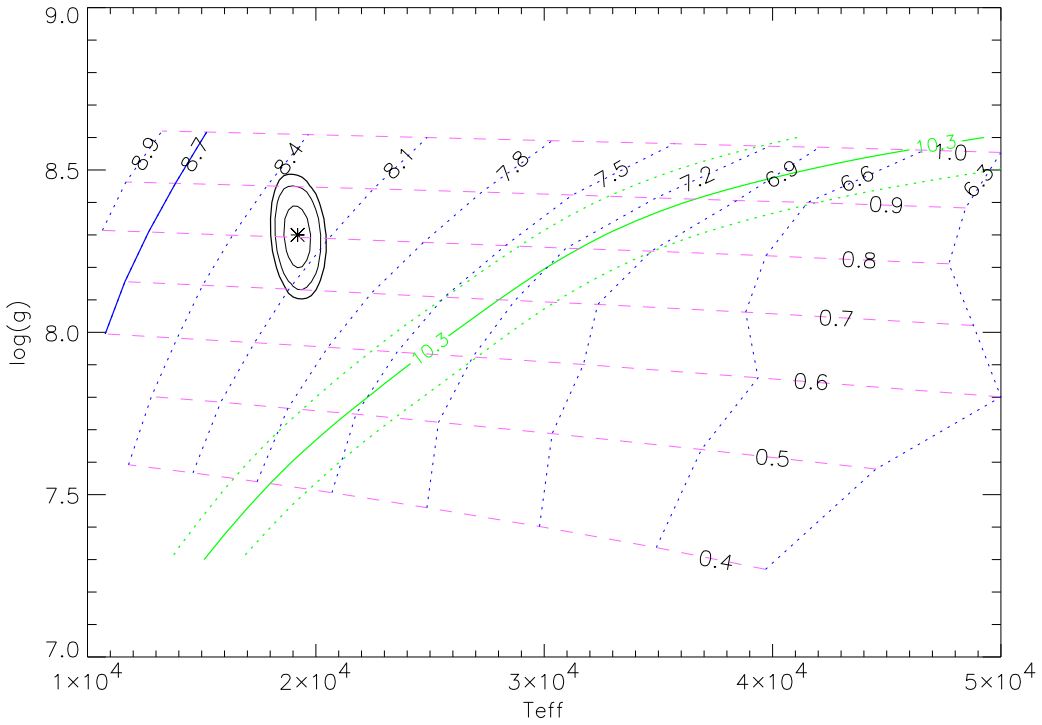

Figure 4.15: Plot of Balmer-line profiles for NGC 6633 WB 4. Black histogram is observed spectrum. The magenta curve is the model for $T_{\rm eff}$ =18000 K and $\log g$ =8.25; the dashed blue curve is the model profile for $T_{\rm eff}$ =19000 K, $\log g$ =8.50.

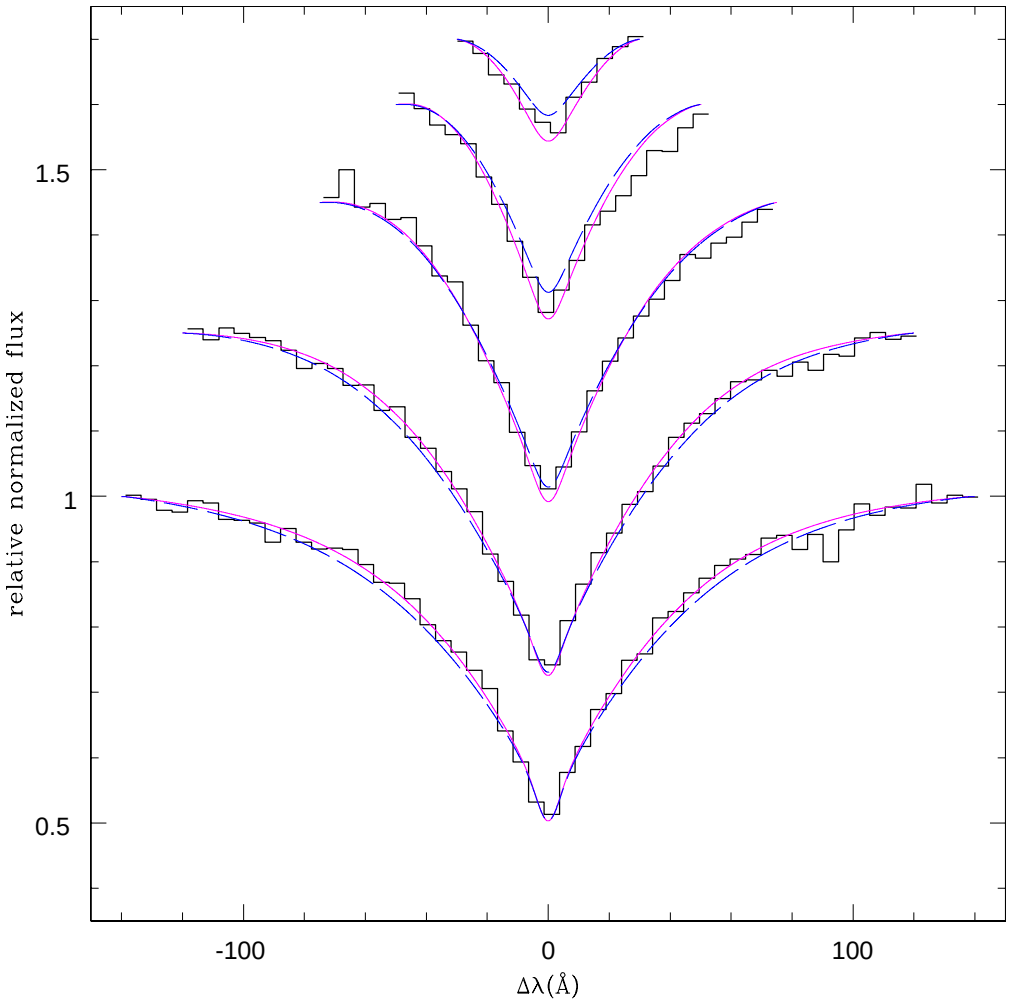

Figure 4.16: Same as in Fig. 4.14, except for NGC 6633 WB 7.

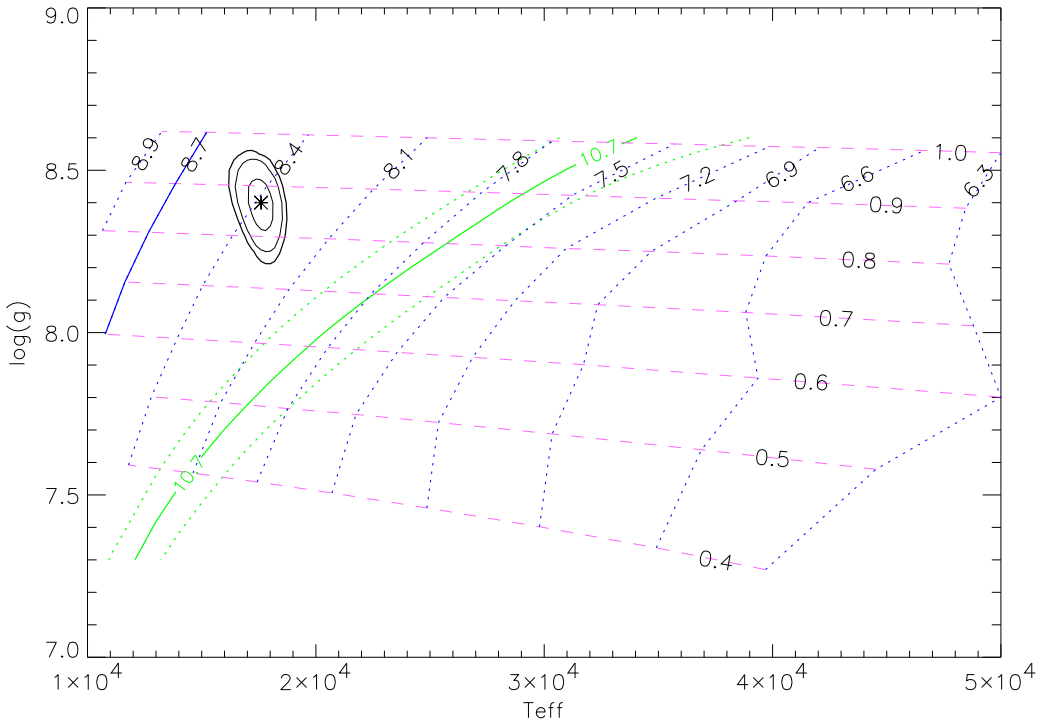

Figure 4.17: Plot of Balmer-line profiles for NGC 6633 WB 7. Black histogram is observed spectrum. The magenta curve is the model for $T_{\rm eff}$ =17000 K and $\log g$ =8.50; the dashed blue curve is the model profile for $T_{\rm eff}$ =18000 K, $\log g$ =8.50.

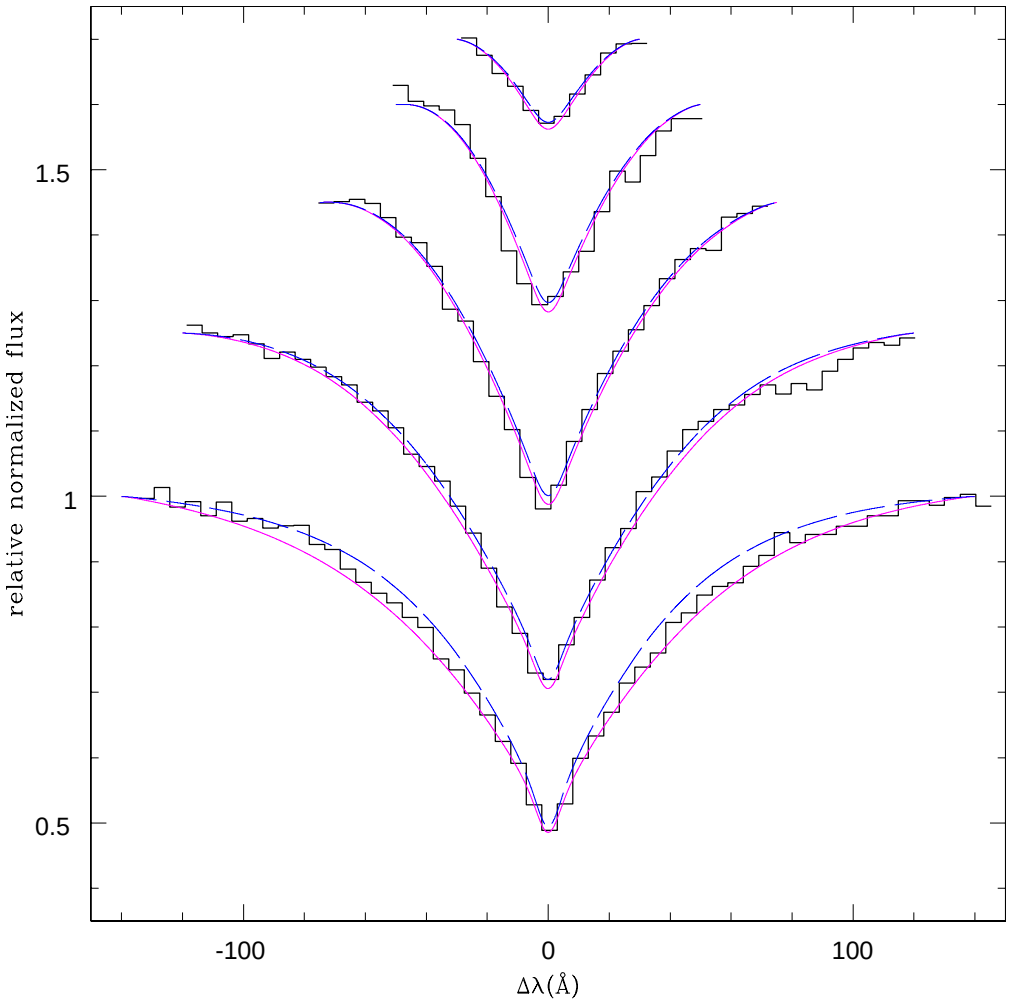

Figure 4.18: Same as in Fig. 4.14, except for NGC 6633 WB 8.

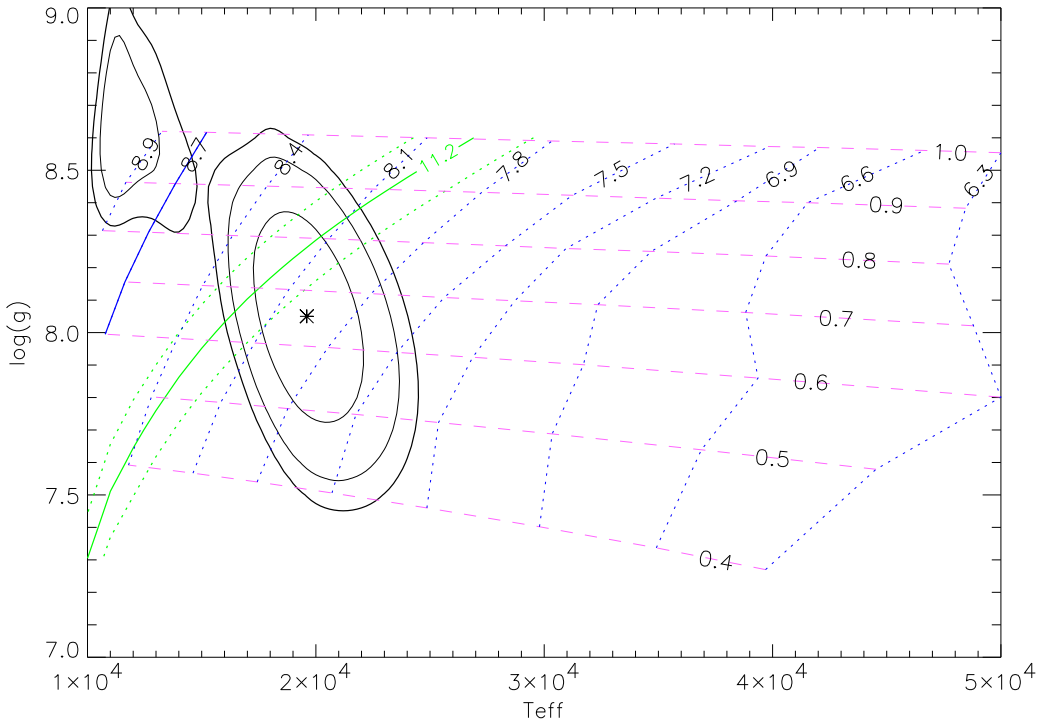

Figure 4.19: Plot of Balmer-line profiles for NGC 6633 WB 8. Black histogram is observed spectrum. The magenta curve is the model for $T_{\rm eff}$ =19000 K and $\log g$ =8.00; the dashed blue curve is the model profile for $T_{\rm eff}$ =20000 K, $\log g$ =8.00.

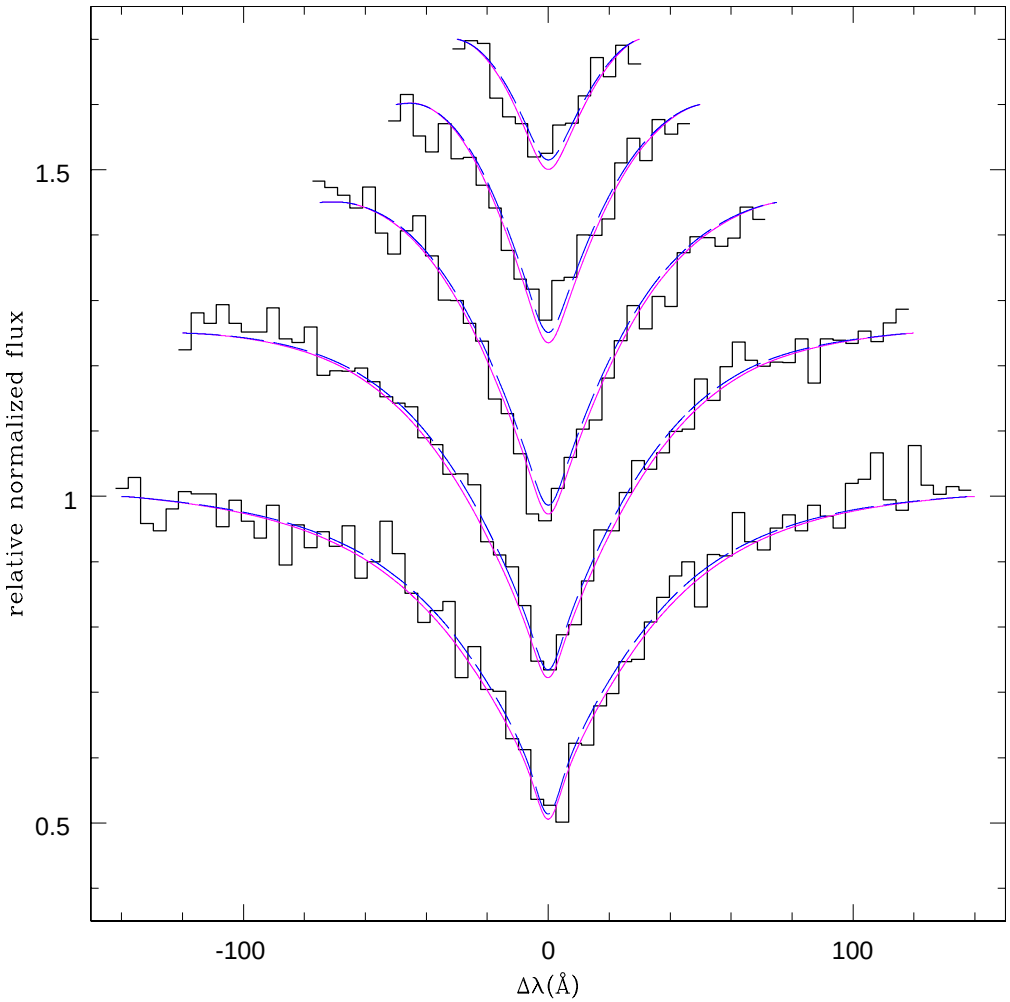

Figure 4.20: Same as in Fig. 4.14, except for NGC 6633 WB 12.

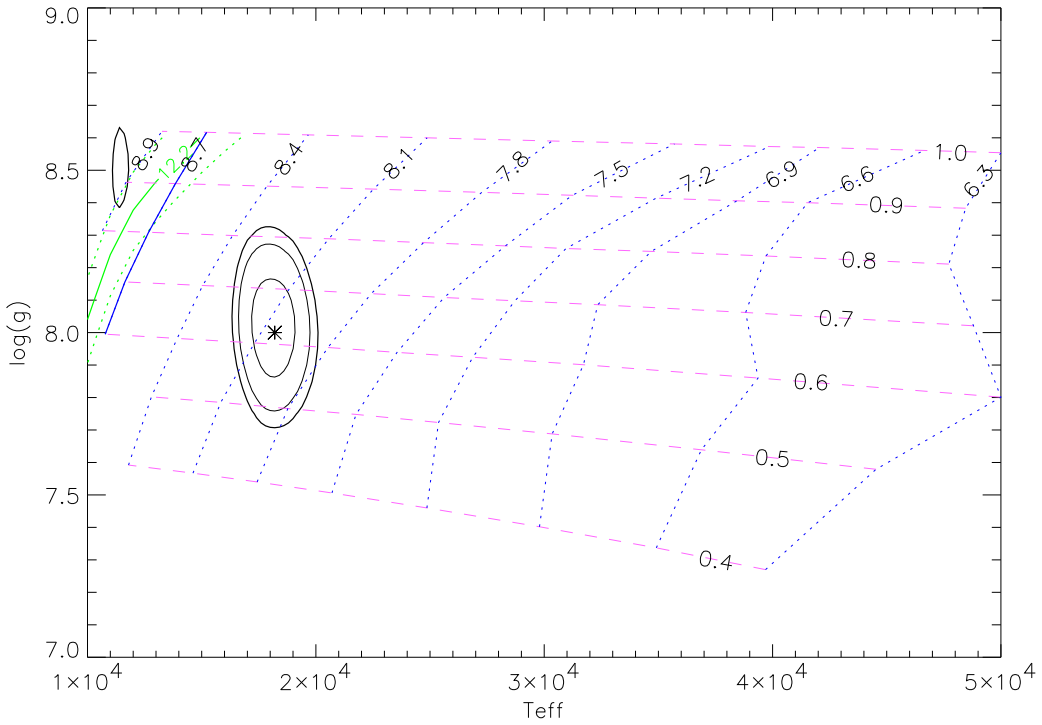

Figure 4.21: Plot of Balmer-line profiles for NGC 6633 WB 12. Black histogram is observed spectrum. The magenta curve is the model for $T_{\rm eff}$ =18000 K and $\log g$ =8.00; the dashed blue curve is the model profile for $T_{\rm eff}$ =20000 K, $\log g$ =8.00.

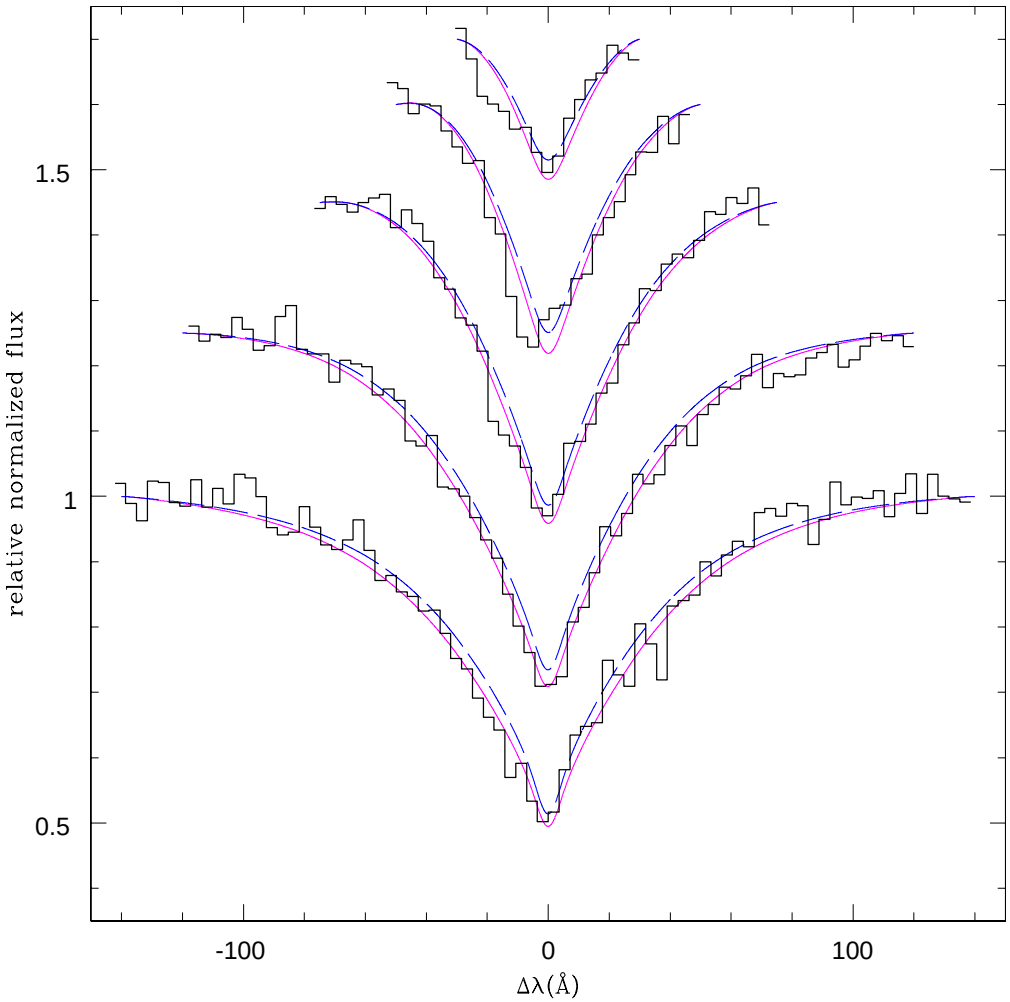

Figure 4.22: Same as in Fig. 4.14, except for NGC 6633 WB 13.

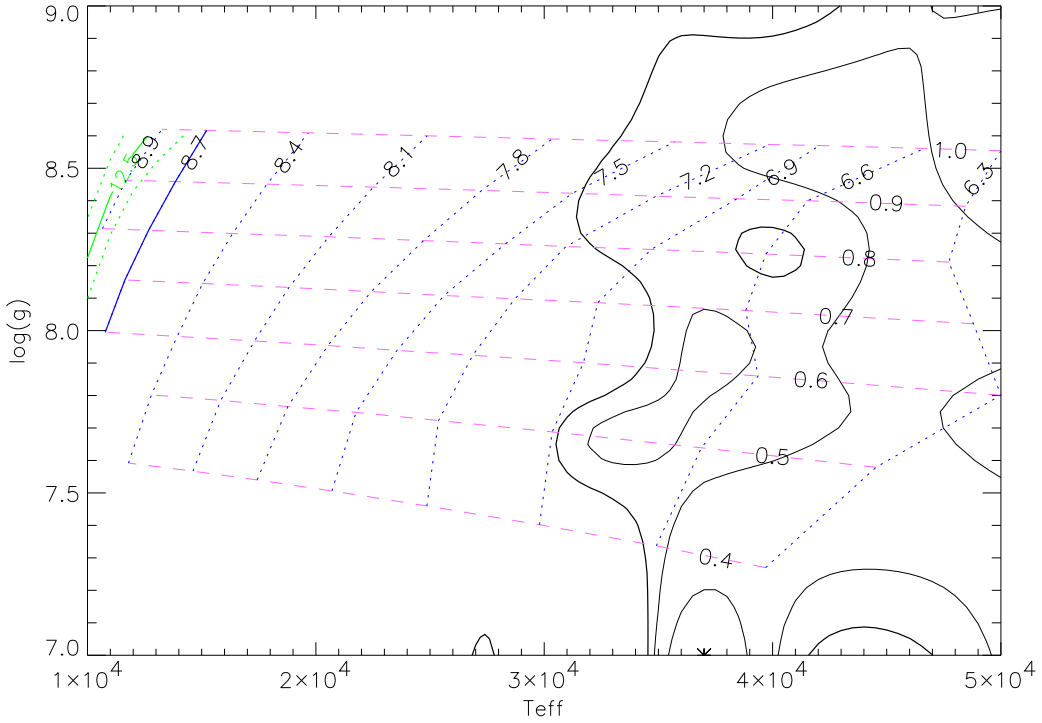

Figure 4.23: Plot of Balmer-line profiles for NGC 6633 WB 13. Black histogram is observed spectrum. The magenta curve is the model for $T_{\rm eff}$ =35000 K and $\log g$ =8.00; the dashed blue curve is the model profile for $T_{\rm eff}$ =45000 K, $\log g$ =8.00.

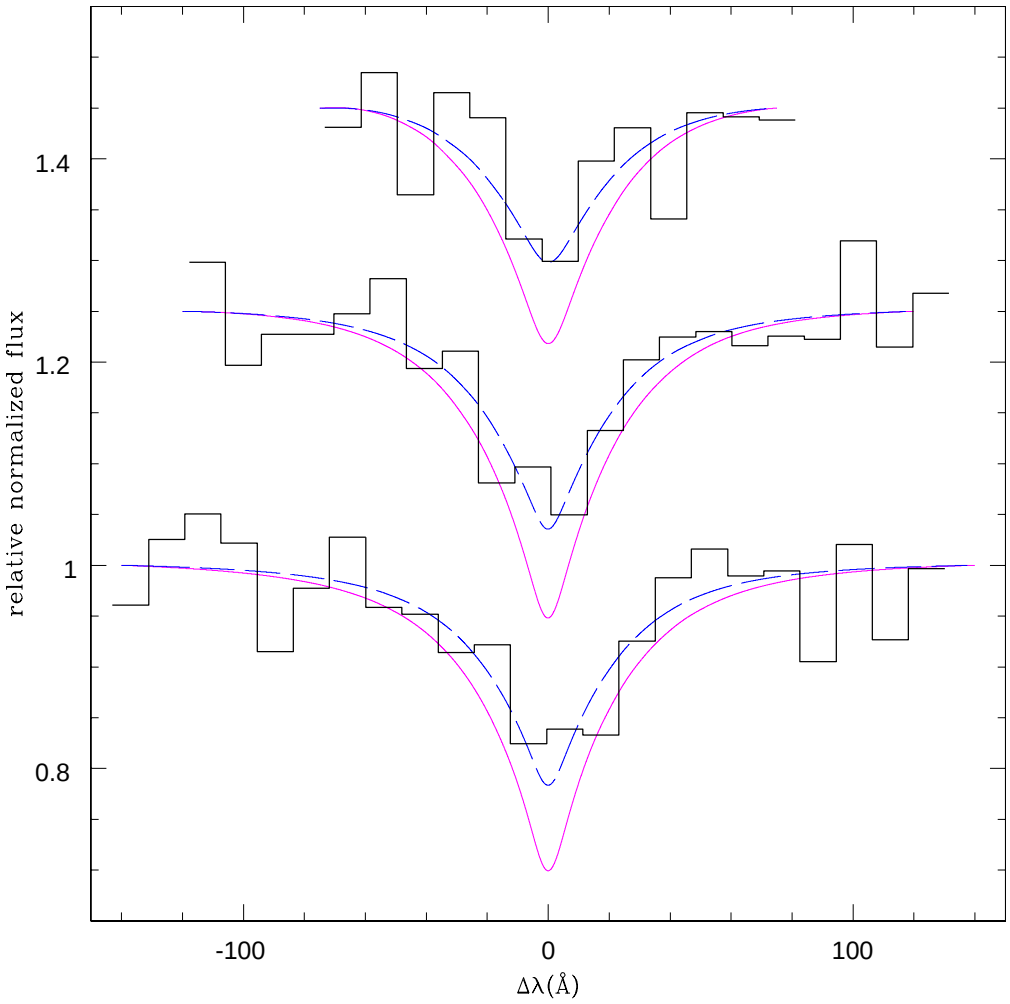

Figure 4.24: Same as in Fig. 4.14, except for NGC 6633 WB 15.

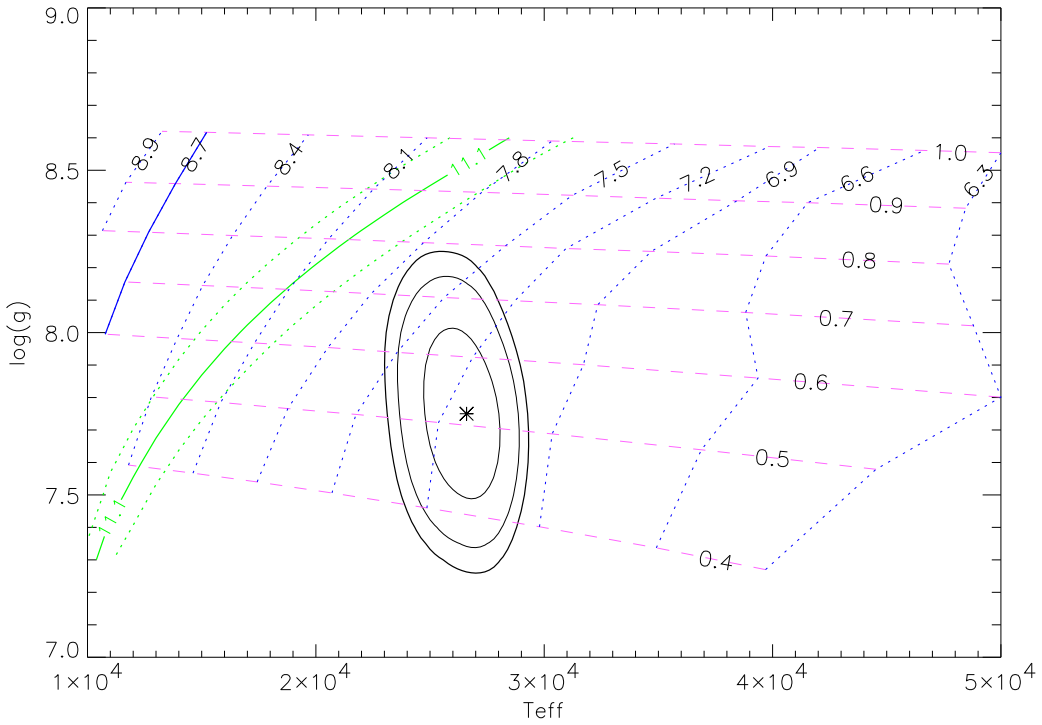

Figure 4.25: Plot of Balmer-line profiles for NGC 6633 WB 15. Black histogram is observed spectrum. The magenta curve is the model for $T_{\rm eff}$ =26000 K and $\log g$ =7.75; the dashed blue curve is the model profile for $T_{\rm eff}$ =28000 K, $\log g$ =7.75.

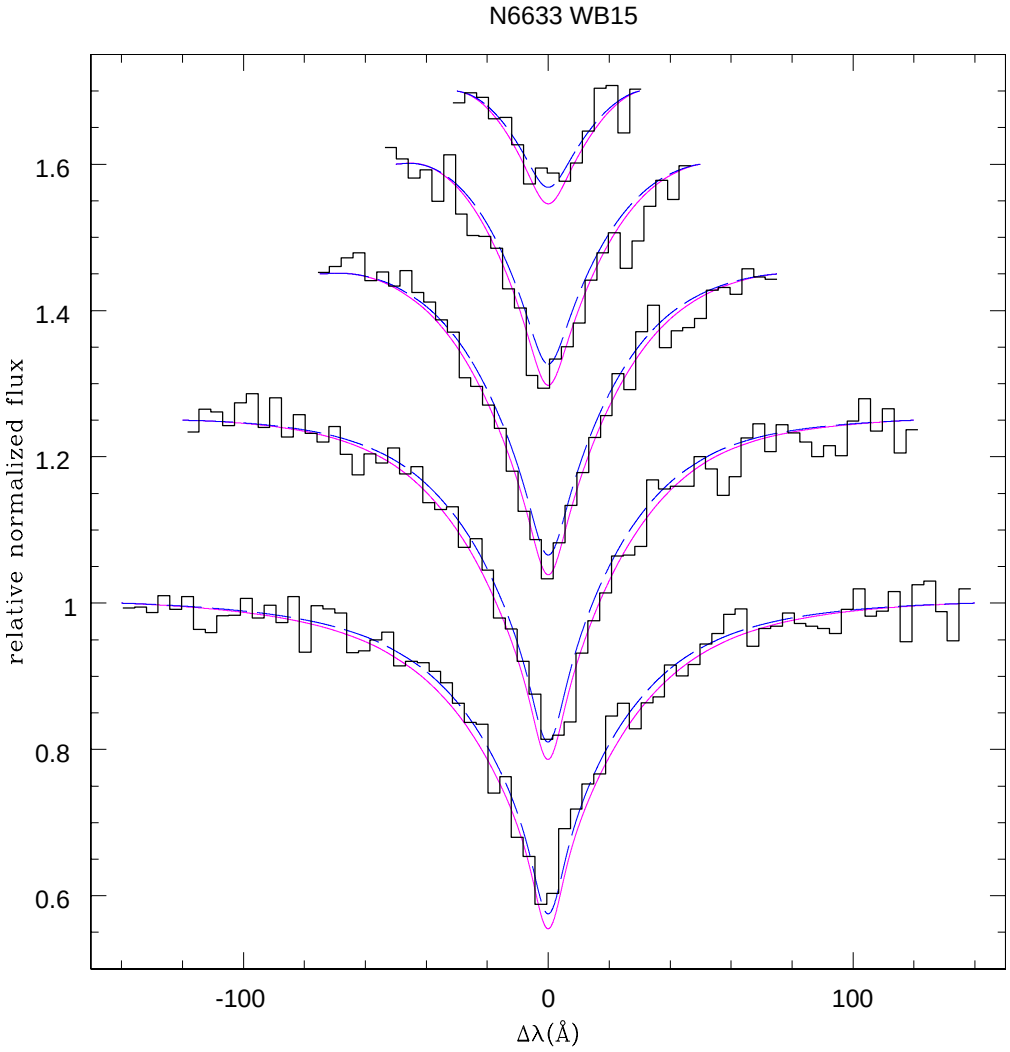

Figure 4.26: Same as in Fig. 4.14, except for NGC 6633 WB 27.

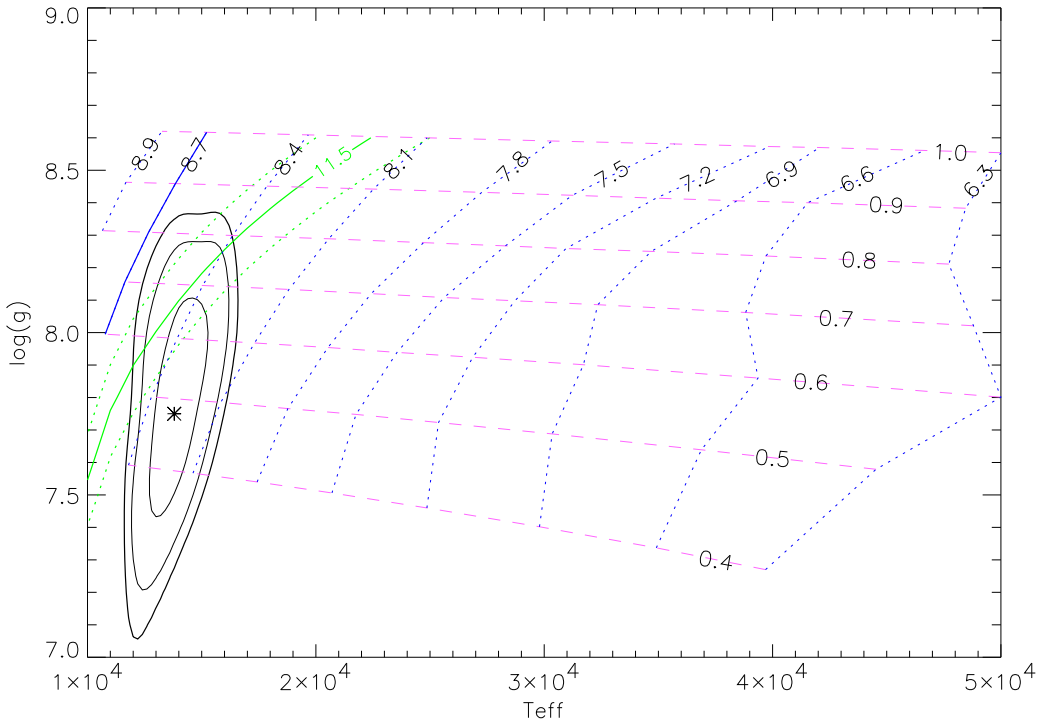

Figure 4.27: Plot of Balmer-line profiles for NGC 6633 WB 27. Black histogram is observed spectrum. The magenta curve is the model for $T_{\rm eff}$ =13000 K and $\log g$ =7.75; the dashed blue curve is the model profile for $T_{\rm eff}$ =16000 K, $\log g$ =8.25

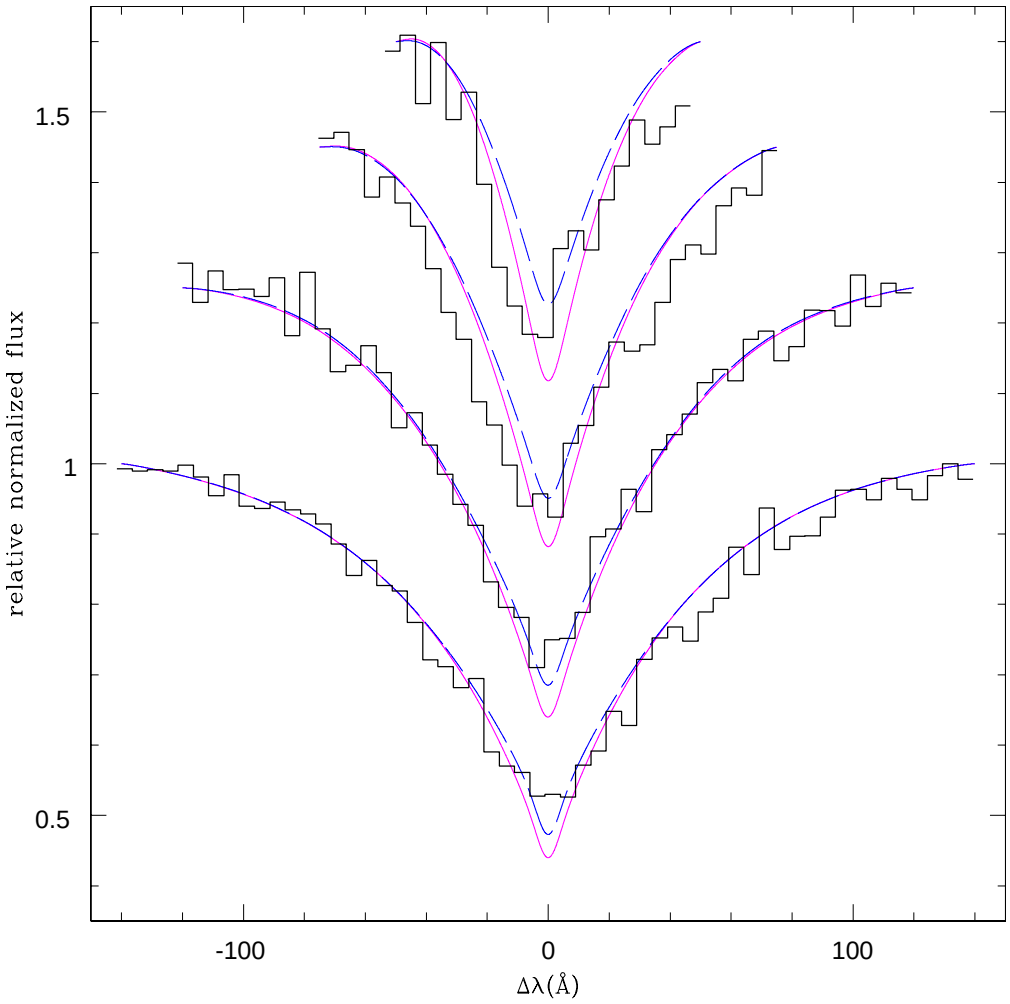

Figure 4.28: Spectra of WD candidates in NGC 7063. Spectra have been normalized and offset by arbitrary amounts.

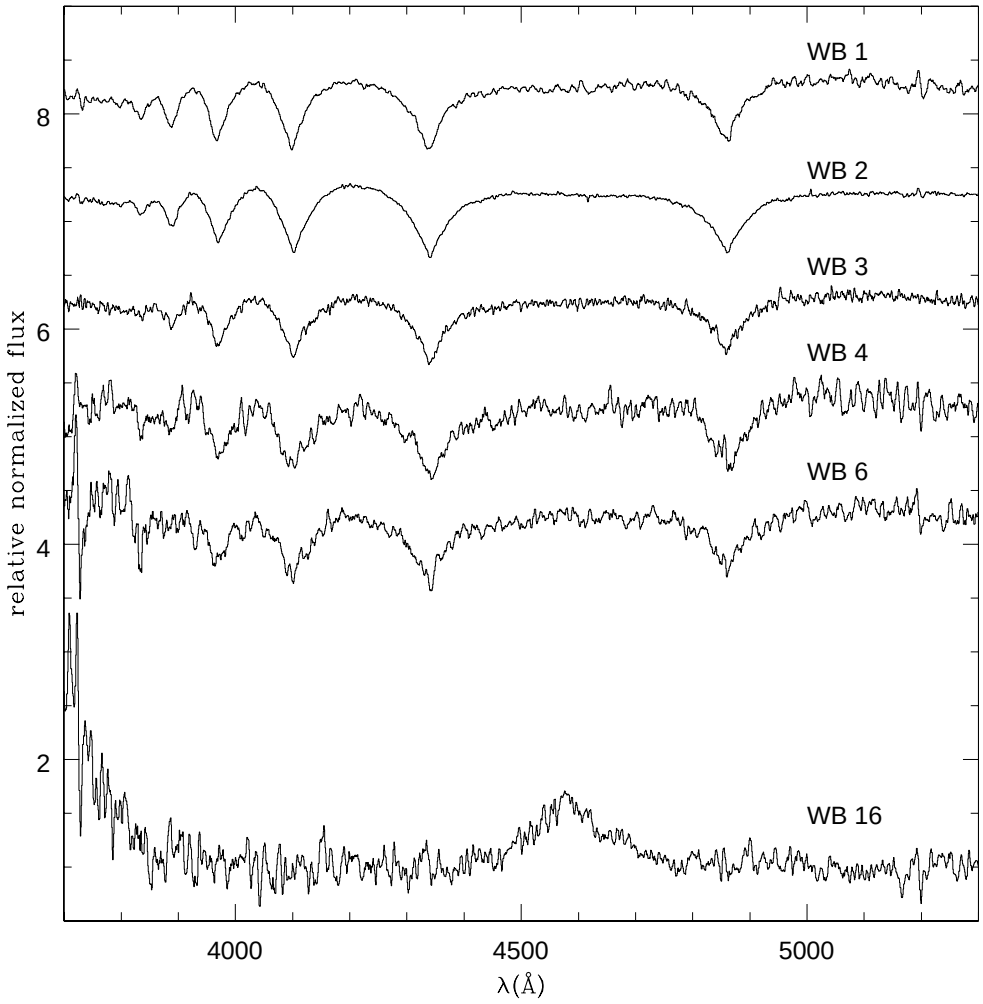

Figure 4.29: Same as in Fig. 4.14, except for NGC 7063 WB 1.

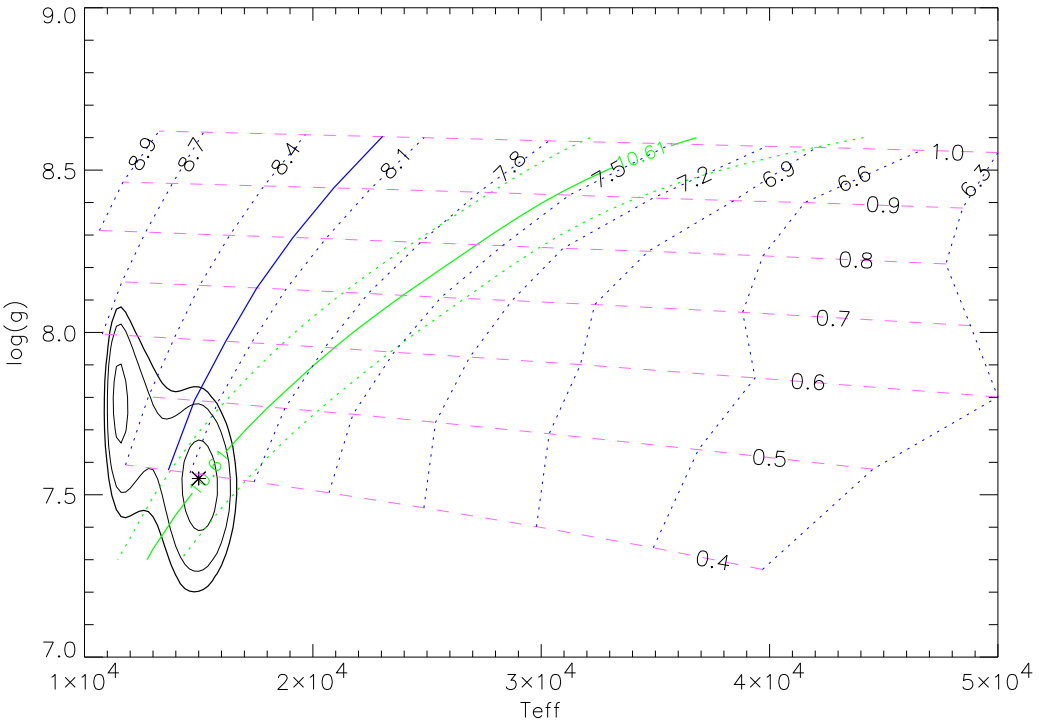

Figure 4.30: Plot of Balmer-line profiles for NGC 7063 WB 1. Black histogram is observed spectrum. The magenta curve is the model for $T_{\rm eff}$ =13000 K and $\log g$ =7.75; the dashed blue curve is the model profile for $T_{\rm eff}$ =16000 K, $\log g$ =8.25

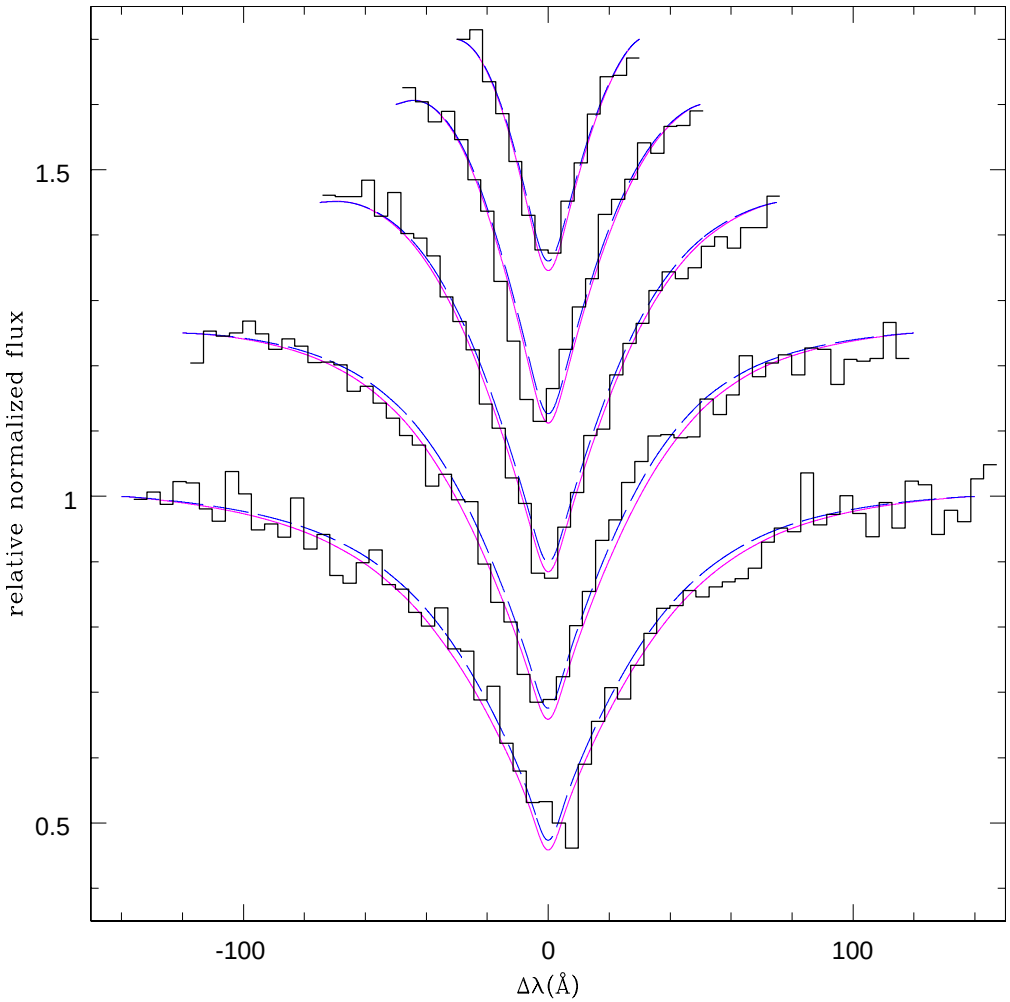

Figure 4.31: Same as in Fig. 4.14, except for NGC 7063 WB 2.

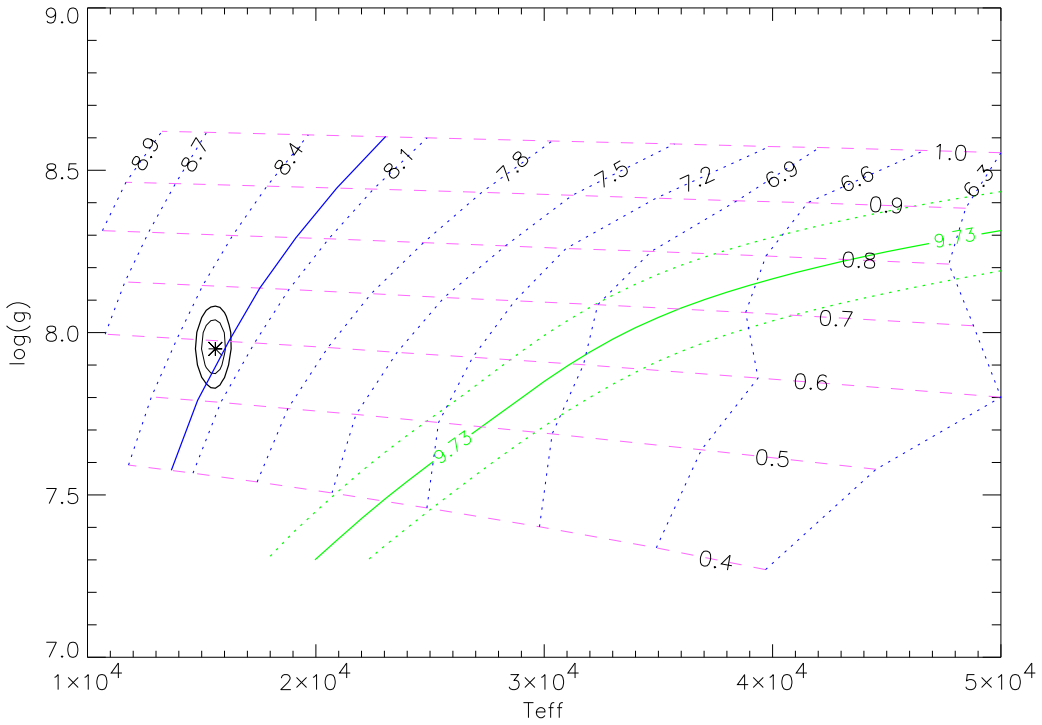

Figure 4.32: Plot of Balmer-line profiles for NGC 7063 WB 2. Black histogram is observed spectrum. The magenta curve is the model for $T_{\rm eff}$ =13000 K and $\log g$ =7.75; the dashed blue curve is the model profile for $T_{\rm eff}$ =16000 K, $\log g$ =8.25

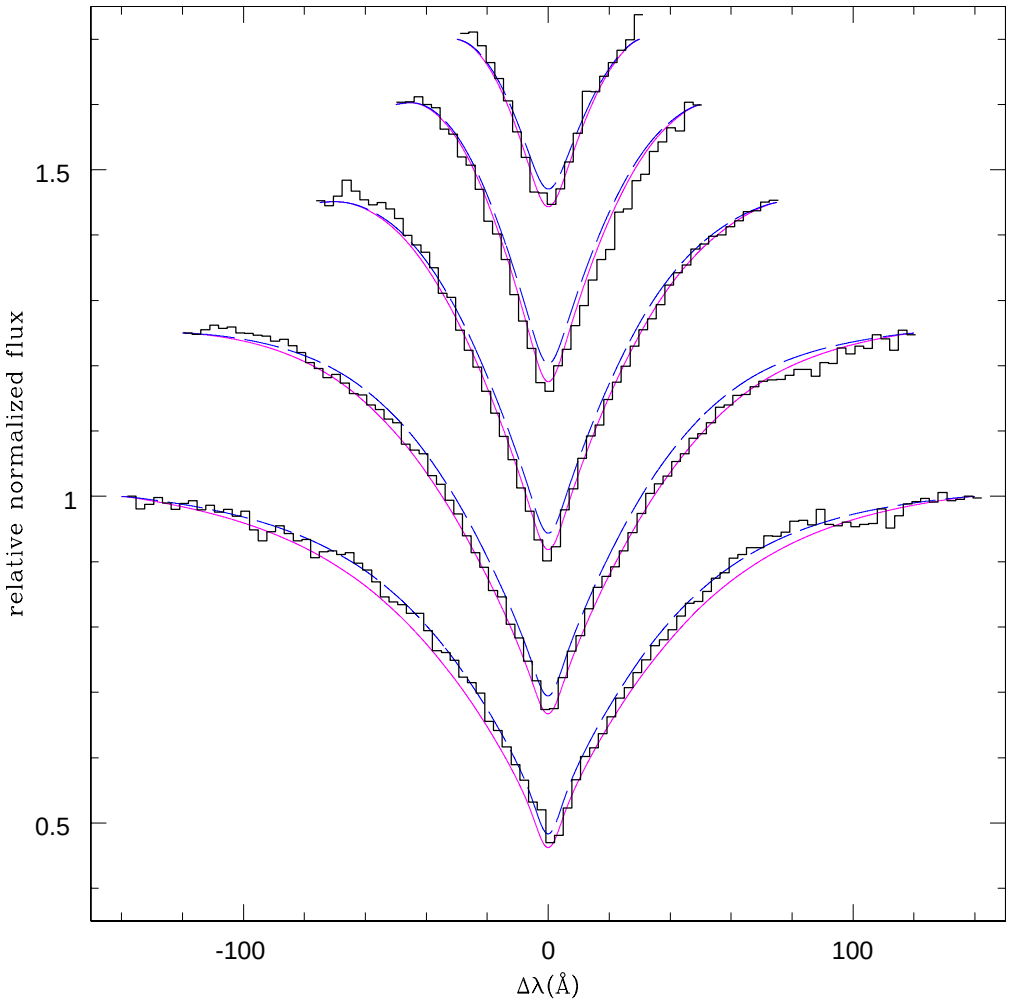

Figure 4.33: Same as in Fig. 4.14, except for NGC 7063 WB 3.

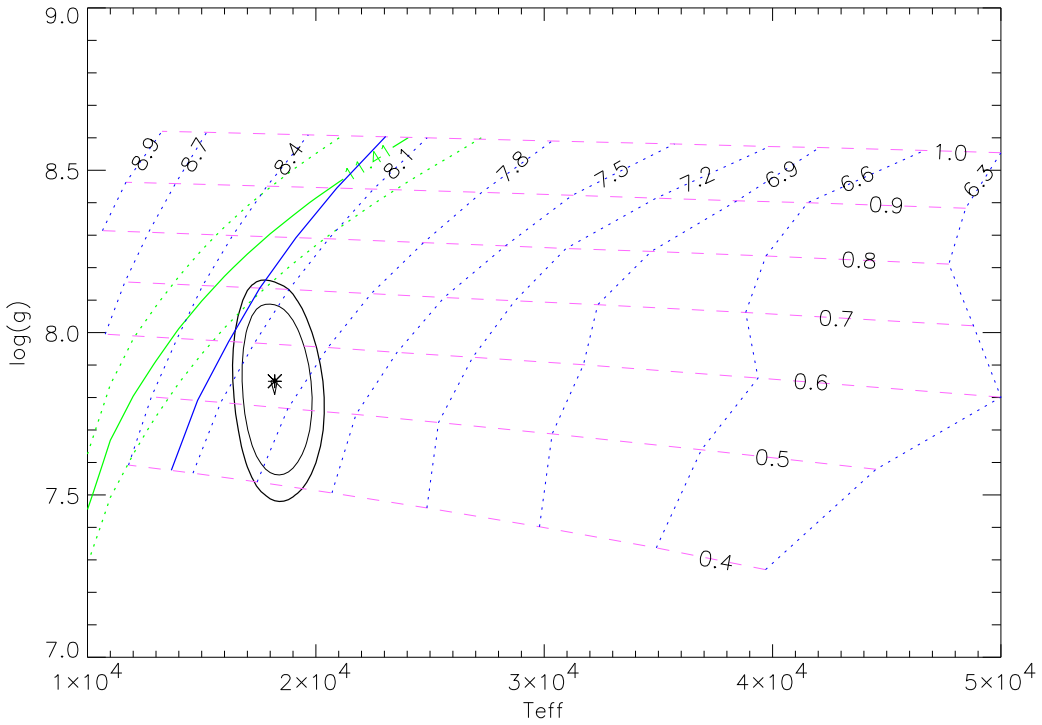

Figure 4.34: Plot of Balmer-line profiles for NGC 7063 WB 3. Black histogram is observed spectrum. The magenta curve is the model for $T_{\rm eff}$ =18000 K and $\log g$ =7.75; the dashed blue curve is the model profile for $T_{\rm eff}$ =20000 K, $\log g$ =7.75

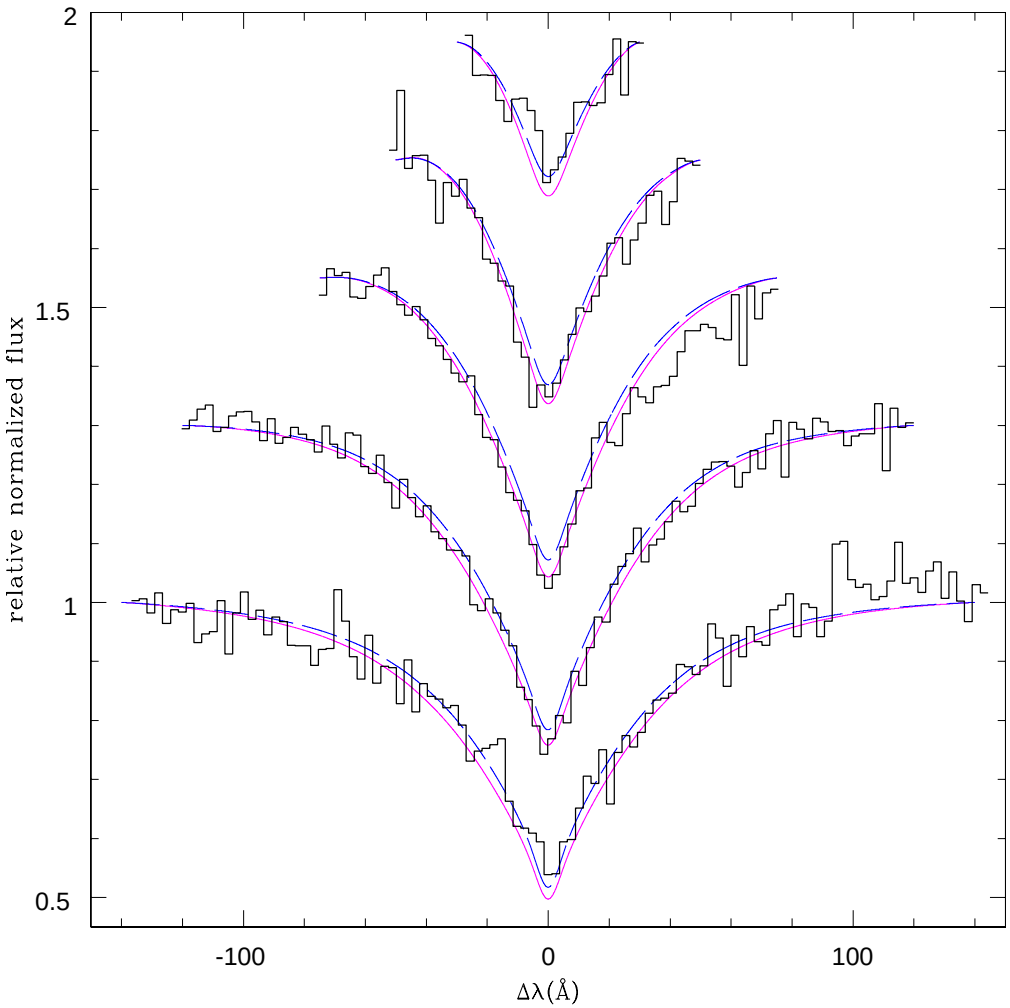

Figure 4.35: Same as in Fig. 4.14, except for NGC 7063 WB 4.

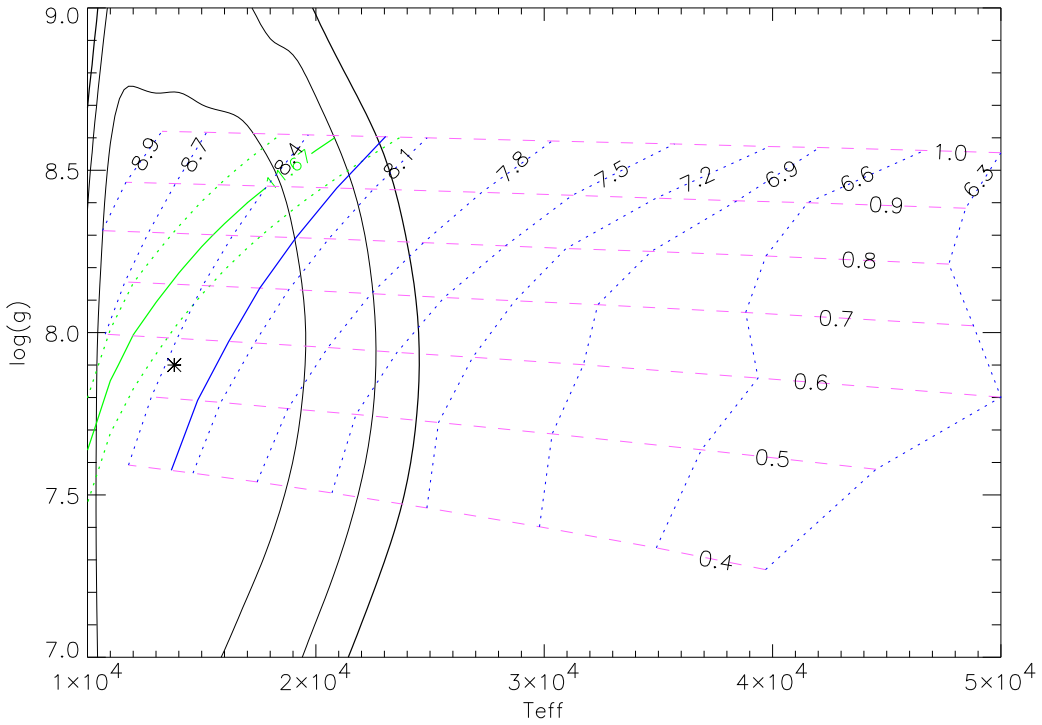

Figure 4.36: Plot of Balmer-line profiles for NGC 7063 WB 4. Black histogram is observed spectrum. The magenta curve is the model for $T_{\rm eff}$ =13000 K and $\log g$ =8.00; the dashed blue curve is the model profile for $T_{\rm eff}$ =18000 K, $\log g$ =8.00

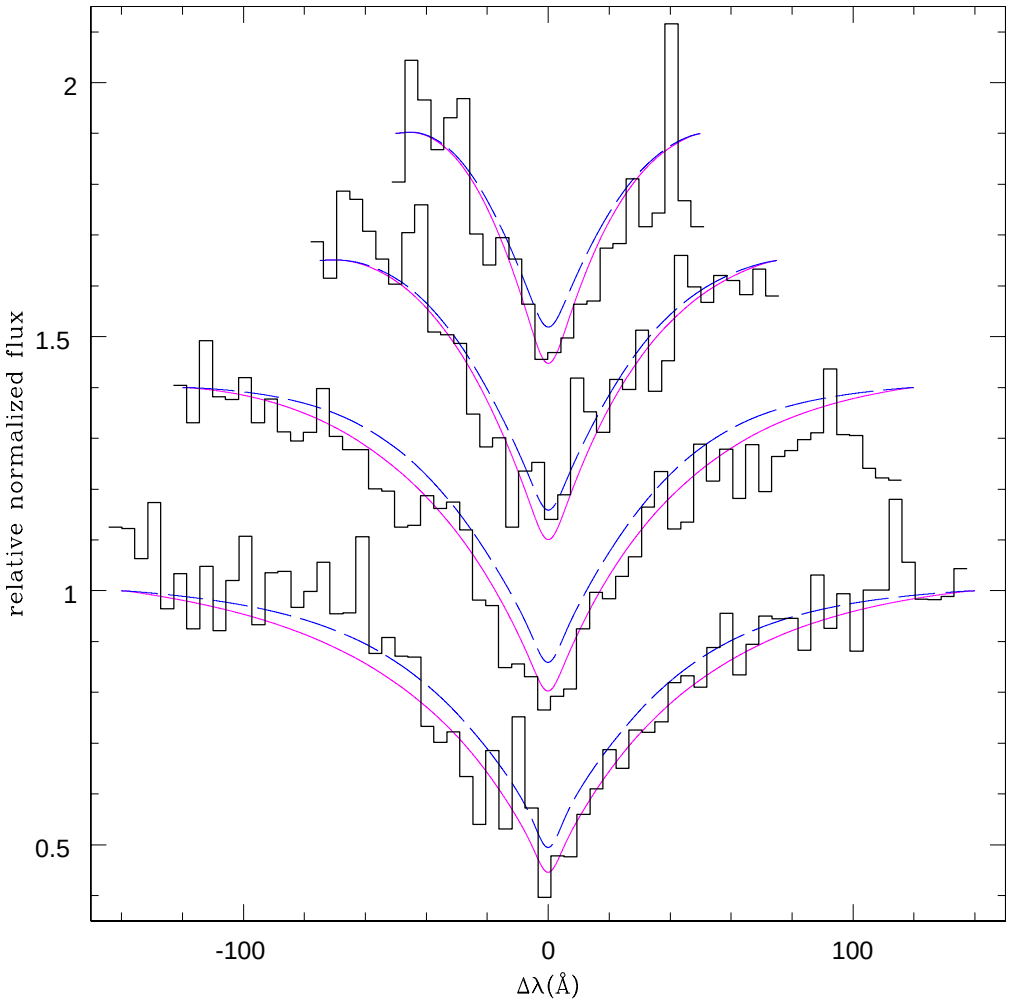

Figure 4.37: Same as in Fig. 4.14, except for NGC 7063 WB 6.

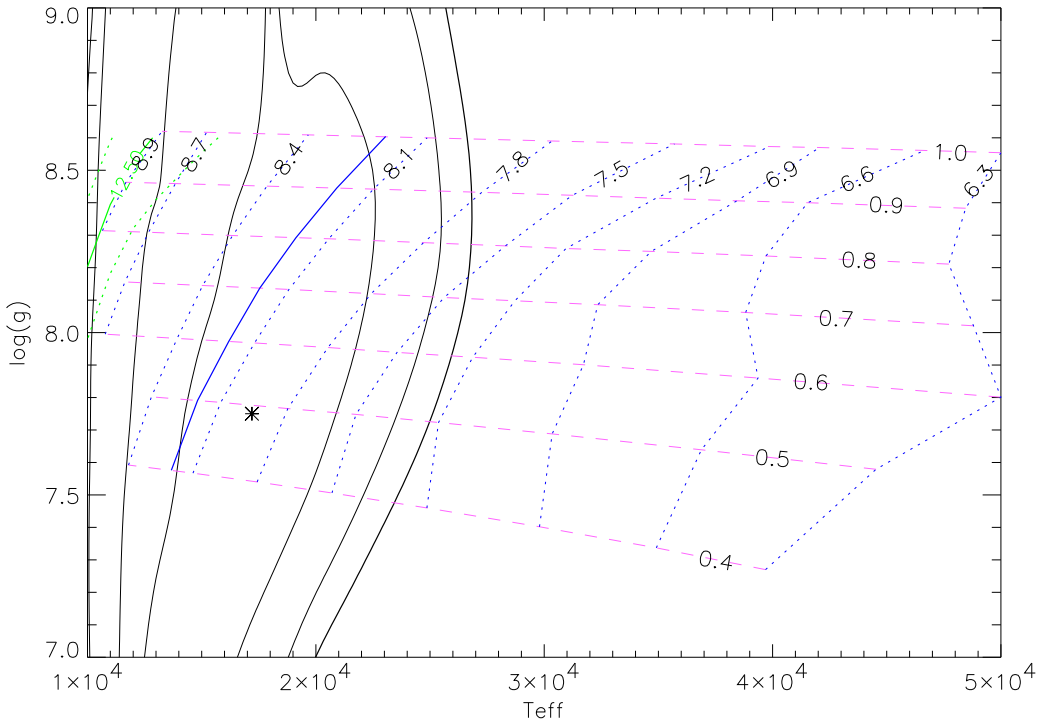

Figure 4.38: Plot of Balmer-line profiles for NGC 7063 WB 6. Black histogram is observed spectrum. The magenta curve is the model for $T_{\rm eff}$ =17000 K and $\log g$ =7.75; the dashed blue curve is the model profile for $T_{\rm eff}$ =24000 K, $\log g$ =8.25

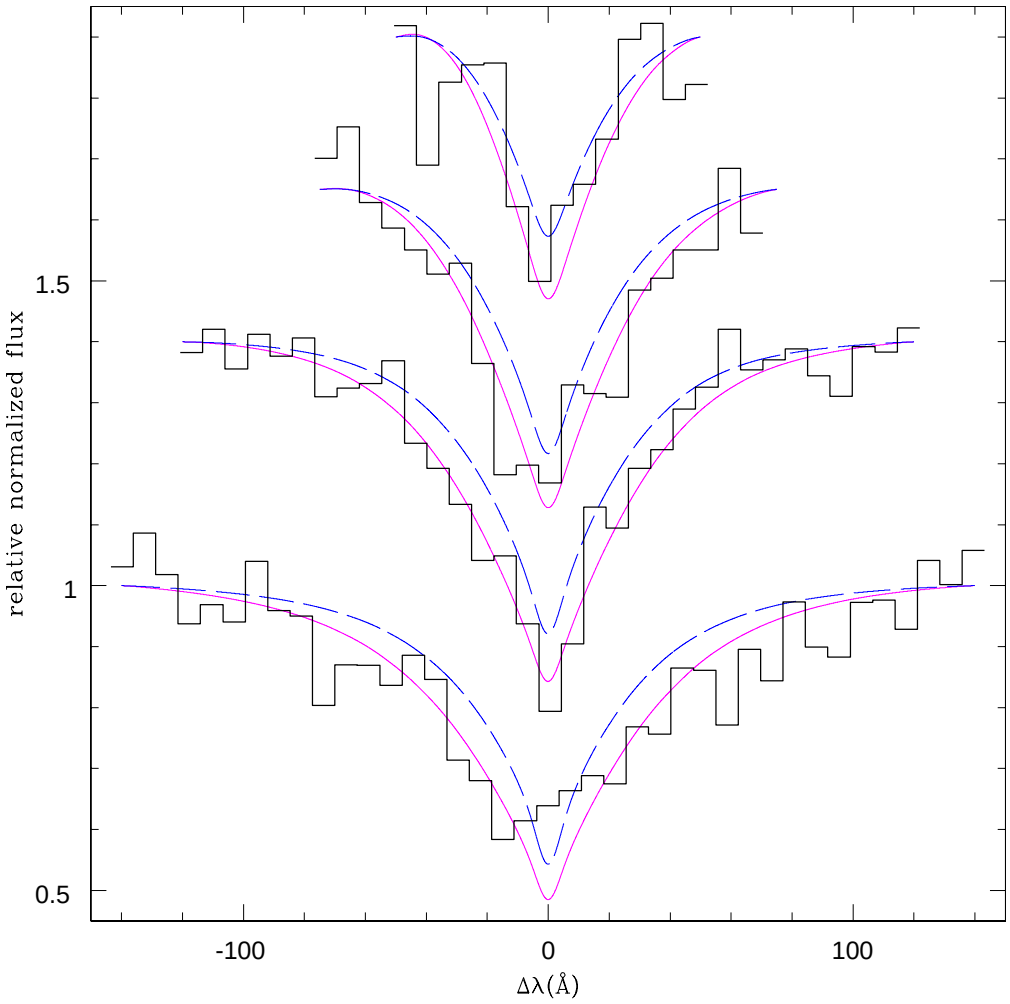

Chapter 5

Analysis & Discussion

5.1 The initial-final mass relation

5.1.1 Final mass

Of fourteen DA WDs with spectral data in four open clusters, four WDs are potential cluster members based on the combination of photometry with the spectral data – NGC 1039 WB 2, NGC 6633 WB 8, NGC 6633 WB 27, and NGC 7063 WB 1. If these cluster WDs are indeed cluster members, the photometric data can be used to constrain the WD parameters more tightly. For example, as seen in Fig. 4.18, the constraints on $\log g$ and $T_{\rm eff}$ for NGC 6633 WB 8 are fairly loose. However, if NGC 6633 WB 8 is a cluster member, its photometry and the cluster distance modulus constrain $T_{\rm eff}$ and $\log g$ to lie in the region defined by the green curves in the figure. The intersection of those curves with the confidence contours define the region of $\log g$-$T_{\rm eff}$ space in which the cluster white dwarf lies.

The mass and cooling ages for each likely cluster WD were re-determined to include only those values within the region of intersection of the 90% confidence contour with the $\pm 2\sigma$ photometry errors. These values are tabulated in Tab. 5.1. The stated value for M_{WD} and the cooling age are for the point of the best χ^2 fit along the line defined by the best photometry (solid green line in Fig. 4.18), and the stated error bars are the extremae in each value in the region of intersection.

5.1.2 Initial mass

The cooling age of each WD is the length of time the WD has been cooling since the planetary nebula phase of the progenitor star.[1] The lifetime of the progenitor star from zero-age main sequence (ZAMS) to the planetary nebula phase is therefore the current cluster age minus the WD cooling age.

The lifetime of the progenitor star, defined as the time spent between arrival on the ZAMS and the thermal pulsing on the AGB, was determined from the evolutionary tracks summarized in Girardi et al. (2002). Subtraction of the WD cooling age from the cluster age gives the lifetime of the progenitor star. The progenitor mass is then determined by interpolation from the tabulated stellar lifetimes. The interpolation routine is accurate to $0.01 M_{\odot}$ for progenitor masses $M_{\rm ZAMS} \lesssim 8 M_{\odot}$ but less reliable for higher masses.

Tab. 5.1 gives the initial ZAMS progenitor mass of each cluster WD for four stellar evolutionary models: $Z = 0.008$, $Z = 0.019$, and $Z = 0.030$ for solar-scaled abundances with moderate convective overshoot, and $Z = 0.019$ without convective overshoot. The initial masses are calculated at various cluster ages spanning the range of values discussed in §3.4.2. The results indicate that the calculated initial mass is highly sensitive to the cluster age, and the sensitivity increases dramatically as the difference between the WD cooling age and the cluster age decreases (see §5.1.4).

5.1.3 The initial-final mass relation: new results

Figure 5.1 displays the initial-final mass data along with the "revised" initial-final mass relation of Weidemann (2000), and the core masses at the first thermal pulse and at the end of the evolutionary models, both from Girardi et al. (Girardi et al., 2000). Also given are initial-final mass points from previously-published studies of the Praesepe, Hyades, and Pleiades clusters (Claver et al., 2001), re-determined from the published $T_{\rm eff}$ and $\log g$ with the current models. The current initial masses for the Praesepe and Hyades WDs are systematically lower than those in Claver et al. (2001) due to their use of pure ^{12}C WD cooling models, and our use of C/O core cooling models.[2] These differences are most pronounced for the most massive WDs ($\Delta M_{WD} = 0.3 M_{\odot}$ for WD 0836+199) and are negligible for the youngest WDs ($\Delta M_{WD} = 0.01 M_{\odot}$ for WD 0438+108).

Within the stated errors and age uncertainties, both NGC 6633 member WDs lie within the previously-published initial-final mass relation. The NGC 7063 member is

[1] While there may be some uncertainty in defining exactly when the cooling time is zero, these uncertainties are on the order of 3×10^4 yr, which is much smaller than the WD ages of 10^{7-8} yr.

[2] C/O cores cool more quickly than pure carbon cores because the heat capacity per gram of oxygen is less than that of carbon, the net result being lower initial masses for the C/O cores.

a distant outlier, but this is readily explained by its potential He-core.

NGC 1039 WB 2 is a confusing case. Based on Fig. 4.10, the WD appears to be a cluster member, yet its position in the initial-final mass relation conflicts with the previous measurements. There are three possible explanations for this. The WD could be a hot field WD currently wandering through the star cluster. The candidate was selected by Anthony-Twarog (1982) in a study of ~ 1600 sq. arcminutes centered on M34. Based on Fig. 4.10, it is assumed that NGC 1039 WB 2 lies within 0.1 mags of the de-reddened cluster distance modulus of 8.38, or at a distance of $474 \pm 22\,\mathrm{pc}$. The volume enclosed by this region is calculated to be $\sim 1340\,\mathrm{pc}^3$. The space density of WDs with $M_V \leq 11 \approx 10^{-4}\,\mathrm{pc}^{-3}$ (Boyle, 1989), so the likelihood that at least one hot WD resides in the surveyed field at the cluster distance is ~ 0.134. It therefore cannot be ruled out that NGC 1039 WB 1 is not a cluster member. Improved studies of the cluster distance modulus and reddening will help to test this explanation.

If NGC 1039 WB 1 is a cluster member, then two possible explanations for the discrepancy with the initial-final mass relation remain. One is that the age of the cluster may be incorrect. In order to bring the upper error bar into agreement with the empirical initial-final mass relation, the logarithmic age of the cluster would need to be greater than ~ 8.6, in significant conflict with currently-published values.

The other explanation would be that this WD was in an interacting binary system and has an abnormally low mass, i.e. NGC 1039 is another He-core WD. According to Bragaglia, Renzini, & Bergeron (1995), the fraction of He-core WDs in the field is ~ 0.1. Assuming this fraction is similar in open clusters, the probability that two or more He-core WDs would be found in a sample of four WDs is $P \approx 0.06$. This probability assumes that the fraction of He-core WDs in open clusters is the same as the fraction in the field, which need not be the case.

5.1.4 The initial-final mass relation and M_w

While the four new WDs do not provide any unique insight into the initial-final mass relation at this point, the analysis raises some interesting points in regard to high-mass WD progenitors. Numerous discussions on the initial-final mass relation have focused on the high-mass end of the relation as an indication of the value of M_w. This discussion is based on white dwarfs in two open clusters, NGC 2516 and the Pleiades.

NGC 2516 is a rich, slightly subsolar-metallicity cluster in the southern hemisphere. Its logarithmic age is 8.2 ± 0.1 (Sung et al., 2002); the cluster age used in Koester & Reimers (1996) is 8.15 ± 0.1. Table 5.2 contains the final and initial masses calculated for each WD at various assumed cluster ages. It is clearly seen that the lower limit to M_w derived from the data is extremely sensitive to the assumed cluster

age. For the Sung et al. (2002) age of 8.2, $M_w \geq 6.34 M_\odot$. If the cluster age is actually 8.3, that lower limit is reduced to $5.70 M_\odot$.

The other WD commonly used to constrain M_w is LB 1497, a hot, high-mass WD located $\sim 86'$ from the center of the Pleiades cluster. Based on its proper motion, LB 1497 has a 79% likelihood of membership (Schilbach et al., 1995), and is located well within the projected tidal radius of the cluster, $r_t \approx 440' \approx 16$ pc (Raboud & Mermilliod, 1998). The measured mass for the Pleiad WD is $1.091 \pm 0.021 M_\odot$ from spectroscopic Balmer line fits (Claver et al., 2001), $0.98^{+0.18}_{-0.16} M_\odot$ from gravitational redshift and an assumed distance modulus of 5.54 ± 0.06 (Wegner et al., 1991), $1.02^{+0.04}_{-0.05} M_\odot$ from gravitational redshift and a Hamada-Salpeter mass-radius relation (Wegner et al., 1991), and $1.025 \pm 0.017 M_\odot$ based on the photometry and an assumed distance modulus of 5.60 (Claver et al., 2001).[3]

Due to coarse grid spacing at high $T_{\rm eff}$ and $\log g$, it is not possible to determine $\log g$ and $T_{\rm eff}$ from the LRIS observations of the Pleiad at this time. Previously-published values of $T_{\rm eff}$ and $\log g$ are available, but as the mass of the Pleiad WD is $\gtrsim 1 M_\odot$ and the W95 models only extend to $1 M_\odot$, the resulting cooling ages require extrapolation and are therefore suspect. If the cooling time is extrapolated from the Balmer-line fit parameters of Claver et al. (2001) and the W95 models, the logarithmic cooling age is 7.90 for a (rederived) WD mass of $1.16 M_\odot$; Claver et al. derive $M_{WD} = 1.091 M_\odot$ and a cooling age of 7.98 (for a pure ^{12}C core). For a lower WD mass of $1 M_\odot$ WD with $T_{\rm eff} = 31660$ and $\log g = 8.60$ (Claver et al., 2001), the logarithmic cooling age is 7.74.

The initial mass of LB 1497 can be determined once the age of the Pleiades is known. Work by Pinsonneault et al. (Pinsonneault et al., 1998) finds an logarithmic age of 8.0 (without stated error bars) for the Pleiades. Lithium depletion studies of the Pleiades suggest a slightly older age of 8.05 (Basri et al., 1996) to 8.1 (Stauffer et al., 1998). Dias et al. (Dias et al., 2002) states a logarithmic age of 8.131. The resulting final masses assuming these ages are given in Tab. 5.3.

To further illustrate the effects of errors in the cluster age upon the derived initial-final mass relation, the initial masses of WDs in the Hyades and Praesepe have been calculated for a range of ages consistent with the logarithmic age of these clusters stated in Claver et al. (2001), 8.80 ± 0.05. The initial masses of the Hyades and Praesepe WDs have been calculated for ages in this range and are also presented in Tab. 5.4.

Based on the quantities plotted in Fig. 5.1, the argument has been made that the empirical initial-final mass relation more closely follows the relation of initial mass

[3]Evidence is very strong that the *Hipparcos* distance modulus to the Pleiades of 5.33 is incorrect due to systematic errors (Narayanan & Gould, 1999), so no analysis or discussion is presented using the *Hipparcos* distance.

to the core mass at the first thermal pulse (dashed line) as opposed to the theoretical initial-final mass relation of Girardi et al. (2000) (solid line). However, if the logarithmic age of NGC 2516 is 8.30 (the upper end of the stated errors on the cluster age), the resulting initial-final mass relation is closer to the theoretical initial-final mass relation than the core mass at the first thermal pulse, as shown in Fig. 5.2.

The Pleiad WD, shown in Fig. 5.2 for assumed Pleiades ages of 8.00, 8.05, and 8.15 and a WD mass of $1.0 M_{\odot}$, remains the tightest constraint on the upper end of the initial-final mass relationship and M_w. Because of the uncertainties surrounding the cooling age of the Pleiad WD and the cluster age, we find $M_w \gtrsim 6 M_{\odot}$, a more conservative lower limit than the $M_w \geq 7.0 M_{\odot}$ advanced by Claver et al. (Claver et al., 2001).

The generic effect of uncertainty in the age of an open cluster on the progenitor mass determination is shown in Fig. 5.3. The figure shows the *derived* progenitor mass for WDs with actual progenitor masses of $6 M_{\odot}$, $7 M_{\odot}$, and $8 M_{\odot}$ based on assumed errors in the observationally-derived logarithmic cluster ages of $\pm 0.1\,\mathrm{dex}$. The figure assumes that the WD cooling age (the actual progenitor mass lifetime subtracted from the actual cluster age) is known precisely. From the plot, it is clear that for clusters older than a logarithmic age of 8.10, measurements of the initial mass are very poorly constrained if the errors in the measured cluster age are 0.1 dex. In order to study the high-mass end of the initial-final mass relation with any true accuracy, either cluster ages must be determined to a higher degree of accuracy, or younger clusters must be studied. The corollary of this is that values of M_w derived from the initial-final mass relation cannot be considered exceptionally valid unless the cluster age is known to high accuracy, which is not the case for either NGC 2516 or the Pleiades, or the cluster is younger than $\sim 10^8\,\mathrm{yr}$, which also is not the case for NGC 2516 or the Pleiades.

5.2 White dwarf populations and M_w

Another method for estimating M_w is based on the initial-mass function (IMF) and the number of observed WDs. Let the number of stars $\mathrm{d}N$ with masses in $(M, M + \mathrm{d}M)$ be given by

$$\mathrm{d}N = N\,\xi(M)\,\mathrm{d}M\,. \tag{5.1}$$

Then the number of stars N with masses between M_1 and M_2 is

$$N = N_0 \int_{M_1}^{M_2} \xi(M)\,\mathrm{d}M\,. \tag{5.2}$$

Supposing that the number of stars in a cluster in a magnitude range ($V_{\rm faint}, V_{\rm bright}$, N_*, is known, and that the mass of a star with magnitude V is $M(V)$. Then N_0 is

$$N_0 = \frac{N_*}{\int_{M(V_{\rm faint})}^{M(V_{\rm bright})} \xi(M)\,{\rm d}M}\,. \tag{5.3}$$

If the ZAMS mass of the most-evolved star remaining in the cluster is $M_{\rm AGB}$, then the number of WDs formed in the cluster N_{WD} is

$$N_{WD} = N_* \frac{\int_{M_{\rm AGB}}^{M_w} \xi(M)\,{\rm d}M}{\int_{M(V_{\rm faint})}^{M(V_{\rm bright})} \xi(M)\,{\rm d}M}\,. \tag{5.4}$$

If $\xi(M)$ and N_* are known, the error in N_{WD} is $\sqrt{N_{WD}}$. Therefore, given the number of cluster stars in a known mass range, it is possible to determine the number of expected WDs for various values of M_w, and compare these to the observed number of cluster member WDs.

5.2.1 Counting WDs

The combined photometry and spectroscopy available for several clusters permits the most accurate counts of member WDs. Figs. 5.4 - 5.7 show the final CMDs and, for NGC 7063, color-color plot, with spectroscopic results included. Though little spectroscopic work has been done, IC 4665 contains no confirmed WDs. Based on the cluster age, only a handful of viable candidates remain. NGC 6633 has been well-observed spectroscopically. Two WDs are likely members, and two viable WD candidates remain unobserved. In NGC 7063, only one member WD was found. One candidate with photometry similar to the He-core WD remains unobserved.

Two major sources of incompleteness dominate the WD samples. The first is photometric incompleteness, i.e. non-detection of WDs during the image processing, and binary star incompleteness, i.e. WDs hidden in unresolved binaries. Both of these are explored below.

Photometric Completeness

The photometric completeness of the sample was determined by artificial star tests. Artificial stars are created from the scaled PSF and inserted into random locations in each field. For PFCam fields, the magnitude distribution of artificial stars was drawn from a linear approximation to the $0.6 M_\odot$ WD cooling curve at each cluster's distance and reddening. Only 100 artificial stars were placed in the images in a single run to

prevent an increase in the crowding. The total number of runs were adjusted such that the expected error in the completeness,

$$\sigma_f \approx \sqrt{f(1-f)/n_{\rm add}}\,, \tag{5.5}$$

where f is the fraction of stars recovered and $n_{\rm add}$ is the number of stars added (Bolte, 1989), was $\lesssim 0.05$. Photometric analysis of the artificial star frames was identical to that in §3.4. The recovered artificial stars were required to have output photometry within 7σ of the input values.

The results from the PFCam artificial star tests for NGC 2168 and NGC 7063 are shown in Figs. 5.8 and 5.9. NGC 7063 is $\gtrsim 90\%$ complete for $V \lesssim 22$, one magnitude fainter than the faintest expected WD. NGC 2168 is less than 50% complete for $V \geq 21.5$, which corresponds to the faintest expected WD if the logarithmic age of NGC 2168 is 8.0. If NGC 2168 is older, such as the age of 8.3 published by Sung & Bessel (1999), the photometry is not deep enough to reach the faintest WD candidates. The resulting white dwarf luminosity function for NGC 2168, corrected for completeness, is given in Tab. 5.5 and shown in Fig. 5.10.

For the CFHT images of NGC 6633, 1000 artificial stars were inserted in each of two artificial star runs. As the faint limit of the WD candidate selection was well above the photometric limit, artificial stars in a single magnitude range of $21.25 \geq V \geq 20.75$ and $B-V = 0.4$ were used to determine completeness. The completeness for NGC 6633 was determined to be $f = 0.919 \pm 0.009$.

WDs in unresolved binaries

Multiple-star systems with an evolved member are known to survive the planetary nebula phase, with Sirius being a prime example. WDs in a binary with a low-mass ($\lesssim 0.3 M_\odot$) are still recovered by photometric selection, as the WD is significantly more luminous than the companion at optical wavelengths. WDs in a binary system with companions of equal or brighter luminosity are unlikely to be recovered, as the combined spectral-energy distribution does not meet the color selection criteria applied to find WD candidates.

In order to determine the incompleteness due to binary systems, a Monte Carlo simulation was developed. The simulation draws stars randomly from a user-selected IMF. If a star has a mass higher than the MSTO, the star is assumed to have formed an invisible stellar remnant if the ZAMS mass is greater than M_w. Otherwise, the star is assumed to have formed a WD. The resultant WD mass is taken from the "revised" initial-final mass relation of Weidemann (2000).

If the star has evolved into a WD, its photometric indices are determined from the WD cooling models, the WD mass, and cooling age of the WD, determined by

subtracting the progenitor lifetime from the cluster age. If the star has not evolved into a WD or invisible remnant, its photometry is determined from the ZAMS of Girardi et al. (2002).

The binary fraction in the simulation is the fraction of observed point sources which are actually unresolved binaries. Companion stars are assigned to each simulated star with a probability equal to the binary fraction. The mass of the companion star is again drawn from the input IMF. Binary system photometry is determined by summing the light from the companion stars.

To simplify the simulation, the ZAMS photometry of each star was used. The output simulated clusters therefore have no main-sequence turnoff or red giant branch. This has no impact on the number of recovered WDs. Both the evolved and ZAMS stars in the studied mass ranges are far more luminous than WDs, and the WDs is not be detected in either case.

Stars continue to be drawn in this manner until the number of simulated star systems within a given magnitude range equals the number of observed stars in the magnitude range. The selection criteria used in §3.4.3 are then applied to the data to recover WDs. Ten thousand simulations are run for each set of input parameters to provide robust statistical measurements of the numbers of WDs and observed WDs, even for sparse stellar systems. An example of the output from the simulation is shown in Figs. 5.13 and 5.14.

Three IMFs of the form $\xi(M) = M^{-(1+\alpha)}$ were used in the simulations: a Salpeter IMF ($\alpha = 1.35$) (Salpeter, 1955), a steeper power law ($\alpha = 2$), and a broken power law ($\alpha = 1.6$ for $M > 1M_{\odot}$ and $\alpha = -0.2$ for $M \leq 1M_{\odot}$). The steeper power law is obtained from the Salpeter IMF when unresolved binaries are accounted for (Naylor et al., 2002). Broken power laws are commonly quoted as fitting the observed mass functions of open clusters (Naylor et al., 2002; Meusinger et al., 1996; Barrado y Navascués et al., 2001), and the selected form approximates the mass function of NGC 2168 (Barrado y Navascués et al., 2001).

For the simulated clusters in this project, the Salpeter IMF results in more WDs than the other IMFs due to its lesser slope at high-masses. The broken power law results in few WDs in binary systems being recovered, as the flat low-end mass function increases the typical WD companion mass and luminosity.

The clusters NGC 2168, NGC 6633, and NGC 7063 were modeled using this simulation. Results of each cluster follow:

NGC 7063. — For NGC 7063, a cluster age of 8.15 was used. The PFCam field contains 19 member stars with $V \leq 13.5$. Membership criteria are based on proper motion membership ($P \geq 0.7$) when available or photometry consistent with cluster membership when proper motion data is ambiguous ($0.7 \geq P \geq 0.4$) or unavailable. Each simulation proceeded until 19 stars with $V \leq 13.5$ and lifetimes longer than a

logarithmic age of 8.15 were drawn. Because of the cluster sparseness, the average number of WDs in the cluster was low, 1.9 ± 1.4 for a Salpeter IMF with $M_w = 8M_\odot$ and 1.0 ± 1.0 WDs for a Salpeter IMF with $M_w = 6M_\odot$. Both of these numbers are consistent with the one WD discovered. Variations in the IMF and binary fraction resulted in only fractional changes to these numbers and did not provide any additional insight.

NGC 6633. — Based on the proper motion study of Sanders (1973), there are 45 likely proper motion members ($P \geq 50\%$) with $V \leq 12$ in the CFHT field. The resulting numbers of WDs from the Monte Carlo simulation for a cluster age of 8.675 are given in Tab. 5.6. Based on the spectroscopic results of two confirmed member WDs and two more viable WD candidates, the existence of up to four cluster member WDs can be assumed. Four or fewer WDs is in mild conflict with the results for a Salpeter IMF; the $\alpha = 2$ power law and broken power laws are in better agreement with the number of observed WDs, especially if the binary fraction is $\gtrsim 0.5$. The difference in expected numbers of WDs based on differing values of M_w is too small to be explored with this cluster.

NGC 2168. — The imaged fields in NGC 2168 contain thirty-six stars brighter than $V = 13$. In these fields, four WD candidates were observed, 6.9 after the completeness correction. Tab. 5.7 contains the results of the simulation for the cluster for two different assumed cluster ages of 8.0 and 8.3. Because of the small number of WDs resulting from the simulations, only results for a binary fraction of 0.5 are shown for the age of 8.0; simulations with differing binary fractions produced negligible changes in the results.

Based on the simulations, if NGC 2168 has the younger age of 8.0, and if all four of the WD candidates are cluster WDs, then the cluster has a near-Salpeter IMF and $M_w \approx 8M_\odot$. Given that the cluster mass function has been found to likely be steeper than Salpeter (Barrado y Navascués et al., 2001) and that field WDs likely contaminate the sample, this seems unlikely. If the cluster has an age of 8.0 but only one or two of the candidates are cluster members, then it is not possible to rule out any of the tested models. If the cluster age has the older value of 8.3, then it is difficult to draw any conclusions about M_w, the IMF, or the binary fraction.

Hyades and Praesepe. — This simulation is also run in a cursory exploration of the lack of WDs in the Hyades and Praesepe cluster. According to Weidemann et al. (1992), the Hyades is "missing" 21 WDs, i.e. the IMF would suggest 29 WDs in the Hyades, yet only seven Hyades member WDs are known. A selection on Hyades members in WEBDA resulted in 89 Hyades members brighter than $V = 7.5$. The resulting simulations, using the broken-power-law IMF, contain an average of 27 WDs in the Hyades for $M_w = 8M_\odot$, close to the twenty-nine WDs Weidiemann et al. calculated. For a binary fraction of 0.5, on average 17.8 ± 4.5 WDs are in binaries. A

purely photometric survey would recover, on average, 12.3 ± 3.7 WDs, 3.2 ± 1.8 of which would be in binary systems. If $M_w = 6M_\odot$, the number of total WDs averages 23.8 ± 5.4, of which 10.9 ± 3.5 would be detected in a photometric survey. Therefore, the presence of only seven known member WDs may not be a severe discrepancy.

Claver et al. (2001) give the total number of potential WDs in the Praesepe as nine, six of which are confirmed members. Jones & Stauffer (1991) find ~ 100 completeness-corrected members of the Praesepe brighter than $M_V = 5.5$. Assuming the broken-power-law IMF and $M_w = 6M_\odot$, the average number of WDs in the Praesepe simulations is 17.2 ± 4.5, with 7.6 ± 2.9 being detected from photometric surveys, and the remainder hidden in binary systems. If $M_w = 8M_\odot$, then the total number of WDs in the Praesepe simulation averages 19.6 ± 4.8, with an average of 8.5 ± 3.0 being found by photometric surveys.

The results for both of these clusters are quite preliminary and are sensitive to the input IMF and selection criteria. Analysis of the WDLFs in each cluster could help to verify whether or not binary stars explain the WD deficit.

Dynamical Evolution

The dynamical evolution of open clusters has often been invoked to explain the lack of WDs in the Hyades and other clusters (Weidemann et al., 1992). Self-consistent N-body simulations are only now being applied to open clusters due to the complexity of the problem. Initial results reproduce the observed, gross characteristics of open clusters well, including mass segregation and the evaporation of stars. These initial results also suggest that WDs do not evaporate preferentially from open clusters, rather, they tend to concentrate toward the central regions. This concentration occurs due to mass segregation prior to the WD formation and persists because the WDs in intermediate-age stellar clusters are more massive than the majority of cluster stars (Portegies Zwart et al., 2001).

Based on the initial results of the binary star simulations in the Hyades and Praesepe, there may be little need to invoke WD evaporation for the lack of observed WDs, though further study is needed before such a conclusion is firmly drawn. It should also be noted that the Pleiad WD is fairly distant from the concentrated center of the star cluster, in contradiction of the N-body simulations.

Table 5.1: Initial and final masses and cooling ages or observed white dwarfs, assuming cluster membership

Cluster	Object	$M_{fin}(M_\odot)$	WD age[a]	Cluster age[a]	$M_{init}(M_\odot)$ $z=0.008$	$z=0.019$	$z=0.019$[b]	$z=0.03$
NGC 1039	2	$0.51^{+0.12}_{-0.07}$	$7.59^{+0.21}_{-0.17}$	8.30	$4.36^{+0.32}_{-0.13}$	$4.48^{+0.31}_{-0.13}$	$4.31^{+0.27}_{-0.11}$	$4.40^{+0.28}_{-0.12}$
				8.40	$3.88^{+0.20}_{-0.09}$	$4.02^{+0.19}_{-0.08}$	$3.91^{+0.17}_{-0.07}$	$3.97^{+0.18}_{-0.08}$
NGC 6633	8	$0.76^{+0.13}_{-0.16}$	$8.16^{+0.17}_{-0.18}$	8.63	$3.46^{+0.41}_{-0.20}$	$3.62^{+0.40}_{-0.20}$	$3.56^{+0.34}_{-0.15}$	$3.59^{+0.38}_{-0.19}$
				8.68	$3.25^{+0.30}_{-0.16}$	$3.40^{+0.30}_{-0.16}$	$3.37^{+0.26}_{-0.14}$	$3.39^{+0.29}_{-0.15}$
				8.82	$2.77^{+0.15}_{-0.09}$	$2.92^{+0.15}_{-0.09}$	$2.93^{+0.14}_{-0.09}$	$2.92^{+0.15}_{-0.09}$
	27	$0.67^{+0.12}_{-0.22}$	$8.47^{+0.11}_{-0.13}$	8.63	$4.76^{+2.99}_{-0.85}$	$4.85^{+2.74}_{-0.80}$	$4.65^{+2.38}_{-0.71}$	$4.76^{+2.39}_{-0.75}$
				8.68	$4.12^{+1.28}_{-0.54}$	$4.25^{+1.21}_{-0.52}$	$4.11^{+1.11}_{-0.45}$	$4.19^{+1.14}_{-0.49}$
				8.82	$3.14^{+0.33}_{-0.21}$	$3.30^{+0.33}_{-0.21}$	$3.28^{+0.29}_{-0.19}$	$3.29^{+0.31}_{-0.21}$
NGC 7063	1	$0.39^{+0.09}_{-0.11}$	$8.05^{+0.18}_{-0.17}$[c]	8.15	≥ 6.53	≥ 6.51	≥ 6.22	$6.52^{+\infty}_{-0.21}$

[a] WD cooling age

[b] No convective overshoot

[c] Assumes CO core

Table 5.2: Initial & Final masses for previously-published WD data in NGC 2516.

Object[a]	WD Mass ($M_\odot$)	Cooling age	Initial Mass ($M_\odot$)[b] age=8.05	age=8.10	age=8.15	age=8.20	age=8.25	age=8.30
NGC 2516-1	0.931	7.802	7.42	6.64	6.02	5.54	5.13	4.79
NGC 2516-2	1.010	7.606	6.24	5.79	5.40	5.06	4.77	4.49
NGC 2516-3	0.972	7.950	> 8	> 8	7.21	6.34	5.70	5.20
NGC 2516-4	1.066	7.887	> 8	7.42	6.57	5.91	5.41	4.99

[a] As given in Koester & Reimers (1996)

[b] Assuming solar metallicity with convective overshoot

Table 5.3: Initial-final mass relation for Pleiad WD

Adopted WD	Cooling	Final mass ($M_\odot$) for			
mass ($M_\odot$)	age	age=8.00	age=8.05	age=8.10	age=8.15
1.09[a]	7.98[a]	$\gtrsim 50$	$\gtrsim 13$	$\gtrsim 9$	7.65
1.16[b]	7.90[b]	$\gtrsim 11$	$\gtrsim 8$	7.59	6.68
1.00	7.74	7.70	6.66	6.28	5.77

[a] From Claver et al. (2001)

[b] Extrapolation from Claver et al. (2001) $T_{\rm eff}$ and $\log g$

Table 5.4: Initial & Final masses for previously-published WD data in the Hyades and Praesepe.

Object	WD Mass	Cooling	Initial Mass ($M_\odot$)[b]		
	($M_\odot$)	age[a]	age=8.75	age=8.80	age=8.85
WD 0836+201	0.623	8.188	3.17	3.00	2.85
WD 0836+199	0.823	8.601	4.41	3.87	3.50
WD 0837+199	0.814	8.360	3.40	3.19	3.00
WD 0840+200	0.752	8.523	3.89	3.54	3.27
WD 0836+197	0.904	8.141	3.13	2.97	2.82
WD 0352+098	0.709	8.431	3.55	3.31	3.09
WD 0406+169	0.798	8.488	3.74	3.43	3.19
WD 0421+162	0.676	8.007	3.04	2.90	2.76
WD 0425+168	0.699	7.611	2.91	2.79	2.67
WD 0431+125	0.651	7.811	2.96	2.83	2.70
WD 0438+108	0.681	7.280	2.87	2.75	2.64
WD 0437+138	0.773	8.450	3.61	3.35	3.12

[a] From W95 C/O core models

[b] Average of $Z = 0.019$ and $Z = 0.030$ with convective overshoot

Table 5.5: The white dwarf luminosity function from NGC 2168.

V	$N_{\mathrm{WD,obs.}}$	f^a	σ_f^a	$N_{\mathrm{WD,corr.}}$	$\sigma_{N_{\mathrm{WD,corr.}}}$
20.0	0	0.878	0.009	0	$\cdots$
20.5	1	0.716	0.020	1.40	1.40
21.0	2	0.659	0.017	3.04	2.15
21.5	1	0.410	0.017	2.44	2.44
22.0	0	0.070	0.009	0	$\cdots$

[a] As in Bolte (1989) Eq. 1 and Eq. 2

Table 5.6: Simulated numbers of WD detections in NGC 6633

IMF[a]	Binary fraction	$M_{\rm crit}$ ($M_\odot$)	N_{WD} total	N_{WD} detected	$N_{WD}^{\rm bin}$ detected[b]
1	0.7	8	17.0 ± 4.9	7.3 ± 2.9	4.3 ± 2.2
		6	13.9 ± 4.3	6.5 ± 2.7	4.1 ± 2.1
	0.5	8	16.9 ± 4.8	9.1 ± 3.3	3.5 ± 1.9
		6	13.9 ± 4.2	7.9 ± 3.0	3.3 ± 1.9
	0.3	8	16.9 ± 4.8	11.5 ± 3.7	2.4 ± 1.6
		6	13.9 ± 4.3	9.8 ± 3.5	2.3 ± 1.6
2	0.7	8	9.8 ± 3.4	5.2 ± 2.4	3.4 ± 1.9
		6	8.4 ± 3.1	4.8 ± 2.3	3.3 ± 1.9
	0.5	8	9.7 ± 3.4	6.0 ± 2.6	2.8 ± 1.7
		6	8.4 ± 3.2	5.5 ± 2.5	2.7 ± 1.7
	0.3	8	9.6 ± 3.4	7.1 ± 2.8	1.9 ± 1.4
		6	8.4 ± 3.2	6.4 ± 2.7	1.8 ± 1.4
3	0.7	8	13.9 ± 4.2	4.0 ± 2.0	1.5 ± 1.2
		6	11.8 ± 3.8	3.5 ± 1.9	1.5 ± 1.3
	0.5	8	13.9 ± 4.2	5.8 ± 2.6	1.2 ± 1.1
		6	11.7 ± 3.8	5.1 ± 2.4	1.2 ± 1.1
	0.3	8	13.7 ± 4.2	8.2 ± 3.1	0.9 ± 0.9
		6	11.7 ± 3.8	7.1 ± 2.9	0.8 ± 0.9

[a] 1=Salpeter, 2=Power law, 3=Broken power law

[b] This is a subset of the number of detected WDs

Table 5.7: Simulated numbers of WD detections in NGC 2168

age	IMF[a]	Binary frac	$M_{\rm crit}$ ($M_\odot$)	N_{WD} total	N_{WD} detected	$N_{WD}^{\rm bin}$ detected[b]
8.0	1	0.5	8	3.6 ± 2.0	3.0 ± 1.8	1.8 ± 1.4
			6	1.1 ± 1.1	0.9 ± 1.0	0.6 ± 0.8
	2	0.5	8	1.9 ± 1.4	1.7 ± 1.3	1.1 ± 1.0
			6	0.6 ± 0.8	0.6 ± 0.8	0.4 ± 0.6
	3	0.5	8	2.9 ± 1.7	1.6 ± 1.3	0.7 ± 0.8
			6	0.9 ± 1.0	0.6 ± 0.8	0.3 ± 0.5
8.3	1	0.7	8	8.4 ± 3.2	5.9 ± 2.6	4.4 ± 2.2
			6	5.7 ± 2.6	4.2 ± 2.2	3.2 ± 1.9
		0.5	8	8.4 ± 3.2	6.4 ± 2.8	3.6 ± 2.0
			6	5.6 ± 2.5	4.4 ± 2.2	2.6 ± 1.6
		0.3	8	8.4 ± 3.2	7.0 ± 2.9	2.5 ± 1.6
			6	5.6 ± 2.5	4.8 ± 2.3	1.8 ± 1.4
	2	0.7	8	4.8 ± 2.4	3.9 ± 2.1	3.1 ± 1.8
			6	3.5 ± 1.9	2.9 ± 1.8	2.3 ± 1.6
		0.5	8	4.8 ± 2.3	4.1 ± 2.1	2.5 ± 1.6
			6	3.4 ± 1.9	3.0 ± 1.8	1.9 ± 1.4
		0.3	8	4.8 ± 2.3	4.3 ± 2.2	1.7 ± 1.4
			6	3.4 ± 1.9	3.1 ± 1.8	1.3 ± 1.1
	3	0.7	8	6.9 ± 2.8	2.8 ± 1.7	1.6 ± 1.3
			6	4.8 ± 2.3	2.1 ± 1.5	1.2 ± 1.1
		0.5	8	6.9 ± 2.8	3.6 ± 2.0	1.3 ± 1.2
			6	4.8 ± 2.3	2.6 ± 1.7	1.0 ± 1.0
		0.3	8	6.8 ± 2.8	4.5 ± 2.3	0.9 ± 0.9
			6	4.7 ± 2.3	3.2 ± 1.9	0.7 ± 0.8

[a] 1=Salpeter, 2=Power law, 3=Broken power law

[b] This is a subset of the number of detected WDs

Figure 5.1: Derived initial-final mass relation. Filled circles indicate results from this study for the best cluster ages; error bars are $\sim 90\%$ confidence levels. The upper limit with error bars is the He-core WD in NGC 7063. Open triangles are Hyades and Praesepe WDs from Claver et al. (2001); open squares are NGC 2516 WDs from Koester & Reimers (1996); the high final-mass upper limit is the Pleiad WD from data in Claver et al. (2001). The dotted line indicates the "revised" initial-final mass relation of Weidemann (2000). The solid line is the theoretical initial-final mass relation of Girardi et al. (2000); the dashed line are the core masses at the first thermal pulse from that study.

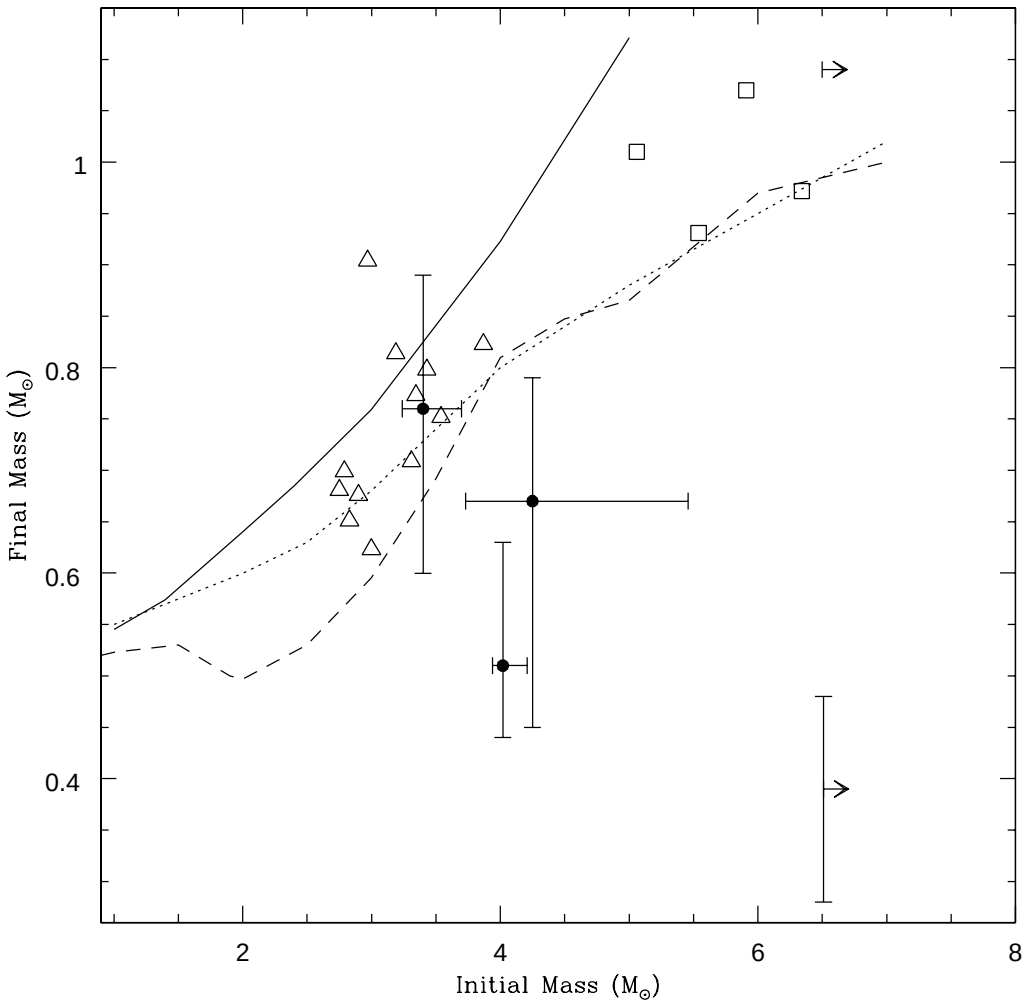

Figure 5.2: Revised initial-final mass relation, assuming an NGC 2516 age of 8.30. NGC 2516 WDs are indicated by asterisks. Filled boxes are Hyades and Praesepe data from Claver et al. (2001), filled circles are data from this study. Open star, filled pentagon, and open pentagon are for a Pleiad WD mass of $1 M_{\odot}$and Pleiad ages of 8.15, 8.05, and 8.00, respectively. Dotted line is the "revised" initial-final mass relation of Weidemann (2000); solid and dashed lines are the theoretical initial-final mass relation and core mass at first thermal pulse from Girardi (2000).

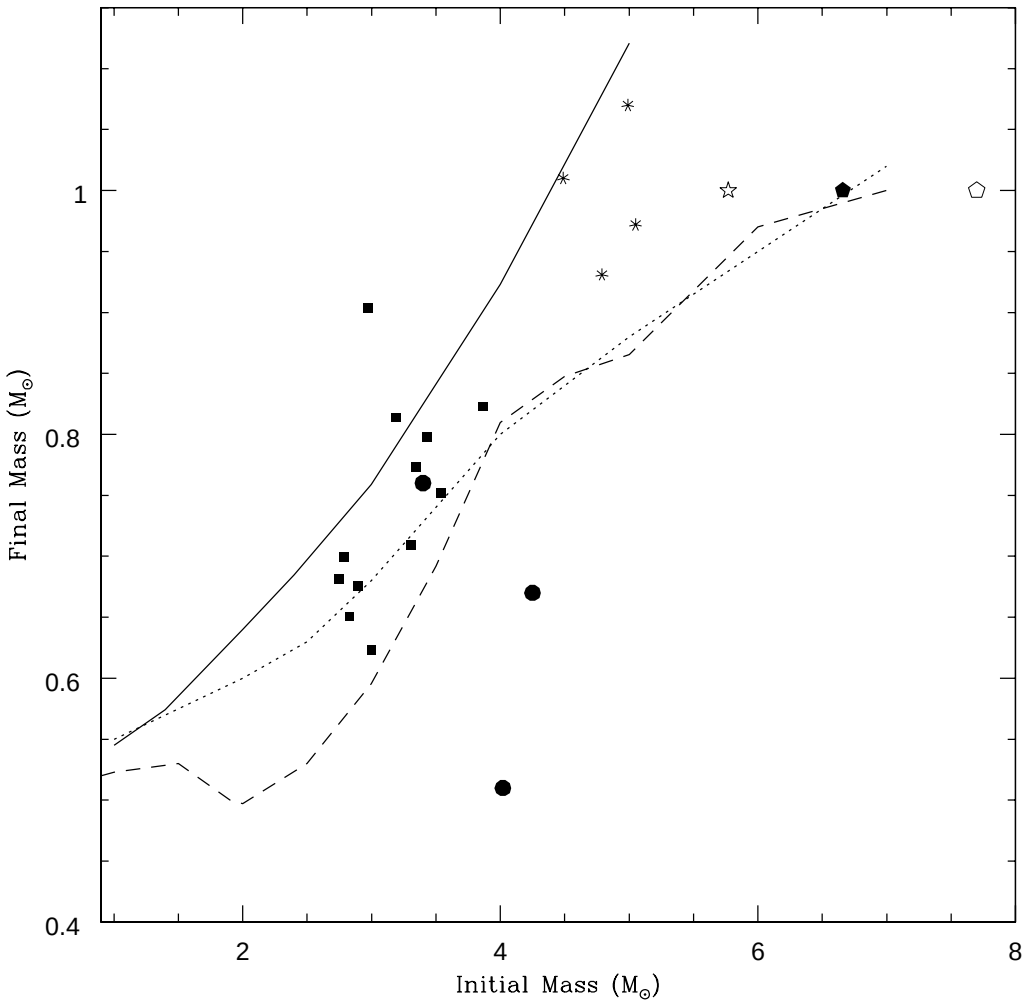

Figure 5.3: The sensitivity of derived progenitor masses to cluster age errors. The curves indicate the derived progenitor masses for WDs with actual progenitor masses of $8M_{\odot}$ (blue long-dashed), $7M_{\odot}$ (black solid), and $6M_{\odot}$ (red short-dashed) assuming errors in the logarithmic cluster age of 0.1 dex. Upper curves are for underestimates of the cluster age; lower curves are for overestimates.

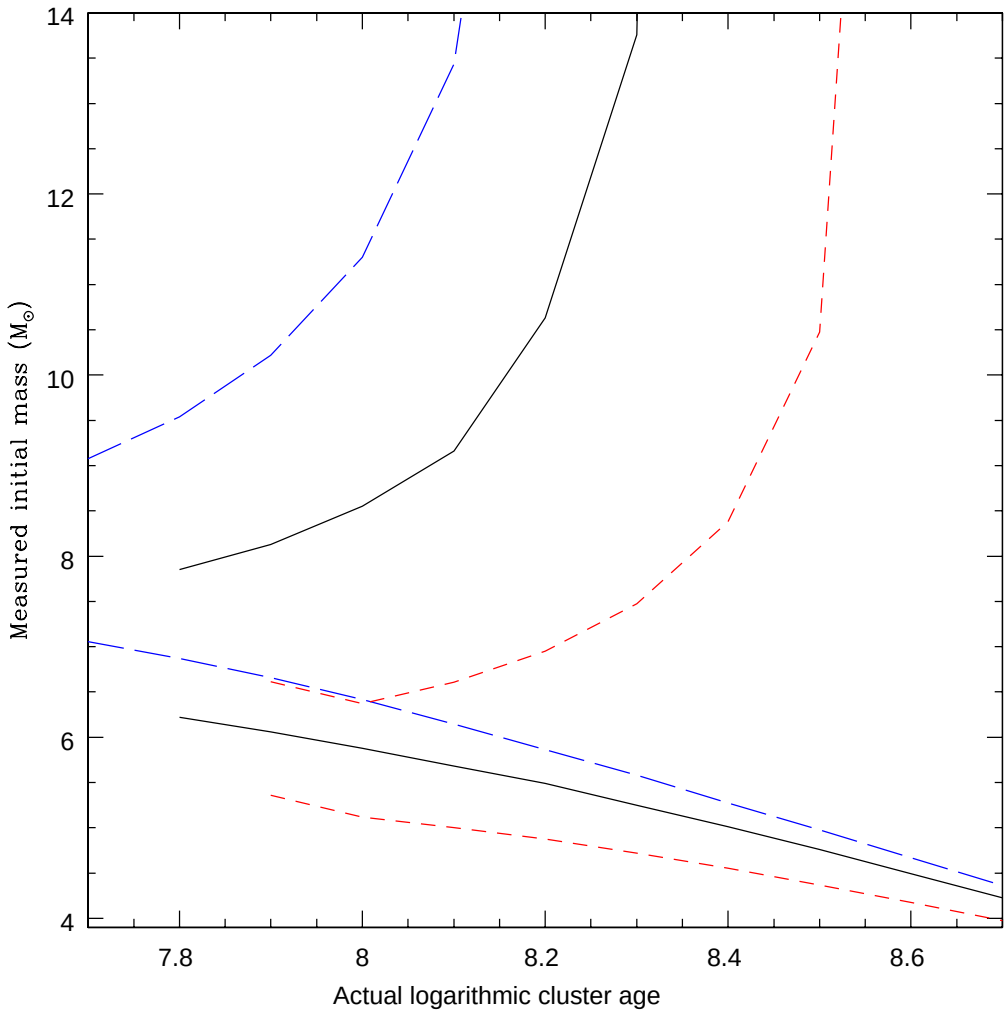

Figure 5.4: $B-V, V$ CMD of IC 4665, including results of spectroscopic observations. Figure as in Fig 3.17, except confirmed non-WDs indicated by red crosses.

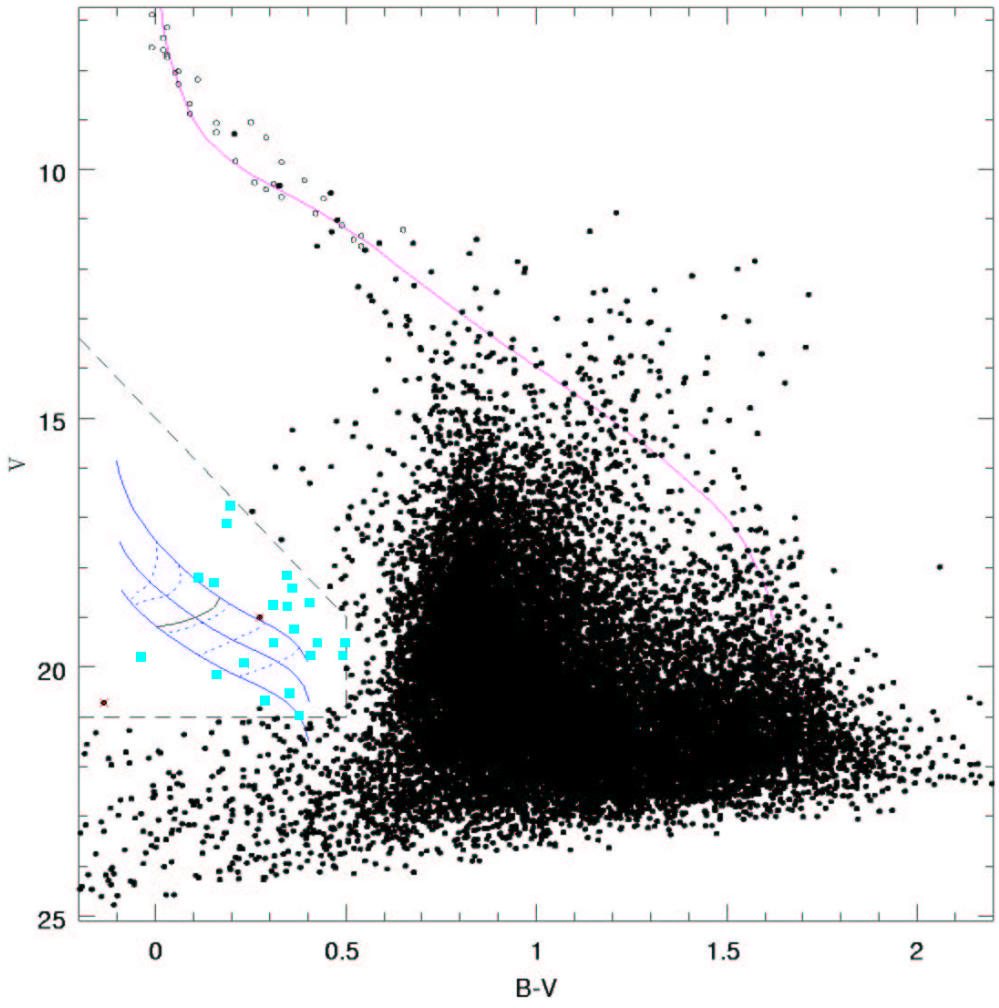

Figure 5.5: $B-V, V$ CMD of NGC 6633, including results of spectroscopic observations. Figure as in Fig. 3.18, except confirmed member WDs are shown as filled blue squares, non-member DA WDs as open blue squares, non-member DB and DO WDs as filled magenta squares, non-WDs as red crosses, and unobserved candidates as filled cyan boxes.

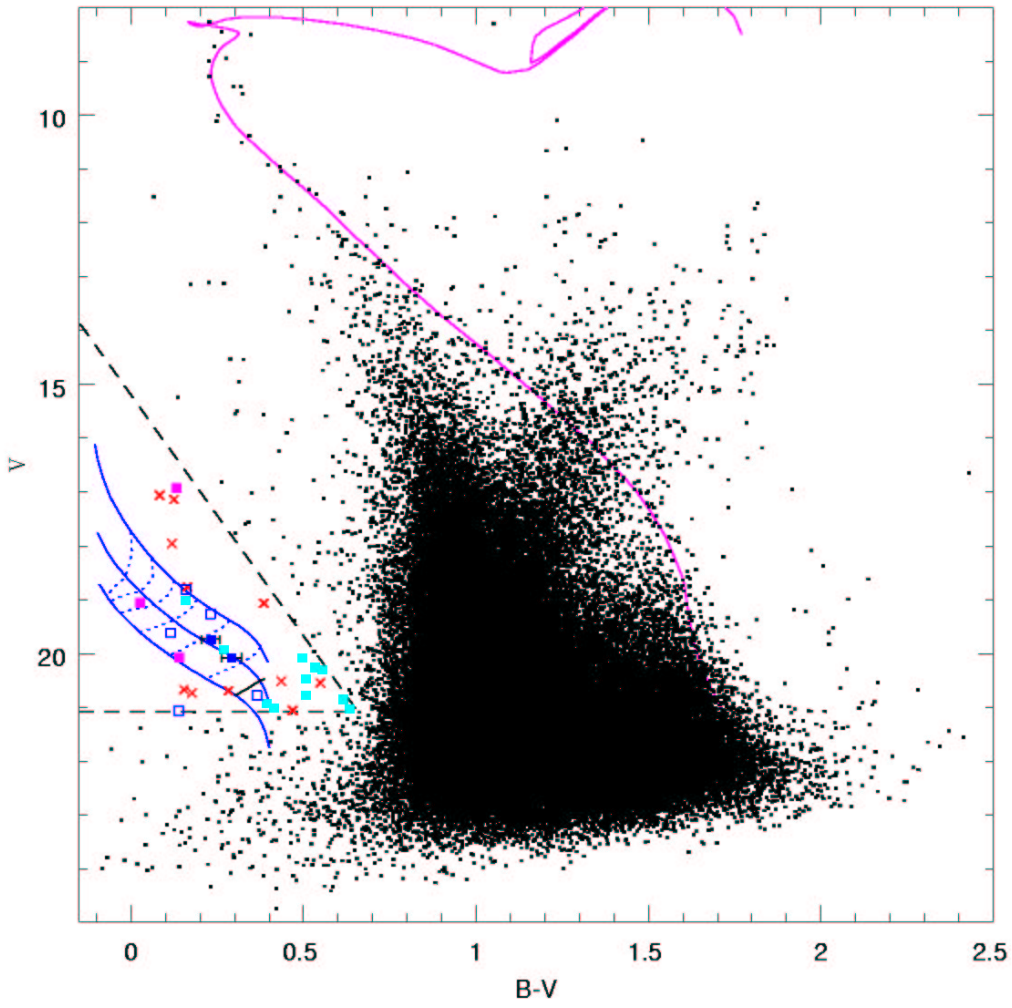

Figure 5.6: $U-B, U$ and $B-V, V$ CMDs of NGC 7063, including results of spectroscopic observations. Figure as in Fig. 3.19, except confirmed non-member WDs indicated as open blue boxes, confirmed WD member as filled blue box, and unobserved objects as filled cyan boxes.

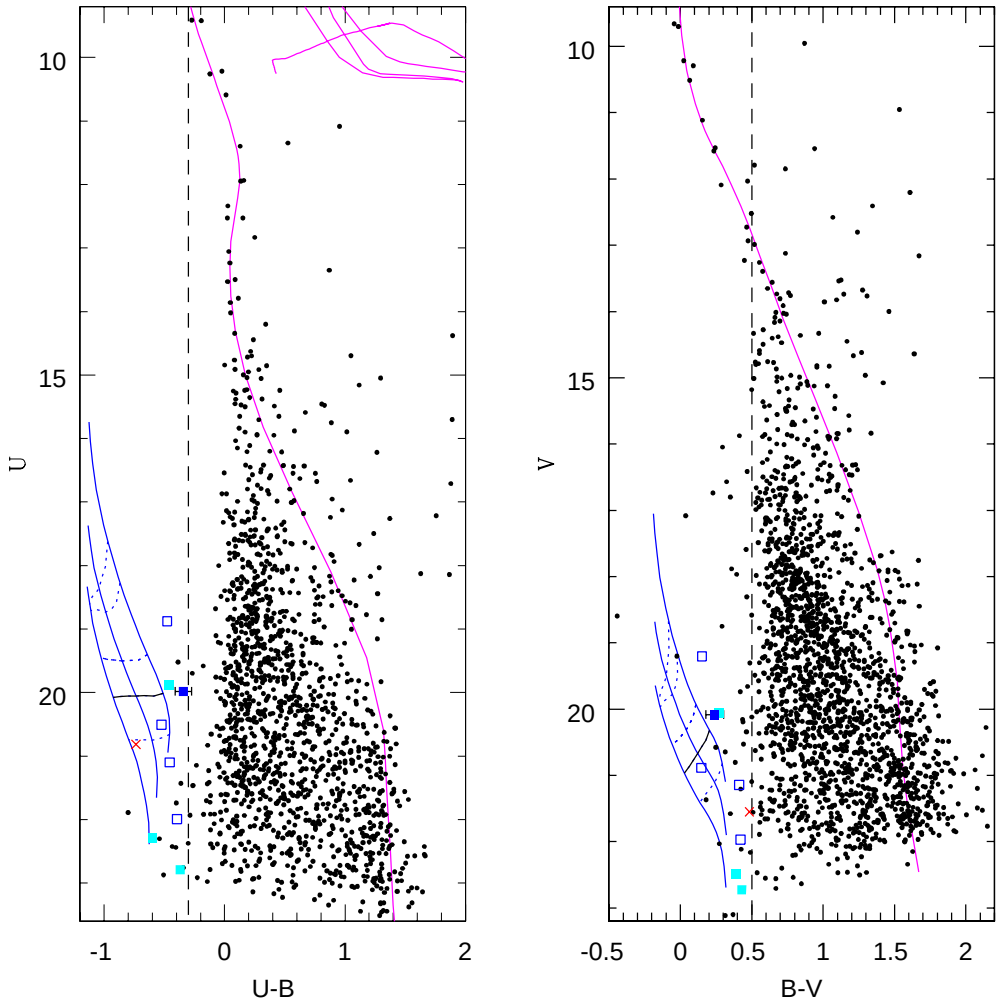

Figure 5.7: $B-V, U-B$ color-color plot on NGC 7063, including results of spectroscopic identifications. Figure as in Fig. 3.20, except confirmed member WD identified with filled blue box, confirmed non-member WDs identified with open blue boxes, and unobserved objects identified with filled cyan boxes.

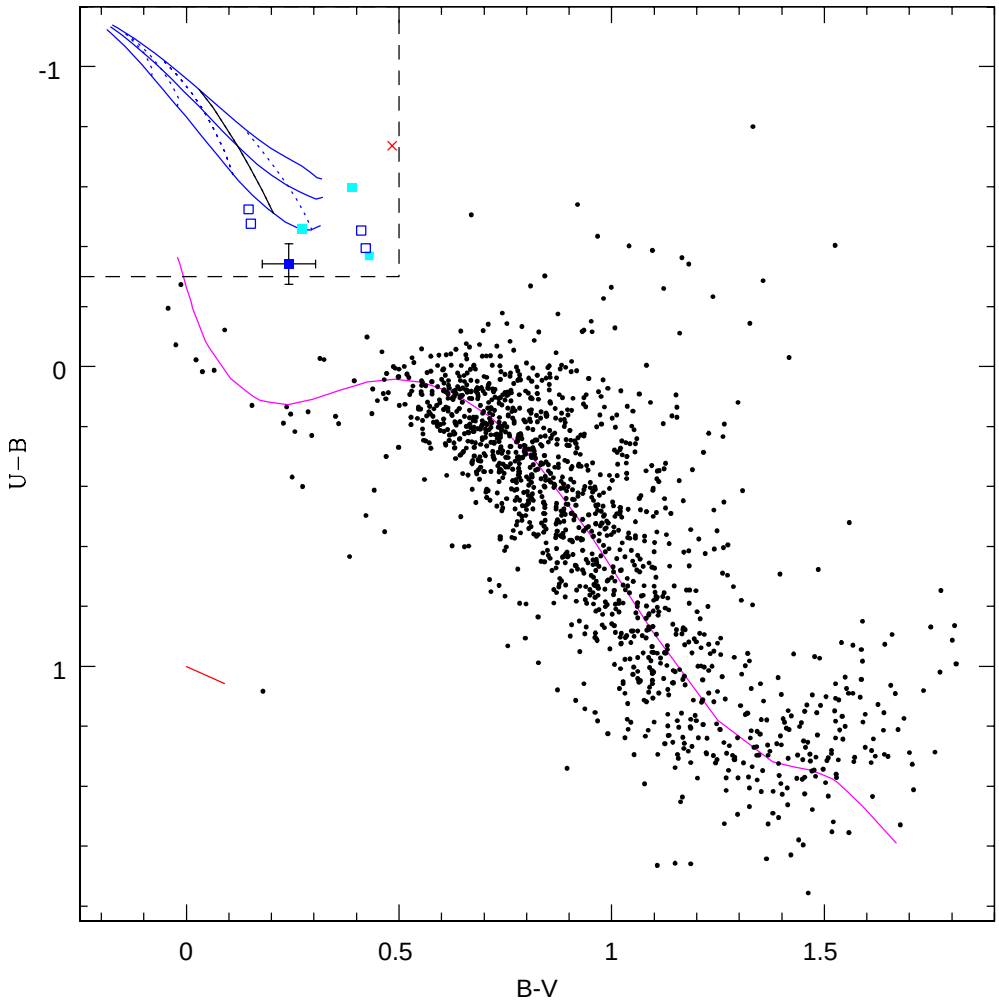

Figure 5.8: Completeness in detection of WDs in NGC 2168, based on the result of artificial star tests. Error bars are determined using Eq. 5.5.

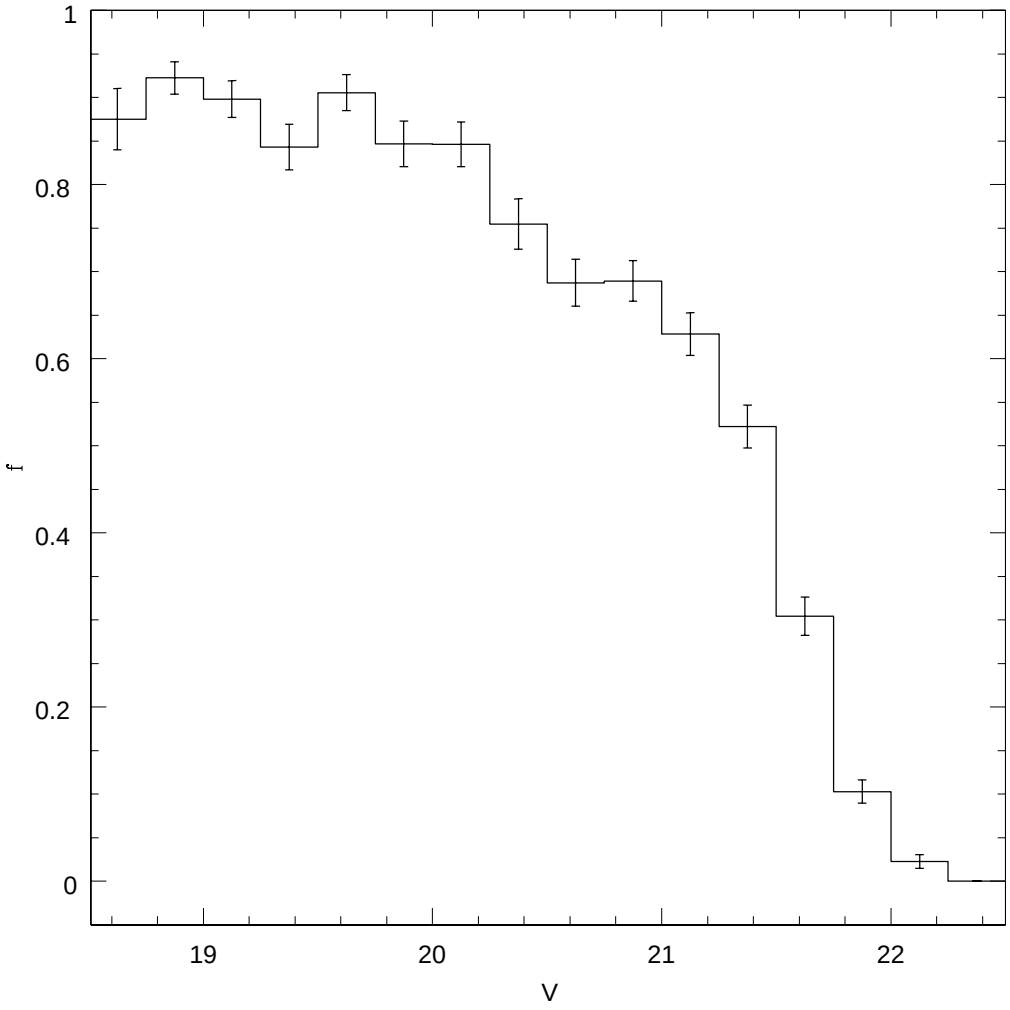

Figure 5.9: Completeness in detection of WDs in NGC 7063, based on the result of artificial star tests. Error bars are determined using Eq. 5.5.

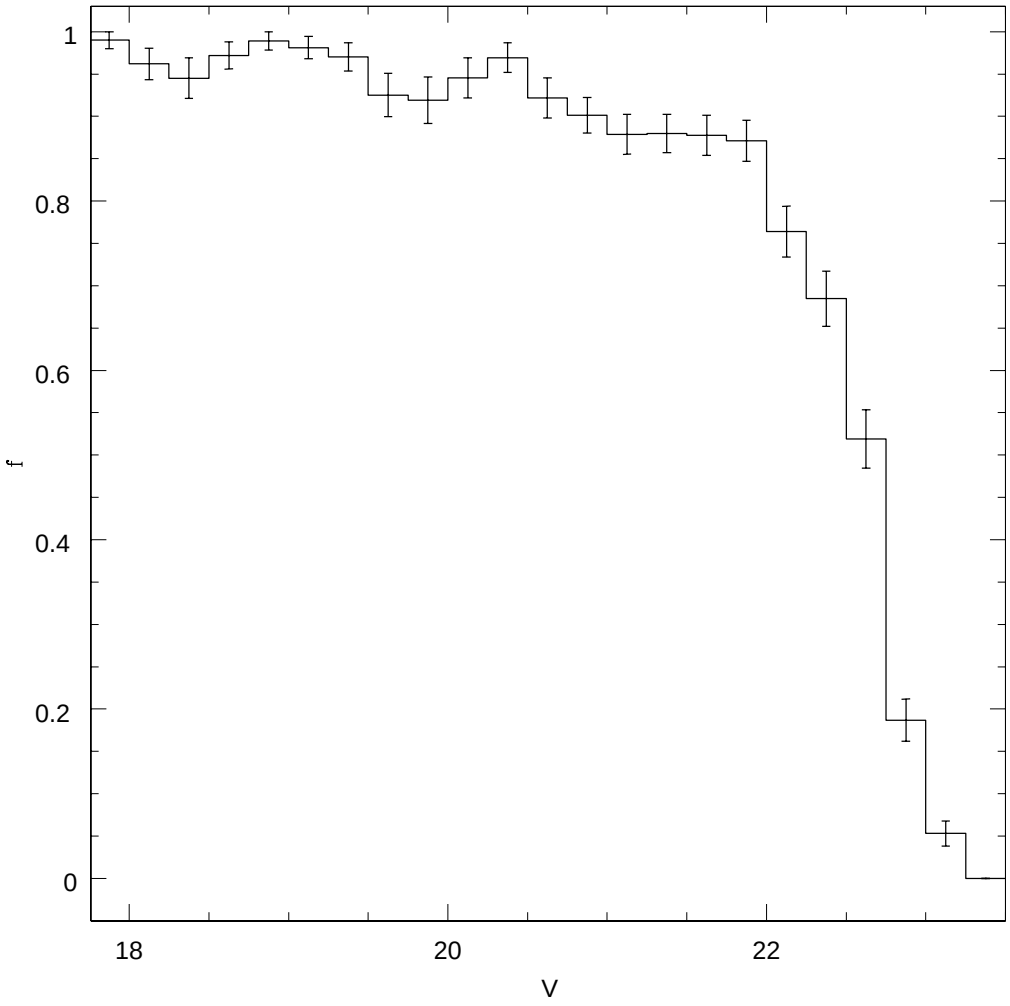

Figure 5.10: The white dwarf luminosity function (WDLF) for NGC 2168, including the raw WDLF (solid line) and the WDLF corrected for completeness (dashed line). Error bars are calculated as in Eq. 2 of Bolte (1989).

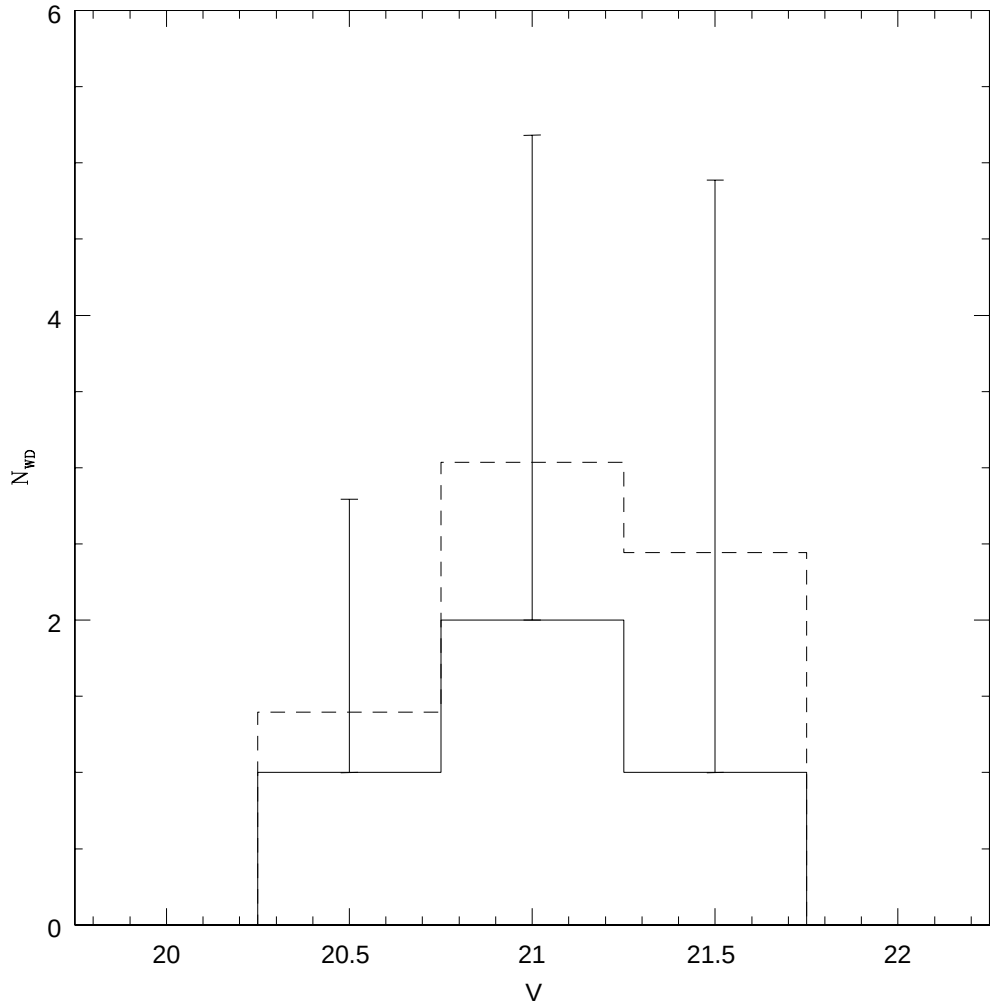

Figure 5.11: $U-B, U$ and $B-V, V$ CMDs for WDs in binary systems. Blue lines indicate WD cooling sequences for lone WDs with masses of $0.4M_{\odot}(0.1M_{\odot})1.0M_{\odot}$ (top to bottom); black line indicates the ZAMS for a solar-metallicity population; red lines indicate the sequences for ZAMS + WD binaries for WD mass of $0.7M_{\odot}$, $T_{\rm eff}$ of 50000K, 40000K, 30000K, 20000K, 15000K, and 10000K (top to bottom). The green lines indicate the binary sequences for main sequence stars with the brightest modeled WD ($0.4M_{\odot}$, $T_{\rm eff}$=50000K; top) and the faintest modeled WD ($1.0M_{\odot}$, $T_{\rm eff}$=10000K; bottom).

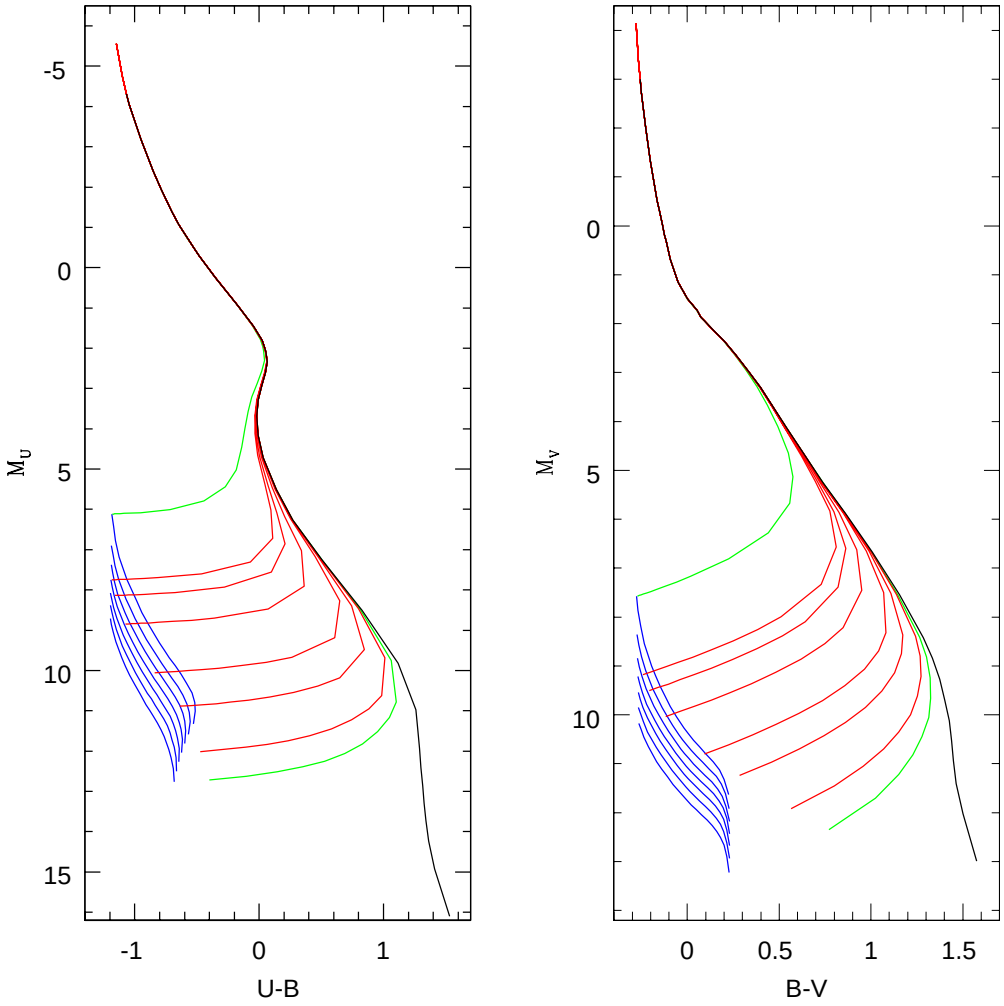

Figure 5.12: $U-B$, $B-V$ color-color plot for WDs in binary stystems. Blue lines indicate cooling sequences for lone WDs with masses of $0.4M_{\odot}$($0.1M_{\odot}$)1.0msun (bottom to top); black line indicates the ZAMS for a solar-metallicity population; red lines indicate the sequences for ZAMS + WD binaries for a WD mass of $0.7M_{\odot}$, $T_{\rm eff}$ of 50000K, 40000K, 30000K, 20000K, 15000K and 10000K (left to right turnoffs along ZAMS). Green lines indicate binary sequences for ZAMS + WD for brightest modeled WD ($0.4M_{\odot}$, $T_{\rm eff}$=50000K; left) and faintest-modeled WD ($1.0M_{\odot}$, $T_{\rm eff}$=10000K; right).

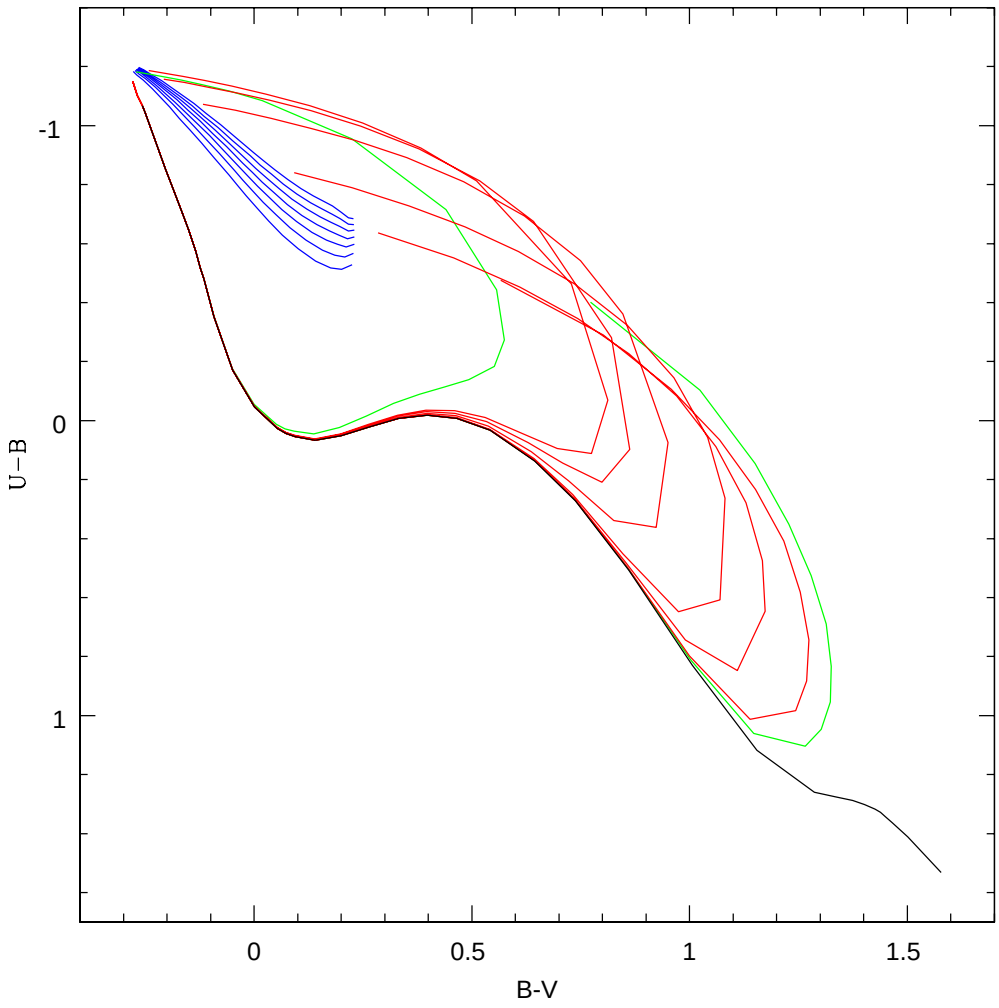

Figure 5.13: CMDs from the Monte Carlo simulation of a binary stars in a rich open cluster. The fictitious cluster has an input distance modulus and color excess of zero, a binary fraction of 0.5, an age of 8.5, and a Salpeter IMF. The main sequence, binary sequence and WD cooling sequence are easily visible, as is the region containing WD-MS binaries. Blue lines indicate WD cooling curves for single WDs of masses $0.4M_{\odot}$, $0.7M_{\odot}$, and $1.0M_{\odot}$ (top to bottom).

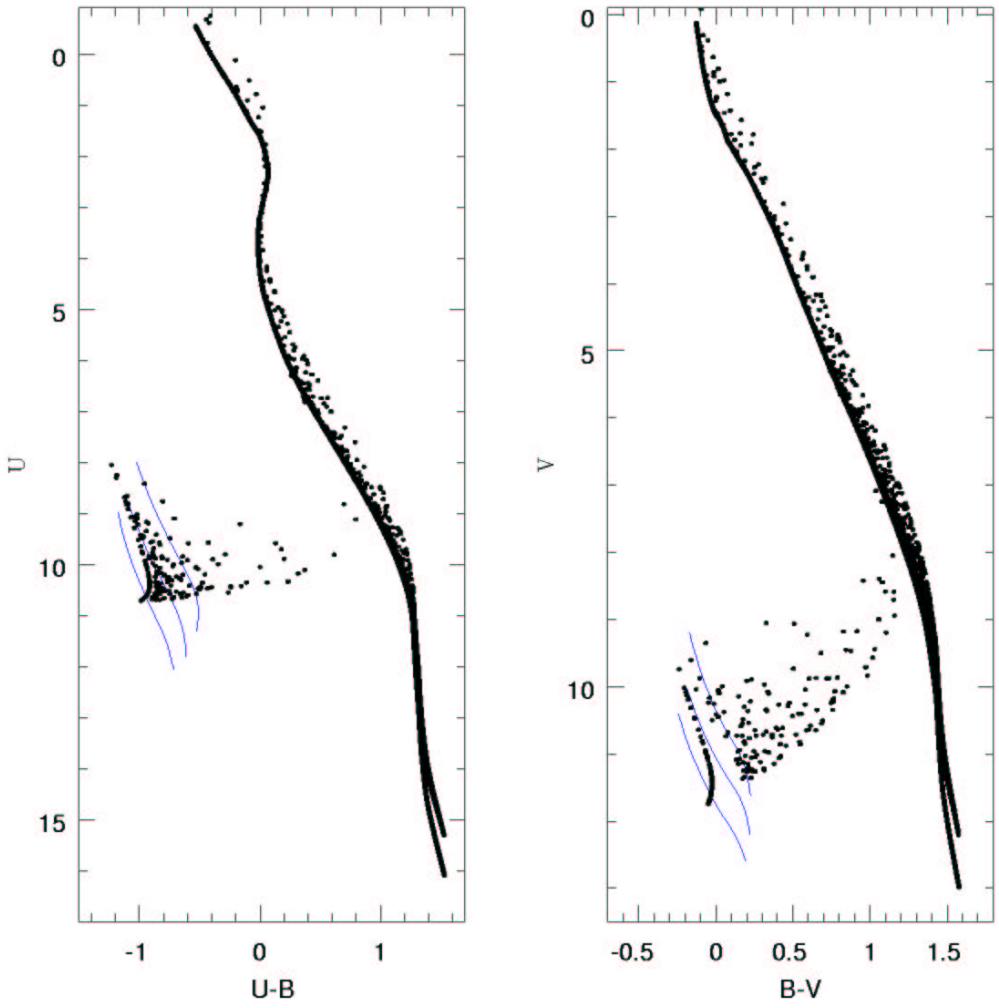

Figure 5.14: $B-V, U-B$ color-color plot from binary star simulation in Fig. 5.13. Blue curves indicate WD cooling curves for single WDs of masses $1.0M_{\odot}$, $0.7M_{\odot}$, and $0.4M_{\odot}$ (top to bottom).

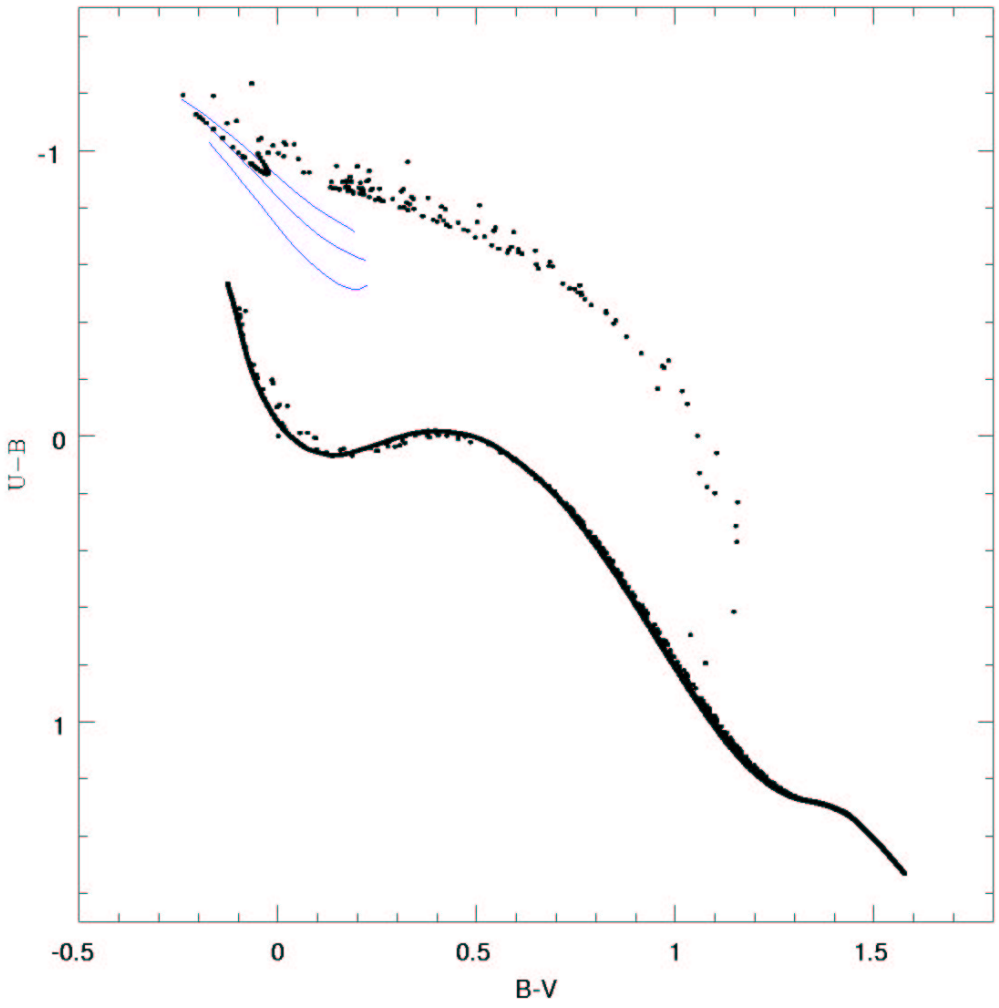

Chapter 6

Conclusions and Future Work

This dissertation presents the first results of a study of white dwarfs in intermediate-age open clusters. The primary conclusions are:

- A sample of open clusters with complete WD sequences within the reach of Keck spectroscopy has been presented.
- Photometry for the clusters NGC 2168, IC 4665, NGC 6633, and NGC 7063 has been presented. Within each cluster, WD candidates have been photometrically selected. Based on photometry alone, it is not possible to identify cluster WDs unambiguously.
- Spectroscopy for WD candidates in NGC 1039 (M34), IC 4665, NGC 6633, and NGC 7063 has been presented. Out of thirty-one identified objects, four are cluster member WDs. For each WD, the effective temperature and surface gravity have been determined, and the WD masses and cooling ages derived.
- Analysis of the initial-final mass relation reveals that the high-mass end of the relation is very sensitive to the assumed ages of the parent open clusters, more sensitive than usually stated.
- The lower limit on M_w, and therefore the lower limit on $M_{\rm crit}$, is $5.7 M_{\odot}$.
- Based on the empirical initial-final mass relation from this study and previously-published WD studies, the initial-final mass relation likely lies between the relation derived from the core masses at the first thermal pulse and the relation derived from the core mass at the end of thermal pulsing from stellar evolutionary models.

- The "white dwarf deficit," or apparent lack of WDs in open clusters as compared with what would be expected from an integration of the initial mass function, can be explained as being due to WDs being hidden in unresolved binaries. Evaporation of WDs from open clusters therefore need not be as strong an effect as sometimes suggested.

More work remains to be done in order to obtain the most useful data. Some of the necessary work includes:

- **Improved Balmer-line fitting.** Some improvements need to be made to the spectral model fits. Most importantly, the covariance matrix for error determination needs to be computed properly so that the stated errors accurately represent the model uncertainty and are less dependent on assumptions about the error distribution. It is also necessary to obtain a higher-resolution grid of spectral models, especially for high $T_{\rm eff}$. A finer model grid would permit more accurate determination of $T_{\rm eff}$ and $\log g$ for hot ($T_{\rm eff} \gtrsim 20000K$) WDs in the sample.

- **More and improved spectra.** NGC 2168 is a very interesting cluster from the standpoint of being relatively young and a very rich, compact cluster. No spectra have been obtained yet, but the masses and ages of WDs in this cluster will be important in the determination of the high-mass end of the initial-final mass relation. Improved spectra of the potential He-core WD in NGC 7063 are needed to confirm its nature. Finally, spectra of potential WD-MS binaries may confirm the presence of the binaries and the validity of the binary star simulation.

- **Imaging and analysis of more clusters.** The conclusions drawn from this study have been hampered by the small numbers of cluster member WDs confirmed to date. Analysis of more clusters will provide a larger cluster-member WD sample. In addition, attention needs to be focused on rich open clusters in order to improve the likelihood of finding cluster WDs.

References

Althaus, L. G. & Benvenuto, O. G. 1997, *The Astrophysical Journal*, **477**, 313

Anthony-Twarog, B. J. 1982, *The Astrophysical Journal*, **255**, 245

Barrado y Navascués, D., Stauffer, J. R., Bouvier, J. ., & Martín, E. L. 2001, *The Astrophysical Journal*, **546**, 1006

Basri, G., Marcy, G. W., & Graham, J. R. 1996, *The Astrophysical Journal*, **458**, 600

Beers, T. C., Preston, G. W., & Shectman, S. A. 1988, *The Astrophysical Journals*, **67**, 461

Begelman, M. C. 2001, in *ASP Conf. Ser. 240: Gas and Galaxy Evolution*, p. 363

Bergeron, P., Liebert, J., & Fulbright, M. S. 1995a, *The Astrophysical Journal*, **444**, 810

Bergeron, P., Saffer, R. A., & Liebert, J. 1992, *The Astrophysical Journal*, **394**, 228

Bergeron, P., Wesemael, F., & Beauchamp, A. 1995b, *Publications of the Astronomical Society of the Pacific*, **107**, 1047

Bergeron, P., Wesemael, F., Fontaine, G., & Liebert, J. 1990, *The Astrophysical Journall*, **351**, L21

Bessell, M. S., Castelli, F., & Plez, B. 1998, *Astronomy & Astrophysics*, **333**, 231

Binney, J. 2001, in *ASP Conf. Ser. 240: Gas and Galaxy Evolution*, p. 355

Bolte, M. 1989, *The Astrophysical Journal*, **341**, 168

Bono, G., Caputo, F., Cassisi, S., Marconi, M., Piersanti, L., & Tornambè, A. 2000, *The Astrophysical Journal*, **543**, 955

Boyle, B. J. 1989, *Monthly Notices of the Royal Astronomical Society*, **240**, 533

Bragaglia, A., Renzini, A., & Bergeron, P. 1995, *The Astrophysical Journal*, **443**, 735

Brighenti, F. & Mathews, W. G. 1998, *The Astrophysical Journal*, **495**, 239

Castellani, V., Chieffi, A., Tornambe, A., & Pulone, L. 1985, *The Astrophysical Journall*, **294**, L31

Claver, C. F., Liebert, J., Bergeron, P., & Koester, D. 2001, *The Astrophysical Journal*, **563**, 987

Dekel, A. & Silk, J. 1986, *The Astrophysical Journal*, **303**, 39

Dias, W. S., Alessi, B. S., Moitinho, A., & Lépine, J. R. D. 2002, *Astronomy & Astrophysics*, **389**, 871

Dominguez, I., Chieffi, A., Limongi, M., & Straniero, O. 1999, *The Astrophysical Journal*, **524**, 226

Dragicevich, P. M., Blair, D. G., & Burman, R. R. 1999, *Monthly Notices of the Royal Astronomical Society*, **302**, 693

Ferrara, A. & Tolstoy, E. 2000, *Monthly Notices of the Royal Astronomical Society*, **313**, 291

Finley, D. S., Koester, D., & Basri, G. 1997, *The Astrophysical Journal*, **488**, 375

Fontaine, G., Brassard, P., & Bergeron, P. 2001, *Publications of the Astronomical Society of the Pacific*, **113**, 409

Fontaine, G., Brassard, P., Bergeron, P., & Wesemael, F. 1992, *The Astrophysical Journall*, **399**, L91

Girardi, L., Bertelli, G., Bressan, A., Chiosi, C., Groenewegen, M. A. T., Marigo, P., Salasnich, B., & Weiss, A. 2002, *Astronomy & Astrophysics*, **391**, 195

Girardi, L., Bressan, A., Bertelli, G., & Chiosi, C. 2000, *Astronomy & Astrophysicss*,

141, 371

Glushkova, E. V. & Uglova, I. M. 1997, *Astronomy Letters*, **23**, 591

Hansen, B. M. S. 1999, *The Astrophysical Journal*, **520**, 680

Hayes, D. S. 1985, in *IAU Symp. 111: Calibration of Fundamental Stellar Quantities*, Vol. 111, pp 225–249

Hoag, A. A., Johnson, H. L., Iriarte, B., Mitchell, R. I., Hallam, K. L., & Sharpless, S. 1961, *Publications of the U.S. Naval Observatory Second Series*, **17**, 345

Janes, K. & Adler, D. 1982, *The Astrophysical Journals*, **49**, 425

Janes, K. A., Tilley, C., & Lynga, G. 1988, *The Astronomical Journal*, **95**, 771

Jeffries, R. D. 1997, *Monthly Notices of the Royal Astronomical Society*, **288**, 585

Jeffries, R. D., Totten, E. J., Harmer, S., & Deliyannis, C. P. 2002, *Monthly Notices of the Royal Astronomical Society*, **336**, 1109

Jones, B. F. & Prosser, C. F. 1996, *The Astronomical Journal*, **111**, 1193

Jones, B. F. & Stauffer, J. R. 1991, *The Astronomical Journal*, **102**, 1080

Kalirai, J. S., Richer, H. B., Fahlman, G. G., Cuillandre, J., Ventura, P., D'Antona, F., Bertin, E., Marconi, G., & Durrell, P. R. 2001a, *The Astronomical Journal*, **122**, 257

Kalirai, J. S., Ventura, P., Richer, H. B., Fahlman, G. G., Durrell, P. R., D'Antona, F., & Marconi, G. 2001b, *The Astronomical Journal*, **122**, 3239

Koester, D. & Reimers, D. 1981, *Astronomy & Astrophysics*, **99**, L8

Koester, D. & Reimers, D. 1985, *Astronomy & Astrophysics*, **153**, 260

Koester, D. & Reimers, D. 1993, *Astronomy & Astrophysics*, **275**, 479

Koester, D. & Reimers, D. 1996, *Astronomy & Astrophysics*, **313**, 810

Koester, D., Schulz, H., & Wegner, G. 1981, *Astronomy & Astrophysics*, **102**, 331

Koester, D., Schulz, H., & Weidemann, V. 1979, *Astronomy & Astrophysics*, **76**, 262

Kurucz, R. L. 1979, *The Astrophysical Journals*, **40**, 1

Lamb, D. Q. & van Horn, H. M. 1975, *The Astrophysical Journal*, **200**, 306

Landolt, A. U. 1992, *The Astronomical Journal*, **104**, 340

Liebert, J., Dahn, C. C., & Monet, D. G. 1988, *The Astrophysical Journal*, **332**, 891

Mathews, W. G. 1989, *The Astronomical Journal*, **97**, 42

Mayle, R. & Wilson, J. R. 1988, *The Astrophysical Journal*, **334**, 909

McMahan, R. K. 1989, *The Astrophysical Journal*, **336**, 409

Mermilliod, J. 1995, in *ASSL Vol. 203: Information & On-Line Data in Astronomy*, p. 127

Mestel, L. 1952, *Monthly Notices of the Royal Astronomical Society*, **112**, 583

Meusinger, H., Schilbach, E., & Souchay, J. 1996, *Astronomy & Astrophysics*, **312**, 833

Narayanan, V. K. & Gould, A. 1999, *The Astrophysical Journal*, **523**, 328

Naylor, T., Totten, E. J., Jeffries, R. D., Pozzo, M., Devey, C. R., & Thompson, S. A. 2002, *Monthly Notices of the Royal Astronomical Society*, **335**, 291

Oke, J. B., Cohen, J. G., Carr, M., Cromer, J., Dingizian, A., Harris, F. H., Labrecque, S., Lucinio, R., Schaal, W., Epps, H., & Miller, J. 1995, *Publications of the Astronomical Society of the Pacific*, **107**, 375

Pinsonneault, M. H., Stauffer, J., Soderblom, D. R., King, J. R., & Hanson, R. B. 1998, *The Astrophysical Journal*, **504**, 170

Portegies Zwart, S. F., McMillan, S. L. W., Hut, P., & Makino, J. 2001, *Monthly Notices of the Royal Astronomical Society*, **321**, 199

Press, W. H., Teukolsky, S. A., Vetterling, W. T., & Flannery, B. P. 1992, *Numerical recipes in FORTRAN. The art of scientific computing*, Cambridge: University Press,

—c1992, 2nd ed.

Prosser, C. F. 1993, *The Astronomical Journal*, **105**, 1441

Raboud, D. & Mermilliod, J.-C. 1998, *Astronomy & Astrophysics*, **329**, 101

Reimers, D. & Koester, D. 1982, *Astronomy & Astrophysics*, **116**, 341

Reimers, D. & Koester, D. 1988, *Astronomy & Astrophysics*, **202**, 77

Reimers, D. & Koester, D. 1989, *Astronomy & Astrophysics*, **218**, 118

Reimers, D. & Koester, D. 1994, *Astronomy & Astrophysics*, **285**, 451

Richer, H. B., Fahlman, G. G., Rosvick, J., & Ibata, R. 1998, *The Astrophysical Journall*, **504**, L91

Romanishin, W. & Angel, J. R. P. 1980, *The Astrophysical Journal*, **235**, 992

Salaris, M., Dominguez, I., Garcia-Berro, E., Hernanz, M., Isern, J., & Mochkovitch, R. 1997, *The Astrophysical Journal*, **486**, 413

Salpeter, E. E. 1955, *The Astrophysical Journal*, **121**, 161

Salpeter, E. E. 1971, ARA&A, **9**, 127

Sanders, W. L. 1973, *Astronomy & Astrophysicss*, **9**, 213

Schilbach, E., Robichon, N., Souchay, J., & Guibert, J. 1995, *Astronomy & Astrophysics*, **299**, 696

Schwarzschild, M. 1958, *Structure and evolution of the stars.*, Princeton, Princeton University Press, 1958.

Somerville, R. S. & Primack, J. R. 1999, *Monthly Notices of the Royal Astronomical Society*, **310**, 1087

Stauffer, J. R., Schultz, G., & Kirkpatrick, J. D. 1998, *The Astrophysical Journall*, **499**, L199

Stello, D. & Nissen, P. E. 2001, *Astronomy & Astrophysics*, **374**, 105

Stetson, P. B. 1992, in *ASP Conf. Ser. 25: Astronomical Data Analysis Software and Systems I*, Vol. 1, p. 297

Sung, H. & Bessell, M. S. 1999, *Monthly Notices of the Royal Astronomical Society*, **306**, 361

Sung, H., Bessell, M. S., Lee, B., & Lee, S. 2002, *The Astronomical Journal*, **123**, 290

Tinsley, B. M. 1974, *Publications of the Astronomical Society of the Pacific*, **86**, 554

van den Bergh, S. & Tammann, G. A. 1991, ARA&A, **29**, 363

van den Heuvel, E. P. J. 1975, *The Astrophysical Journall*, **196**, L121

von Hippel, T., Steinhauer, A., Sarajedini, A., & Deliyannis, C. P. 2002, *The Astronomical Journal*, **124**, 1555

Wegner, G., Reid, I. N., & McMahan, R. K. 1991, *The Astrophysical Journal*, **376**, 186

Weidemann, V. 2000, *Astronomy & Astrophysics*, **363**, 647

Weidemann, V., Jordan, S., Iben, I. J., & Casertano, S. 1992, *The Astronomical Journal*, **104**, 1876

Williams, K. A., Bolte, M., Claver, C. F., & Wood, M. A. 2001, *American Astronomical Society Meeting*, 198

Wood, M. A. 1990, *Journal of the Royal Astronomical Society of Canada*, **84**, 150

Wood, M. A. 1995, in *LNP Vol. 443: White Dwarfs*, p. 41

Yi, S., Demarque, P., Kim, Y., Lee, Y., Ree, C. H., Lejeune, T., & Barnes, S. 2001, *The Astrophysical Journals*, **136**, 417